CHARACTERISTICS OF MICROSEISMS RECORDED BY THE EARTHSCOPE TRANSPORTABLE ARRAY

by

Oner Sufri

A dissertation submitted to the faculty of
The University of Utah
in partial fulfillment of the requirements for the degree of

Doctor of Philosophy

in

Geophysics

Department of Geology and Geophysics

The University of Utah

May 2015

The University of Utah Graduate School

STATEMENT OF DISSERTATION APPROVAL

The dissertation of Oner Sufri

has been approved by the following supervisory committee members:

Keith Koper	, Chair	6/30/2014 Date Approved
Michael Thorne	, Member	6/30/2014 Date Approved
Kristine Pankow	, Member	6/30/2014 Date Approved
Jeffrey Moore	, Member	6/30/2014 Date Approved
Benjamin de Foy	, Member	6/30/2014 Date Approved

and by John Bartley , Chair of the

Department of Geology and Geophysics

and by David B. Kieda, Dean of The Graduate School.

ABSTRACT

I analyzed the characteristics of microseisms recorded in the United States by Earthscope Transportable Array (TA) broadband stations during the calendar year of 2009 and a 19-day period of October–November 2012. I used eigen-decomposition of spectral covariance matrices to extract power and polarization information for each hour of data recorded at each seismometer. For the continuous data from 2009, I generated array-averaged spectrograms and geographical animations to locate individual microseisms. Then, I grouped and cataloged those microseisms according to their initiation time, duration, peak power, average power, dominant period, variation in their period content, degree of polarization, and their azimuths obtained from polarization ellipsoids. Over 78 distinct microseismic events were identified and grouped into four different types. The longest duration microseismic signal occurred in the month of December, 2009, for more than 280 hours and was associated with the propagation of two storms: one from the Gulf of Alaska region and another from the Newfoundland region. The most powerful signal was also recorded in the same month with an average peak period near 6-sec on December 28–31, 2009, and resulted from wave action associated with two different unnamed storms in the East-Central Pacific and North Atlantic oceans. The seismic observations were compared to excitation predictions computed with the power spectral density of the equivalent pressure generated by ocean gravity waves using the WAVEWATCH-III ocean wave model from the French Research Institue for

Exploitation of the Sea (Ifremer). Microseismic excitation predictions were calculated both with and without coastline reflections.

I also processed continuous TA seismic data from 17 October–4 November, 2012, coinciding with the passage of Hurricane Sandy. I determined and tracked locations of microseisms as the hurricane propagated from South to North along the U.S. Atlantic coast. I found that the maximum microseismic power and degree of polarization occurred when Sandy made its westward turn towards New York on October 29, 2012. I also found two microseism source locations in the North Atlantic and Northeast Pacific oceans related to two different storms systems. The locations obtained from the seismic results were compared to the ocean wave models obtained from Ifremer.

This work is dedicated to my mother and father.

TABLE OF CONTENTS

LIST OF FIGURES

ACKNOWLEDGEMENTS

I would like to thank my advisor Keith Koper for the time and effort mentoring me and helping me to become a good scientist. Since I started working with him, I learned a lot in terms of programming, teaching, and finding solutions to scientific questions. I also would like to thank my committee members Kris Pankow, Michael Thorne, Jeffrey Moore, and Benjamin De Foy for their insights and suggestions.

I would like to thank Relu Burlacu as well, for his help during my PhD study.

Finally I would like to thank my family, my mother, and father for their patience. Although they were not here with me, they were always supportive and encouraging.

CHAPTER 1

INTRODUCTION

When an earthquake-free seismogram is inspected, one realizes that there is noise generated by processes such as traffic, construction, heavy machinery, wind, and ocean and lake waves. Previous studies have shown that human activities (construction, traffic, etc.) and wind contribute primarily to the shorter period (< 1 sec) portion of the seismic noise, whereas ocean or lake waves primarily contribute to the long-period (>1 sec) portion of the seismic noise (e.g., McNamara and Buland, 2004). The longer period naturally occurring noise signals are known as microseisms.

Early studies from the 1900s through the early 1940s proposed different mechanisms for explaining the cause of microseisms. One was the motion of weather systems (Gutenberg, 1924). It was claimed that atmospheric disturbances were strongly correlated with microseisms, and changes in storms tracks were predictable from the irregularities of recorded seismic waves (Banerji, 1935). Another proposed mechanism was that pumping of the atmosphere could be the reason for observing microseisms. According to this idea, when the center of a tropical cyclone approached a seismic station, the variation of atmospheric pressure would be observed quite strongly (Gherzi, 1932). Another presented cause was pressure changes above the ocean surface (Sholte, 1943). It was assumed that the amplitude of the compression waves generated by atmospheric

pressure oscillation above a broader region of ocean surface would be greater than the amplitude of surface gravity waves generated. Surface gravity waves, known as ocean waves, are generated as the force of gravity or buoyancy tries to restore equilibrium between the atmosphere and ocean. Therefore, atmospheric pressure oscillations do not explain how the ocean waves are generated.

None of these initial explanations proved to be the precise cause of microseism generation. Longuet-Higgins (1950) took the idea presented by Miche (1944) for explaining the cause of microseisms and improved it. According to Longuet-Higgins, microseisms with periods between 3–10 sec are generated as follows: two similar period ocean wave groups traveling in opposite directions interact nonlinearly to generate a standing wave in the ocean. The first-degree pressure fluctuations in a continuous ocean wave decrease with depth due to the potential energy of ocean wave train remaining at a constant level. Hence, there is no first-degree pressure fluctuation at the ocean bottom. However, the second-degree pressure fluctuations in a standing wave do not attenuate with depth, and so the pressure perturbation on the ocean floor would be significant. The corresponding displacement of the ocean floor will create surface waves propagating in all directions at half the period of the interacting ocean waves. Because this generated seismic energy has double the frequency of the interacting ocean waves (i.e., half the period of the interacting ocean waves), it is called the double-frequency microseism.

Hasselmann (1963) realized that microseisms with periods above 10 sec could not be explained by the Longuet-Higgins theory. He introduced a new generation mechanism for the longer-period microseisms that involved ocean waves shoaling along coastlines. The ocean wave energy was directly transferred to the solid earth at, or close to,

coastlines, with the same period as the ocean waves. Hence this energy is known as the single-frequency microseism, with dominant periods of 10–20 sec.

The study of microseisms in this dissertation was motivated by two fundamental questions in earth science: (1) Seismic noise can be used to image earth structure, especially in the crust and upper mantle. Gaps in tomography studies are filled and more uniform images are produced with the help of microseismic sources. However, because in most cases there is anisotropy in the noise field, the Greens functions recovered from the seismic noise can be biased. This biasing problem could be mitigated by determining more precise locations of the microseismic sources (Chevrot et al., 2007). (2) Unknown mechanisms in microseismic source generation from the interaction of atmosphere-ocean-solid earth system. It has been shown that the effect of global warming on the oceans can be studied by analyzing historical seismic records from the presatellite era (Grevemeyer et al., 2000). Results indicated that there has been an increase in storm and ocean wave activity in the Atlantic and the North and Central Pacific Oceans since the 1980s (Aster et al., 2008; Bromirski et al., 2005). Identifying more precise locations of microseismic sources would contribute to understanding whether the number of storms and their intensity may continue to increase. This would also help to understand how global warming is affecting the tracks of storms and their impact on coastal regions.

Motivated by these two general considerations, I investigated several fundamental questions related to microseisms: (1) Do microseisms generally propagate as Rayleigh waves or are Love waves as prevalent? (2) What are the source locations of double-frequency microseisms, close to coastal regions, in deep oceans, or both? (3) What are the dominant peak seismic periods for the North Atlantic and the Pacific Oceans? (4) Is

one ocean more dominant than the other in terms of generating certain peak seismic periods? (5) Does sea state (temperature, depth, ocean currents, etc.) affect the dominant seismic period or source region? That is, although the number of hurricanes and their intensities increased in the Atlantic, there could be some years with less intense storms due to the change in the weather systems and ocean currents. Can this be a reason for not observing longer period double frequency microseismic energy from the Atlantic? I set out to address these questions in the following thesis.

1.1 Review of Recent Literature

Microseisms have been studied since the 1900s. As a result, there are numerous studies related to microseisms. In this section, I review some recent studies that use polarization analysis to determine the microseismic source locations from the North and East Central Pacific Ocean and the North Atlantic Ocean.

Schulte-Pelkum et al. (2004) measured the direction and amplitude of microseisms generated in the North Pacific and the North Atlantic Oceans and recorded in southern California. They used 3-week long (12–31 January, 1998) continuous data from the Terrascope Broadband Seismic Network, ANZA broadband seismic array, and six stations from other networks. At each station, they determined the amplitude and direction of the microseisms using polarization analysis of the three-component record in the time domain. For the array, they measured the azimuth and slowness of microseisms by finding the peak power from slant-stacks of the continuous vertical seismograms. They also compared their seismic results with ocean wave height data taken from the recordings of California coastal buoys, a regional model taken from recordings of a deep-

ocean buoy, and wind-based regional and global ocean wave models. They identified three microseism source regions: two in the North Pacific Ocean and one in the Labrador region of the North Atlantic Ocean during their 3-week observation period. The North Pacific Ocean sources were located in the British Columbia region and off the coast of Baja California. They also tried to compare the microseism from the Labrador region with the 1991 "Perfect Storm" (also known as the Halloween Nor'easter of 1991 that evolved from absorbing Hurricane Grace as a nor'easter and became a new unnamed hurricane in the North Atlantic) microseism. They found that this microseism, originating from Labrador, was more powerful than the microseism generated by the 1991 event.

Chevrot et al. (2007) analyzed records of double-frequency microseisms for their arrival direction and amplitude using stations in Western Europe. They used 24 broadband stations in the Quercy region of France and 13 stations from the Grafenberg Array in Germany for the time period between 2 December, 2005, and 30 January, 2006. They also used individual stations with continuous LH channels: station MAHO from Menorca, station PAB from Spain, station SMPL from Corsica, station SSB from France, and station VSL from Sardinia for the time period of 2 December 2005 to 31 January 2006. They performed frequency slowness analysis for the array from the Quercy region and the Grafenberg array. For the individual stations, they used polarization and amplitude analyses. They compared their results with the significant wave heights produced by a second-generation ocean surface wave model developed by the French Meteorological Service, Marine and Oceanographic Section (Meteo-France). They identified locations of double-frequency microseism sources along the western coast of Menorca Island in the Mediterranean Sea, the Northern Galicia margin (off the coast of

Northwest Spain), and the western coast of Ireland in the Atlantic Ocean. They showed evidence that both coastal and deep ocean regions are capable of generating double-frequency microseisms. They also showed that swell reflection could explain the coastal sources at the Galicia margin and the western coast of Ireland, while for the deep ocean sources they hypothesized a nonlinear interaction between primary swell and wind sea as the cause.

Stutzmann et al. (2009) analyzed the effect of climate on seismic noise. They used 15 years of continuous data from the GEOSCOPE global seismic network. They computed the energy spectra of the stations and corrected the power spectral density estimates by removing the instrument response. They also performed polarization analyses of the double-frequency microseisms from eigen-analysis of three-component seismic data. They obtained back azimuths and the degree of polarization of the double-frequency microseisms. They found that the double-frequency microseism amplitude variations were global, and they depended on the latitude of the station and the season. They also observed that higher amplitudes were present in the local winter for both northern and southern hemispheres and that the dominant directions of the double-frequency microseisms changed seasonally.

Landes et al. (2010) determined the origin of deep-ocean microseisms using teleseismic body waves. In their first step, they used data from the Eastern Turkey Seismic Experiment (ETSE), a temporary array consisting of 20 broadband stations, for the time period of October 1999 to August 2001. They performed polarization analysis on the cross-correlated signals from the ETSE array and determined azimuths and incident angles of P-waves from the covariance matrix. In their next step, they performed

beamforming analysis on the data from three arrays, ETSE array, a temporary array deployment in Yellowstone, and an array from Kyrgyzstan, to locate P-wave noise sources in oceans. They found a significant part of the seismic noise was composed of P-waves generated by different sources. They also found that these sources had strong seasonality as a result of migration of oceanic storms between the northern and southern hemispheres. They noted that the location of P-wave microseismic sources in the single-frequency and double-frequency bands did not coincide, showing these sources were generated in different regions. They also showed that P-waves in the double-frequency microseism band were easier to identify than in the single-frequency microseism band.

Traer et al. (2012) used yearlong continuous data from USArray to identify source regions of long period seismic noise defined as hum and microseisms recorded for the period of September 2010 to August 2011. They also studied two special cases (Hurricane Irene and a Pacific swell) during their observation period. They beamformed the seismic data and then correlated the beam-former output with ocean wave hindcasts from all the oceans of the world. They divided the microseismic sources into two separate subcategories and labeled them as single frequency microseism and double frequency microseism sources. They showed that the dominant hum signals were produced along the Pacific coast of Central and South America for the Southern Hemisphere winter and the coasts of the North Pacific and Europe for the Northern Hemisphere winter. They also found that the dominant single-frequency microseism sources were generated along the coasts of Polynesia and Alaska for the Southern Hemisphere winter and Newfoundland and Greenland for the Northern Hemisphere winter. For the double-frequency microseism sources, they showed that during the Southern Hemisphere winter the coast

of South America and the Northern Hemisphere winter the east and west coast of North America were located as the main regions of double frequency microseism generations. They also found that the double-frequency microseism sources along the east and west coasts of Northern America were present during the southern hemisphere winter. Coastal regions generally showed higher correlation with the microseismic surface waves and wave heights than open ocean regions. Although their results indicated some of the double-frequency microseism energy observed by the USArray was produced close to the coastline, they mentioned that the double-frequency microseism sources could be generated at any ocean depth.

Sergeant et al. (2013) investigated variations in the seismic noise field close to the Polar region around Greenland. They used data for the calendar year of 2010 from stations of the Greenland Ice-Sheet Monitoring Network (GLISN), as well as stations from the global networks in North America and Europe. They performed frequency-dependent polarization analysis of the seismic signals for locating double-frequency microseismic sources within the period range of 3–20 sec. For determining polarization attributes, such as the semimajor and semiminor axes of the ellipse and the degree of polarization, they used eigen analysis of the cross-spectra between the three components of each station. They also computed a numerical ocean wave model including coastal reflections for source modeling. They identified sources along the Canadian coast extending close to mid-Atlantic Ridge and south of Greenland. They also showed that sea ice in the region of the Labrador Sea and Baffin Bay was the main cause of amplitude and the noise polarization modification at nearby stations. Furthermore, they found that noise from this region was only observed at shorter periods (3–4 sec) at nearby stations.

They explained not seeing longer-period seismic energy from the Labrador Sea and Baffin Bay as a result of shallow water depths in the region. They also concluded because of the small extent of the sea, the region might not be capable of generating longer-period ocean waves (larger than 10 sec).

1.2 Methodology

The methodology I used in this study is described in Koper and Hawley (2010) and is based on earlier work by Samson (1983) and Parks et al. (1987). The method determines polarization attributes from the eigenvalues and eigenvectors of the spectral covariance matrix using a sliding window and yields information on how the seismic energy is polarized. The covariance matrix is a function of time and frequency.

First, the instrument response is removed from each hour of data for each component, resulting in an acceleration time history with units of m/s^2. Then, each window is divided into 10 subwindows of length 819.2 seconds (32,768 samples), with each subwindow overlapping another by 62%. The sampling rate was 40 samples per second (Hz). For each subwindow, the trend was removed, and it was tapered using a 10% Hanning function.

The general formula of Hanning function is

$$w(n) = 0.5\left(1 - \cos\left(\frac{2\pi n}{N-1}\right)\right) \tag{1.1}$$

where N is the total number of points in a window, and n is given as n = 1, 2, …, N. Next, the discrete Fourier transforms of each subwindow are calculated:

$$Y^j(k) = \sum_{n=0}^{T_r-1} y^j(n) e^{-i\frac{2\pi}{T_r}nk} \quad (k = 0, 1, 2, \ldots, T_r - 1) \tag{1.2}$$

Here, T_r represents the length of the subwindow and j refers to the j^{th} component of the seismogram (north-south, east-west, up-down). Following the Fourier transform, the spectral covariance matrix, H(f), was calculated for each subwindow from multiplication of the Fourier transformed time series with their complex conjugates:

$$H(f) = \begin{pmatrix} Y^1Y^{1*} & Y^2Y^{1*} & Y^3Y^{1*} \\ Y^1Y^{2*} & Y^2Y^{2*} & Y^3Y^{2*} \\ Y^1Y^{3*} & Y^2Y^{3*} & Y^3Y^{3*} \end{pmatrix} \tag{1.3}$$

where the star indicates a complex conjugate. The matrix is a 3×3 Hermitian matrix, and the elements are a function of frequency. The diagonal elements are the power spectra of each component, while the off-diagonal elements represent the cross-spectra. The 10 covariance matrices for each subwindow are then linearly averaged to produce the total covariance matrix, corresponding to the original 1-hour segment of data. For determining the eigenvalues and eigenvectors of the covariance matrix, eigenvalue decomposition was performed.

The polarization vector, $\hat{z}$, is the eigenvector corresponding to the largest eigenvalue of matrix H. It defines the particle motion at a frequency containing the largest portion of the seismic energy. The components of $\hat{z}$ can be complex, which gives phase lags between components, representing elliptical particle motion.

Figure 1.1 shows the polarization ellipsoid and definitions of polarization angles

of $\mathbf{\Theta}_H$ and $\mathbf{\Theta}_V$ and the complex eigenvector $\hat{z}$, which describes the particle motion projected onto an ellipse in the horizontal plane defined as

$$z_H = \hat{z} - (\hat{e}_1 . \hat{z})\hat{e}_1 \tag{1.4}$$

where $\hat{e}_1$ = (1, 0, 0). The major axis of the horizontal ellipse represents the principal direction of horizontally polarized motion. In order to find the azimuth of the major axis, Parks et al. (1987) searched the maximum value for determining the point of greatest displacement for the projection $\hat{z}$ in the horizontal plane using

$$\left|Re(z_H e^{i2\pi ft})\right|^2 \tag{1.5}$$

They expressed the vector $\hat{z}$ components (z_1, z_2, z_3) in the form

$$z_j = |z_j| e^{i\phi_j} \tag{1.6}$$

which is equivalent to finding the maxima of

$$|z_2|^2 cos^2(2\pi ft + \phi_2) + |z_3|^2 cos^2(2\pi ft + \phi_3) \tag{1.7}$$

The extremes of equation (1.7), remembering the equation of

$$|z_2|^2 sin^2 2\phi_2 + |z_3|^2 sin^2 2\phi_3 = Im[z_2^2 + z_3^2] \tag{1.8}$$

can be found by defining the phase angle , θ, as $\theta = 2\pi ft$ taking the values of

$$\theta_\ell = -1/2 arg[z_2^2 + z_3^2] + \frac{\ell\pi}{2} \tag{1.9}$$

where ℓ is an integer and arg is the argument function to determine angle between the line joining the point to the origin and real axis. ℓ is taken to be the integer closest to zero, minimizing eqution 1.7, the horizontal displacement, and for $Re(z_1) < 0$. This ℓ value defines the phase angle θ_H ($\theta_H = \theta_\ell$). When θ_H is found, the horizontal azimuth of the major axis Θ_H,which is measured counterclockwise from $\hat{e}_2$=(0, 1, 0), can be defined as

$$\Theta_H = \tan^{-1}\left[\frac{Re(z_3 e^{-i\theta_H})}{Re(z_2 e^{-i\theta_H})}\right] = Re(\tan^{-1}(z_3/z_2)) \tag{1.10}$$

If $Re(z_1 z_3^*) < 0$, Θ_H is between $0° < \Theta_H \leq 180°$, and if $Re(z_1 z_3^*) \geq 0$, then Θ_H is between $-180° < \Theta_H \leq 0°$. If the particle motion is similar to P-wave particle motion, it could be said that Θ_H points in the direction of wave motion.

Another important property is the phase difference between the horizontal components of particle motion, ϕ_{HH}. It is given as

$$\phi_{HH} = \phi_3 - \phi_2 \tag{1.11}$$

If $\phi_3 - \phi_2 = 0°$ or 180°, the particle motion is predominantly linear, while if $\phi_3 - \phi_2 = 90°$, then the phase difference between the horizontals represents elliptical motion,

where the major and minor axes of the ellipse are oriented along the axes of a seismometer.

Θ_V is the angle between the vertical and the major axis of the ellipse, and it can also be defined as the angle of incidence (Figure 1.1). The phase angles are defined as

$$\theta_m = 2\pi ft = -\frac{1}{2} arg[z_1^2 + z_H^2] + \frac{m\pi}{2} \tag{1.12}$$

where m is an integer and $z_H^2 = z_2^2 + z_3^2$. The phase angle θ_V is taken as θ_m at a value of m in which particle motion displacement is maximized. Thus the angle of incidence is given as

$$\Theta_V = \tan^{-1}\left[\left|\frac{Re[z_1 e^{-i\theta_V}]}{Re[z_H e^{-i\theta_V}]}\right|\right] \tag{1.13}$$

Equation 1.13 is valid where imaginary part of $z_H \geq 0$. The reason for using absolute value in the arctangent is to restrict the incidence angle values in the range of 0° to 90°.

The phase difference between the vertical and horizontal components, ϕ_{VH} shows whether the particle motion is elliptical or not. It is

$$\phi_{VH} = \phi_H - \phi_1 \tag{1.14}$$

The values of ϕ_{VH} vary between -90° and 90°. If the value is -90°, this indicates that the particle motion is retrograde and the propagating seismic energy is a standard Rayleigh

wave. If the value of ϕ_{VH} is 90°, the propagating seismic energy may still be a standard Rayleigh wave, but with a 180° change in the back azimuth.

Samson (1983) described another important parameter called degree of polarization (β^2). This parameter defines whether the propagating seismic noise is organized or not. In other words, it measures the strength and coherence of the seismic noise. The higher the value (β^2), the more singular the seismic noise. β^2 is defined as

$$\beta^2 = \frac{3t(H^2) - [t(H)]^2}{2[t(H)]^2} \tag{1.15}$$

where *t* is the trace (the sum of diagonals) of H and H is the spectral covariance matrix. The value of β^2 varies between 0 and 1 and is a function of frequency. If β^2 is 0, all the eigen values are equal to each other. If β^2 is 1, there is only one nonzero eigenvalue present.

1.3 Description of Chapters

In Chapter 2, I report on analysis of microseisms recorded by the Earthscope Transportable Array (TA) during the calendar year of 2009. The chapter focuses on categorization of the microseisms into distinct classes (I–IV). Microseismic properties such as duration, polarization direction, maximum observed power, and the period content are noted and compared to predictions from a model of ocean wave activity. I found two distinct dominant periods within the double-frequency microseism band, 5-sec and 8-sec, and I described how they varied as a function of time throughout 2009. Chapter 3 uses similar methods but focuses on TA recordings during Hurricane Sandy in

2012. It was published in Earth and Planetary Science Letters in 2014 (Sufri et al., 2014). Chapter 4 summarizes the principle conclusions from my research and suggests the next steps to follow from my study.

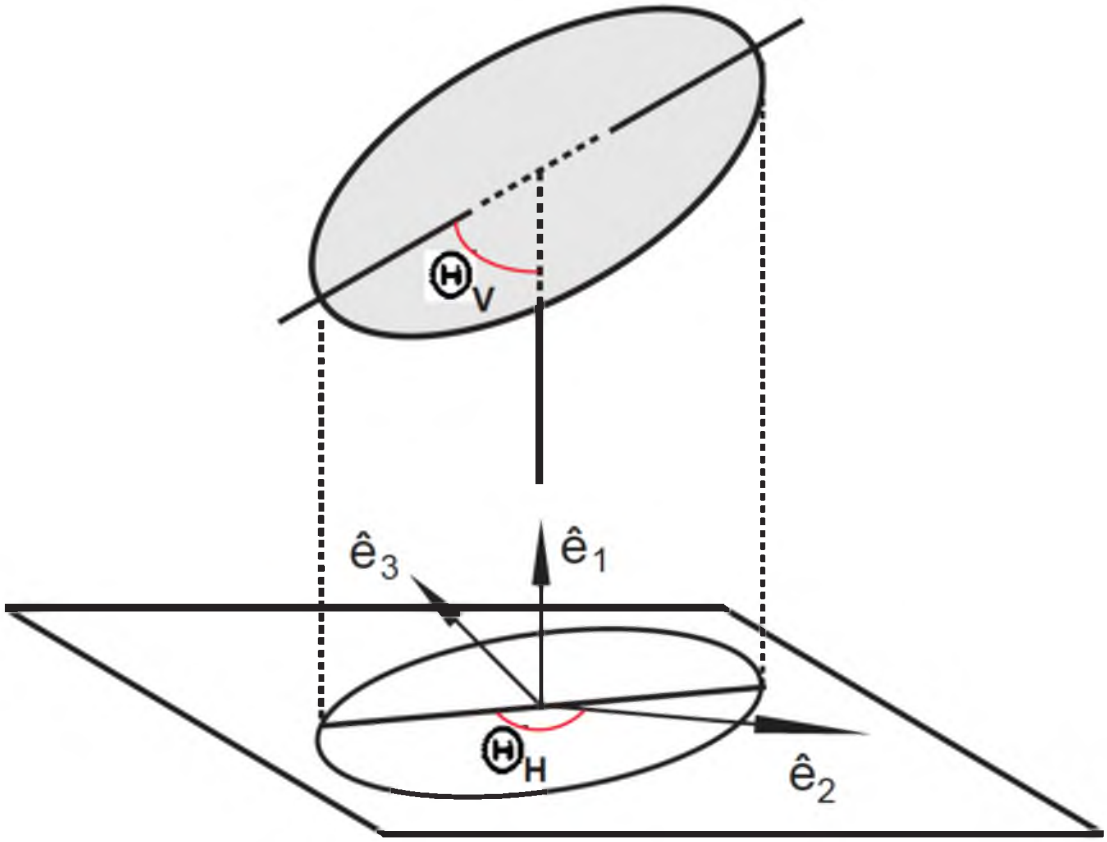

Figure 1.1 Illustration of the polarization angles of Θ_H and Θ_V. The azimuth, Θ_H, is measured counterclockwise from $\hat{e}_2$ and restricted between -180° and 180°. e_1, e_2, and e_3 are the vectors normal to the horizontal plane. These vectors are used as coordinate system to project the long axis of polarization ellipsoid to a horizontal plane. The ellipticity of the particle motion is defined by the amplitudes $|z_1|$, $|z_2|$, and $|z_3|$ and the phase angles Φ_{HH} and Φ_{VH} (defined in the text) (Adapted from Park et al., 1987).

CHAPTER 2

A MICROSEISM CATALOG FOR THE YEAR OF 2009

In this chapter, I catalog and categorize microseisms recorded by the Earthscope Transportable Array for the calendar year of 2009 in order to analyze the similarities and differences of noise sources. I used monthly spectrograms and polarization attributes, extracted via eigen value decomposition of the covariance matrix, for determining the properties of microseisms. I defined four different types of microseisms according to the peak power values, shape, and the period content in the double-frequency band of spectrograms. I also compared the seismic results with predictions of ocean wave models of significant wave heights, power spectral density of equivalent surface pressure, and peak period, computed by the French Research Institute for Exploitation of the Sea (IFREMER, August 22, 2014), to determine whether the seismic results are consistent with ocean wave sources. I then investigated two distinct periods within the double-frequency microseism band in terms of seasonal changes in array-averaged power and degree of polarization. Finally, I estimated the locations of those four types of microseisms in the discussion part.

2.1 Data

I processed continuous seismic data for the entire year of 2009 from the IRIS Data Management Center (DMC). The data were sent in two external hard drive from the DMC in miniseed format. The data were sampled at 40 samples per second, and there were 585 Transportable Array (TA) stations active during some part of 2009. Each station had a single miniseed file that included all three components (BHZ, BHN, and BHE). The station response files were downloaded from the IRIS DMC. A small program was written to convert the year-long miniseed files into hour-long Seismic Analysis Code (SAC) files for each component of each station. At the end of this process, the data size was 1.4 Terabytes.

Figure 2.1 shows the availability of data for each station. It can be seen that the centermost stations and the backbone stations had almost a complete year of data. On the other hand, stations on the west and east edges of the network, and also stations located in the Pacific Northwest, had the least available data. This was because the stations on the western part of the TA network were being moved to the east end of the network in order to continue marching the array across the conterminous United States. This rolling type of coverage was the main feature of the Earthscope Transportable Array program. Earthscope aimed to image the crustal and upper mantle structure of North America and understand how tectonic and volcanic events shaped the geology of the region.

One of the main advantages of having backbone stations in the east and southwest was to better constrain the direction from which the microseismic energy was arriving. For some microseisms with a dominant period below 5 sec, I had difficulties determining the source. In these cases, the reference stations were quite helpful in figuring out the

source location and how the energy was propagating.

2.2 Processing

The technique I used in this chapter is based on the techniques developed by Samson (1983) and Park et al. (1987) and described by Koper and Hawley (2010). Detailed description of the theory and equations used is also given in Chapter 1.

Figure 2.2 shows the flow chart of how the data were processed. The first step was selecting a 1-hour time window from each component of the data. If a station did not have three continuous components for the entire hour, that station was omitted from processing for that hour. Next, each 1-hour long time window was detrended and the instrument response removed. Following that, each time window was divided into 10 subwindows, and each subwindow was tapered with a 10% Hanning function. The Fourier transform was performed on each subwindow of each component. Then, the spectral covariance matrices were calculated, and the 10 covariance matrices were linearly averaged to obtain the overall covariance matrix of the original 1-hour segment of data. The diagonal elements in the covariance matrix represent the power spectra of each component, whereas the off-diagonal elements represent cross-spectra between the components. Next, eigenvalue decomposition was performed and the polarization attributes were extracted from the eigenvalues and eigenvectors. A base 10 logarithm averaging scheme was applied to reduce the number of frequency bins from 32,768 to 301. After averaging, the lowest value of the frequency bin was 0.00123 Hz while the highest value was 19.9526 Hz. This averaging scheme helped to lessen the amount of time for processing and interpreting the results. In order to interpret the results, spatial

animations were made for eigen power, polarization, and peak seismic period.

2.3 Ocean Wave Models

Ocean wave models were taken from the Ifremer web page. The models were developed by Ifremer and the University of Darmstadt using the existing WAVEWATCH III ocean wave model, originally developed by Hendrik Tolman (Tolman, 2002). Ardhuin and Herbers (2013) defined the equivalent surface pressure as the equation involving the sum of amplitudes, wave numbers, and frequencies of interacting ocean waves as a function of time. They also defined the power spectral density of the equivalent surface pressure in three dimensions (K_x, K_y, f_s) using the Fourier amplitudes of the forcing equivalent surface pressure. K_x is the x-component of the wavenumber vector. K_y is the y-component of the wavenumber vector, and f_s is the double-frequency of the interacting ocean waves.

The file formats were netcdf, and they were downloaded from the ftp site (ftp://ftp.ifremer.fr/ifremer/cersat/products/gridded/wavewatch3/iowaga/SISMO/GLOBAL05_2009_REF10_20_40/). Three types of netcdf files were used from the website for the year of 2009: the significant wave heights (hs), peak period and power spectral density of equivalent surface pressure (p2s), and the base-10 logarithm of power spectral density of equivalent surface pressure (p2l). Each file was a month long, and all months for each file were downloaded. In order to read the netcdf files, matlab code was also downloaded from the Ifremer ftp site. For processing (averaging, etc.), plotting, and making animations, I developed my own custom matlab codes.

The significant wave height (hs) netcdf files had the time, geographical location

(latitude and longitude), and wave height information for each location. The time started with the first day of the month, 00:00 UTC hour, and ended with the last day of month, 21:00 UTC hour. The time increment was 3 hours. For the location, the latitude range was defined between -78° and 80° in increments of 0.5°, and the longitude range was defined in between 179.5° and -180° in increments of 0.5°. Significant wave height was given in meters.

The second netcdf file, peak period and power of the power spectral density of equivalent surface pressure (p2s), had the same time and geographical coordinate information as the hs netcdf file. The other contents of this file were peak period and peak power given for each latitude and longitude in 3-hr intervals. The units of the peak period and peak power were seconds and m^4, respectively. I used the peak period information for plotting and comparing the peak seismic period with the peak ocean wave periods.

The p2l netcdf files had the same data interval (3 hours) and the same geographical boundaries as the other two netcdf files. The main difference from the p2s netcdf files was that there were 16 defined ocean wave frequencies, and each frequency had the corresponding base-10 logarithm of power values defined every 3 hours for each latitude and longitude. The 16 frequencies were 0.0410, 0.0451, 0.0496, 0.0546, 0.0601, 0.0661, 0.0727, 0.0800, 0.0880, 0.0967, 0.1064, 0.1171, 0.1288, 0.1416, 0.1558, and 0.1714 Hz. The power values from individual frequencies and the averaged power values from desired frequency ranges were used to support and interpret my results from polarization analyses of seismic data.

2.4 Results

I catalogued and grouped microseisms according to their properties observed on monthly array-averaged spectrograms of dominant eigenvalue power. First, I studied the shape of microseisms in the double-frequency band to determine whether they were wide, narrow, or had a certain shape (for instance if the shape of microseism skewed toward shorter periods or longer periods as time progressed). Then, I compared the seismic power of the similarly shaped microseisms in each group and defined a threshold power required in order to be considered as part of that group. Finally, I used the polarization vectors and principal eigenvalue amplitudes of individual stations for the 3 sec, 5 sec, and 8 sec periods to determine dominant polarization directions. Thus, I categorized microseisms into four different groups, referred to as Types I, II, III, and IV.

For Type I microseisms, the power first appears at the longer period of the double-frequency microseism band. As time progresses, the power shifts to shorter periods (close to 6 sec). In other words, the Type I microseisms showed dispersive behavior, similar to the frequency dependence of surface wave velocity known as surface wave dispersion. In order to place a microseism in this category, its power had to be larger than -130 dB. This threshold was selected from the comparison of peak power of the microseisms from each month and from looking at the seismic amplitude distribution throughout the TA stations during the passage of those microseisms. A first order observation was that microseisms occurred in the summer months were weaker and their peak power were less than -130 dB. Thus, they were not selected for this category.

For Type II microseisms reverse dispersion is observed. That is to say, as time progresses, the seismic energy shifts from shorter periods (2–3 sec) to longer periods

(between 5 and 6 sec). There were two criteria in order to classify a microseism as Type II. First, its power had to be larger than -130 dB, as for the Type I category. Second, the upper limit of its period range had to be smaller than 6 sec.

For Type III and Type IV microseisms, I determined the width of the period range of the double-frequency microseism band by looking at the array-averaged monthly spectrograms and measuring the width of period range in the double frequency microseism band for each microseism. If the period range was larger than or equal to 5 sec and power greater than -120 dB, I labeled Type III. Otherwise I labeled it Type IV. The thresholds were determined from the comparisons of spectrograms of different months, and polarization vectors and eigen amplitudes of individual stations throughout the whole year. The main reason for the thresholds was to eliminate weak seismic noise and focus on stronger microseisms. I observed that the stronger Type III and Type IV microseisms tended to have a wider double frequency microseism range, and the polarization vectors for different periods (such as 3, 5, and 6 sec) had a higher degree of polarization than the Type I, and Type II had.

The properties of the four types of microseisms are given in Table 2.1, Table 2.2, Table 2.3, and Table 2.4, respectively. The relevant properties of microseisms that are reported are the date of observation, duration of the microseism, primary polarization direction, location of the microseism, array-averaged peak seismic power and peak seismic period, and the period range. I determined the location information by comparing the computed ocean wave models with the polarization directions and the seismic amplitudes from each station of the TA network. Since the microseisms are not stationary (they propagate according to the weather patterns, moving storm systems, and the ocean

wave currents), the directions indicate where the microseisms first appeared in reference to the TA network.

The tables also indicate if the microseisms have a single-frequency component. In some cases, the single-frequency microseism band imitated the shape of the microseism in the double-frequency band. This indicated that the microseism source likely generated seismic energy close to the coastline because of ocean wave interaction with the coast. Thus I pointed out whether a microseism originated in the deep ocean or along a coast within this column by answering the question as "Yes" or "No." I also used "not clear" as an answer in some cases, where either the microseism had a very weak single-frequency component or some large earthquakes were present that masked potential single-frequency microseismic energy.

2.4.1 Type I Microseisms

I counted 30 Type I microseisms during the year of 2009. Table 2.1 shows the detailed information for these events. I found that nine microseisms originated from the Gulf of Alaska, 10 from the Pacific coast of Southern Mexico, nine from Southern California and Baja California, and two microseisms originated in the North Atlantic Ocean. One of those two microseisms from the North Atlantic Ocean originated from close to the coast of Newfoundland. The other originated close to the northeast coast of the United States. This latter microseism was coincident with the passage of Hurricane Bill.

2.4.1.1 Gulf of Alaska

The nine microseisms from the Gulf of Alaska occurred during the winter, spring, and fall months of 2009. There were no microseisms originating from this region in the summer months. This is consistent with the fact that most northern hemisphere storms occur during the northern hemisphere winter months. The array-averaged peak seismic period ranged between 7.4–8.5 sec, with a median of 8.1 sec. There were three microseisms that had short duration (less than 24 hours): one from January of 17 hours, another from February of 20 hours, and the third during September had a 16-hour duration. As for seismic power, the strongest microseism occurred between October 21–24, having an array-averaged peak power of -110.7 dB.

Figure 2.3 shows the array-averaged spectrogram for October. The black ellipse indicates the power and period content of a microseism recorded by the TA stations. It is noticeable that there was significant seismic energy (peak power of -135 dB) at the single-frequency periods of 10–20 sec in the microseisms and that many earthquakes occurred during this month. Figure 2.4 shows the averaged ocean wave spectra of the time of this microseism versus time-averaged polarization (Figure 2.4a) and power (Figure 2.4b) for October 21–24. Since these figures show the time-averaged response of the TA stations, they do not indicate how this microseism propagated from the Gulf of Alaska to off-the-coast of Southern California. For the ocean wave spectra, the data were averaged over the periods of 12.5 sec and 18.3 sec for each 3-hour block, and the time averaging was performed for October 21–23. For the seismic amplitudes, I averaged periods between 6.2 sec and 9.1 sec for each hour, and I performed time averaging for the same dates as the ocean wave spectra averaging.

Polarization vectors were calculated using weighted averaging (by degree of polarization). First, I used the polarization direction (azimuth) and corresponding degree of polarization in the weighted-average for each hour. At the same time, I performed simple averaging of the degree of polarization for given periods. Then, I did linear time averaging for the polarization directions and degree of polarization. Finally, I plotted the averaged polarization directions for each station with different vector lengths (by using the averaged degree of polarization values). Most of the stations had east-west alignment, while some stations had their polarization vectors oriented in the northwest-southeast direction (Figure 2.4a). Considering that there were no strong microseisms in the Atlantic Ocean and the Gulf of Mexico, the direction of these vectors supported the idea that the source of this seismic energy was in the Pacific Ocean. Higher seismic amplitudes on the western portion of the TA network also support this conclusion (Figure 2.4b).

Figure 2.5 shows the dominant ocean wave period and dominant seismic period for October 21–23. In order to determine the dominant seismic period, I searched for the maximum seismic power for the periods of 1–10 sec for each station and for each hour. Then, I linearly averaged the corresponding dominant seismic periods over the time window and plotted them on the map in Figure 2.5. The dominant ocean wave periods were also averaged for October 21–23 and plotted in Figure 2.5. Because the double-frequency microseism band defines the period of the seismic waves as half the period of the ocean waves, I used the same scale by taking half of the dominant ocean wave periods. As shown in Figure 2.5, except for the northeast corner of the TA network, all the stations had dominant seismic periods between 6.5 and 7.5 sec. In terms of ocean wave periods, along the Pacific coast (from Gulf of Alaska to the tip of Baja California)

the dominant ocean wave period was between 13 and 15 seconds. The Pacific coast of Southern Mexico also had a dominant ocean wave period around 15 sec.

It could be said that the ocean wave-wave interaction in this region might have dominated the southern stations and even the west-northwest stations of the TA network. However, because of the east-west orientation of the polarization vectors (Figure 2.4a), the dominant source region was most likely along the west coast of the United States. There were also three powerful microseisms likely originating from this region: one occurring March 27–29 having array-averaged peak power of -112.7 dB, one from April 5–8 with the peak power of -113.3 dB, and another occurring November 25–27 with array-averaged peak power of -116.8 dB. These powerful microseisms lasted more than 24 hours as they propagated to the south along the western United States coast.

Nearly all of the microseisms originating from the Gulf of Alaska showed a significant single-frequency component. Since the single frequency microseisms have the same period as the ocean waves near the coastline and they are generated by the interaction of the ocean waves with a shallowing ocean bottom, this indicates the seismic energy from these microseismic sources was generated close to the coastline. One exception occurred for April 5–8. An explanation could be that there were several moderate magnitude earthquakes during the passage of this microseism: a M6.3 from Central Italy on April 6, a M5.6 from Tonga Region again on April 6, a M6.9 and several aftershocks with magnitude larger than 4.0 from Kuril Islands, and a M4.5 from Alaska on April 7. It is possible that these earthquakes might have dominated the single-frequency band. Alternatively, there is the possibility that this source might have a deep ocean origin.

2.4.1.2 Pacific Coast

The second group of Type I microseisms originated from the Pacific coast of Southern Mexico during the spring and summer months of 2009, mostly April, June, and July, except for one microseism that occurred October 3–5. The array-averaged peak seismic periods were between 7.7 and 8.9 sec with a median of 8.2 seconds. The array-averaged seismic power was weaker compared to that of microseisms from the Gulf of Alaska. Except for one microseismic source observed July 23–27, all other microseismic sources had array-averaged peak power between -121.3 dB and -129.5 dB.

The microseism from July 23–27 had the longest duration (~107 hours) in this group and had a longer duration than the entire Type I microseism group. Figure 2.6 shows the July spectrogram with a black ellipse encircling the microseism. The seismic data were averaged over periods of 6 sec and 9 sec for each hour and the time averaging was done over 100 hours for July 23–27. Additionally, ocean wave spectra were linearly averaged between 12.5 sec and 18.3 sec for the period averaging, and during July 23–27 for the time averaging. Figure 2.7a and Figure 2.7b show comparisons of averaged polarization vectors for each station and ocean wave spectra and the average seismic power versus ocean wave spectra, respectively. Although some stations in the network had their polarization vectors aligned east-west, many north-south and southwest-northeast alignments are also visible (Figure 2.7a). On the other hand, it was difficult to detect directivity from the averaged seismic amplitudes in Figure 2.7b.

Comparison of the average dominant seismic period versus average dominant ocean wave period best indicates that the microseismic sources occurred along the southern coast of Mexico and along the coast of Baja California (Figure 2.8). The average

dominant seismic period was approximately 8 sec, while the average dominant ocean wave period for these regions was around 16 sec. Except for the July 21–23 source, all microseisms from this region had a single-frequency component. Thus, microseisms from this region were generated close to the coastline. The July 21–23 microseism either did not generate any seismic energy in the single-frequency band, or the seismic energy at these periods (10 and 20 sec) was not as strong as the other microseisms.

2.4.1.3 Southern California and Baja California

The third group of Type I microseisms originated along the coast of Southern California and Baja California. Although there were seasonal patterns for microseisms originating from the Gulf of Alaska and the Pacific coast of Southern Mexico, there was no specific seasonality for microseismic sources from this region. There were three microseisms that occurred in the spring months (March and April) and four microseisms that occurred in the fall months (September and October). Except for the two microseisms from June and December, it could be said that this region had more coherent seismic energy in the fall and spring months. The average peak period varied between 6.9–9.3 sec with a 7.4 sec median. Even though the period range of these microseisms was similar to microseisms from other regions (6.0 sec to 10.0 sec), the median peak period for the California region was less than the median period of the microseisms from the Gulf of Alaska and the Pacific coast of southern Mexico.

The array-averaged seismic power for the microseisms from Southern California and Baja California was between -125.6 and -113.7 dB. Except for two microseismic sources from October 20–21 and December 5–6, the remainder of the sources had a

longer duration (i.e., more than 24 hours). Three of the microseisms had a clear single-frequency component (two from April and one from December). Hence, these microseismic sources were generated close to the coastline. However, the majority of microseisms either did not have a single frequency component, or large teleseismic earthquakes may have masked the single-frequency microseism band. For instance there were two M5.9 earthquakes from Costa Rica during the passage of the March 10–12 microseism. Another example was during September 1–3; a M7.0 earthquake in Java occurred on September 2 and dominated the single frequency microseism band for several hours.

2.4.1.4. North Atlantic Ocean

The TA stations recorded two Type I microseisms originating from the North Atlantic Ocean, one in July and the other in August. The first, recorded on July 15th, originated in the vicinity of Newfoundland. The array-averaged seismic power of this microseism was -128.3 dB, and the corresponding array-averaged peak period was 6.3 seconds. Although a M7.8 earthquake from off the coast of the South Island of New Zealand dominated the single-frequency band for several hours, there was weak energy at the periods of 11–16 sec mimicking the period shift observed in the double frequency microseismic band. Further comparison of seismic results and the ocean wave model revealed this was a coastal source.

The second microseism (August 22–24) was associated with the passage of Hurricane Bill. This microseism was more powerful than the July 15 microseism. The observed maximum seismic power was -114.8 dB, and the corresponding array-averaged

peak period was 8.1 seconds. The period range of this source varied between 7.1 and 9.7 seconds. It was observed for more than 30 hours as the hurricane was propagating in the North Atlantic Ocean. Because there were station calibrations on the TA network from August 25 to August 31, the seismic records were contaminated. Also, considering Hurricane Bill's continuous motion towards the northeast from the end of August 24, away from the east coast, there were no clear observations of double-frequency microseismic energy coming from the northeast. There was strong single-frequency microseismic energy for the time period of August 22–24. This indicated that the microseisms generated during the passage of Bill probably originated close to the east coast.

2.4.2 Type II Microseisms

There were 11 Type II microseisms during 2009 (Table 2.2). As mentioned previously, these microseismic sources had period ranges of 2.8–5.8 s and reverse dispersion (i.e., a shift from shorter periods to longer periods). Except for the microseism of June 6–9, all microseisms had durations between 12 and 35 hours. The average seismic peak period was between 3.8 and 5.1 sec with a median of 4.3 sec. Analyses of polarization vectors and seismic amplitudes of individual stations revealed that these microseismic sources did not dominate all the stations in the network. For instance, if there was a Type II microseism originating from the Gulf of Mexico, only stations in the southeast corner of the array showed seismic energy arriving from the appropriate direction. The rest of the network stations were either dominated by energy coming from microseisms in the Pacific or Atlantic Oceans or they did not respond at all.

By comparing the seismic observations with the models of ocean wave spectra, I found that six of these sources originated from the Gulf of Mexico, while four were associated with the North Atlantic region. The period of October 23–24 showed that two sources from different regions contributed to the eigen power on the October 2009 spectrogram (one from the Gulf of Mexico, the other one from Newfoundland Region in the Atlantic Ocean). Further analysis of the other Type II microseisms indicated that indeed there were contributions from both regions, but with one region being more dominant than the other.

Figure 2.9 shows the array-averaged spectrogram for December. The black ellipse indicates the duration, period, and power content of a Type II microseism that occurred December 24–25. In general, December had quite strong microseisms, and this specific Type-II microseism could be recognized from its unique shape and its power. Furthermore, the single-frequency microseism band showed that there were many strong microseisms originating from coastal regions. Although the December 24–25 microseism had a single-frequency component, as indicated in Table 2.2, most of the Type II microseisms did not have significant single-frequency energy. As mentioned previously, this was either because of earthquakes dominating the single frequency band while the microseisms were being recorded or because of weaker power on the 10–20 sec band during the passage of a microseism. Another reason could be that there were other types of microseisms present (for instance Type III or Type IV) while the Type II microseisms were appearing, and the single-frequency component of those types might have been stronger than the Type II. Thus, the single-frequency microseism band could possibly be dominated by these other type microseisms energy.

I also observed energy at periods of 30–50 sec when these Type II microseisms were being recorded (Figure 2.9). Although there were some earthquakes coinciding with the passage of the microseism from December 24–25, it is hard to tell if either of the earthquakes were responsible for this long-period energy. Figure 2.10a and Figure 2.10b summarize and compare the seismic observations with the ocean wave spectra models. Since the array-averaged spectrogram indicated the microseism of December 24–25 lasted 32 hours with periods of 2.8–5.1 sec, I did the time and period averaging based on this 32 hour duration and the period content (2.8–5.1 sec), respectively. For the ocean wave model, the period averaging was performed between 5.8–10.3 sec, at double the period of the seismic energy.

Figure 2.10a shows the polarization direction of individual stations and the averaged ocean wave spectra. There was a strong and large source in the Gulf of Mexico. The southeast corner stations of the TA network had their polarization vectors aligned in southeast-northwest directions. At the same time, some central east and northeast stations had north-south polarization directions. Thus, it could be said this microseism was observed strongly at southeast corner stations, some stations in the northeast, and the eastern portion of the TA network. The seismic power of the southeast and some eastern stations in Figure 2.10b supported this.

On the northeastern portion of the TA network and some central stations, there was dominant energy coming from the northeast. The averaged ocean wave spectra in Figure 2.10a and Figure 2.10b support this observation. The model indicated a large and strong source stretching from Newfoundland to almost the mid-Atlantic region in longitude, and from Baffin way to the southeast of the Newfoundland region in latitude.

Meanwhile, there was another, broader, microseismic source in the northern part of the Pacific Ocean. The northwest corner stations and some other stations throughout the TA network indicated the seismic energy from this region was effective with polarization vectors aligned northwest-southeast.

Figure 2.11 shows a comparison of time-averaged dominant seismic periods and time-averaged ocean wave periods. The southeast corner of the network had the seismic period of 4–5 sec while the ocean wave period in the Gulf of Mexico was 8–10 sec. Similarly the eastern portion of the TA network and a few backbone stations from the east had average seismic period around 5 sec. The North Atlantic Ocean had ocean wave periods around 10 sec. These results are also consistent with the results from Figure 2.10a and 2.10b.

2.4.3 Type III Microseisms

I identified 11 microseisms that matched the criteria of Type III. As described earlier, the criteria for Type III microseisms were if the period range of the double-frequency microseism band was equal to or larger than 5 sec, and the peak power of the microseism was equal to or larger than -120 dB. Table 2.3 shows detailed information of these microseisms. The most intriguing observation from this table is that except for two microseisms occurring in January and October, the other microseisms were generated from multiple locations. In other words, multiple sources from two oceans contributed to each microseismic arrival. I indicated this by supplying more than one polarization direction in the table. The recording from January 14–19 indicated that a source region in the Baffin Bay and a large source region between Newfoundland and the south tip of

Greenland were responsible for generating this microseism. During October 11–14, a coastal source in the Newfoundland region generated microseismic energy, which was also listed in the table.

The average peak seismic periods for Type III microseisms were between 5.4–8.7 sec with a median of 6.3 sec. In terms of duration, except for the microseism recorded September 10–12, all others had durations greater than 72 hours. I did not find any increasing or decreasing trend in duration as the year progressed. Also, the number of microseisms each month had an irregular distribution. There were no Type III microseisms in the spring and summer of 2009. Thus, it could be said the Type III microseisms were mostly active during the winter and fall months. Additionally, the most active month was December (Figure 2.9). This is because the stormiest season of the year in the northern hemisphere is winter.

All Type III microseisms were more powerful than Type I and Type II microseisms. The average peak seismic power was between -113.7 and -101.2 dB. The most powerful microseism was recorded on December 28–31, 2009, with array-averaged seismic power of -101.2 dB (the green rectangle region in Figure 2.9). Figure 2.12a shows a comparison of time, period-averaged polarization vectors, and ocean wave spectra. The period averaging of the polarization vectors was performed for the periods of 2.8 sec and 9 sec. The ocean wave spectra period averaging was performed between 5.8 sec and 18.3 sec. The general trend of the polarization directions was east-west. However, clear northeast-southwest orientations can be seen. In fact, the different azimuths of these northeast-southwest oriented polarization vectors indicated a possible intersection at a broad region off the coast of Newfoundland and Labrador. The polarization directions

from the backbone stations, located to the east, also supported this observation. The main explanation for a general east-west trend of polarization vectors could be related to the several small microseismic sources located along the west coast of the United States.

Figure 2.12b shows how the averaged eigen amplitudes responded to sources in the Atlantic and Pacific Oceans. Although the amplitudes were generally high for this broad period range (2.8–9.0 sec), the eastward skewed amplitude map indicated that sources in the Northern Atlantic Ocean were slightly stronger than other sources in the north and east central part of the Pacific Ocean. The map showed three regions with large power (above -110 dB). Two regions were located in the Great Plains, and the other one was located to the southeast corner of the network. The main reason of having high amplitudes in the Great Plains regions was because of the existence of sedimentary basins. These basins consist of sandstone, clay, clay-shale, silt, sand, and also gravel in some regions (http://mrdata.usgs.gov/geology/state/). When seismic energy from a microseism in the North Atlantic Ocean propagates through these sedimentary basins, the basins amplify seismic energy. The southeast corner, on the other hand, might have been affected by the microseisms in the east central Pacific and the North Atlantic oceans. Although the stations in this part of the network were closer to the coast, there were no strong microseisms in the Gulf of Mexico for December 28–31 (Figure 2.12b). Thus the sources from the Atlantic and Pacific Oceans likely produced the large amplitudes in the southeastern corner stations of the TA network.

Figure 2.13 shows comparison of time-averaged dominant peak seismic periods and dominant ocean wave periods. The northeast, northwest, east central, and southeast corner stations average dominant peak seismic periods are in agreement with sources

from the Atlantic region. The dominant peak seismic period for those stations was around 6 sec, while the dominant ocean wave period in the northern Atlantic was around 12 sec. However, it could be possible that some of the stations in the northwest corner might have been affected by seismic energy generated in the northern Pacific Ocean, Gulf of Alaska, and Queen Charlotte Islands Regions. The other stations with average dominant peak seismic periods of 6–7 sec were most likely induced by the 12–14 sec ocean wave-wave interactions occurring in a broader region from the east central Pacific ocean (from off-the coast of Southern California to the tip of Baja California).

2.4.4 Type IV Microseisms

There were 28 Type IV microseisms recorded by the TA network in 2009. Type IV microseisms were defined as microseisms with period range of the double frequency microseism band being less than 4 sec and the peak power being equal to or smaller than -120 dB. Similar to Type III, the majority of these microseisms were likely created by multiple source locations, i.e., from different oceans. For instance, the microseism of February 28–March 7 (Table 2.4) had two dominant sources. A microseism from the North Atlantic Ocean dominated the northeast of the TA network. Meanwhile another microseism from the Pacific dominated the western portion of the network. This latter microseism was quite broad and composed of several sources distributed from the Queen Charlotte Islands Region southward to the coast of Baja California.

Another interesting example of Type IV microseism occurred on August 22–25, 2009. This seismic energy was generated by one source in the North Atlantic Ocean and another source in the central Pacific Ocean (off the coast of Southern Mexico). During

this time period, Hurricane Bill was close to the east coast in the North Atlantic Ocean. This major hurricane may have contributed to the microseism as it was travelling towards the North Atlantic Ocean. There were also single-source Type IV microseisms as well. One interesting example was the recording of September 6–9. Some ocean wave-wave interactions in the northern part of Hudson Bay generated this seismic energy having dominant period of 4.2 sec. Another single source Type IV example, which occurred on October 21 for 9 hours, was from the Gulf of Mexico. Furthermore, there were other single-source examples from the North Atlantic Ocean and the Northeast Pacific Ocean (Table 2.4).

The array-averaged peak seismic power for Type IV microseisms was between -107.6 and -119.5 dB. The corresponding average peak seismic periods fluctuated from 4.0 to 7.7 sec. The most important observation from those periods was that the North Atlantic Ocean, more specifically the region from north of Baffin Bay to the east of Newfoundland, was responsible for the short period seismic energy (4 to 6 sec). Occasionally this region generated seismic energy around 7 and 8 sec. On the other hand, most of the longer-period seismic energy (6 to 9 sec) was generated in two regions of the Pacific Ocean. One stretched from north of Gulf of Alaska to the northwestern coast of United States, while the other region stretched from off the coast of Southern California to Southern Mexico.

2.4.5 5-sec and 8-sec Eigen Power Curves

I analyzed how the array averaged seismic power in the double-frequency microseism band varied as a function of time. For this, I picked the 5-sec and 8-sec

periods. Figure 2.14 shows the array-averaged eigen power curves for these two periods. I smoothed the curves by removing earthquakes and some of the artifacts related to TA calibration. Since earthquakes appeared as spikes, I first documented when these spikes occurred throughout the whole year and then used linear interpolation to remove them. These array-averaged curves represent variations in the double-frequency microseism band without the effects of earthquakes. The 8-sec power curve was more affected by earthquakes than the 5-sec power curve.

The 5-sec eigen power curve was one of the most interesting elements of the double-frequency microseism band (top panel in Figure 2.14). One reason was that a seasonal trend could be observed. For the first 5 months of 2009, there was a decrease in power, then from June-first half of August the trend was almost constant around -130 dB with small fluctuations. Starting in late August, the general trend was an increase. The timing of the lowest and highest value also agreed with these trends. The lowest power was observed on June 5 with -136.5 dB while the highest power was observed on December 30 with -106.5 dB. As explained previously, the trend can be explained by the stormy seasons of a year: winter is the stormiest season.

Another striking observation from the 5-sec power curve was the change in dynamic range. From the beginning of the year to the middle of August, variability was small. However, from mid August to the end of the year, there was a noticeable increase in the dynamic range. There are two reasonable explanations for this. The first is the change in the locations of stations. As 2009 progressed, the stations from the west edge of the network were being redeployed to the east edge of the network (Figure 2.1). Hence, the geology (geologic units under stations, site effects) could have influenced the

recording of the 5-sec microseismic power and resulted in more variation in dynamic range. Another factor was that beginning in August, there were powerful storms generating microseisms in the Atlantic Ocean. It could be that these microseisms were more powerful than those in the Pacific Ocean and those that occurred earlier in the Atlantic Ocean.

The 8-sec eigen power curve had a similar general trend as the 5-sec eigen power curve. In the first half of 2009 there was a decrease in power, while the following second half of the year saw an increase. The lowest power was observed on July 13 with -145.3 dB while the largest value was observed on December 3 with -107.6 dB. Because of the larger dynamic range in power throughout 2009, this decreasing and increasing trend was not as noticeable as for the 5-sec curve. The reason for having larger dynamic range for the 8-sec power curve might be the remarkably small background seismic noise level at the 8-sec band.

One important observation was that the majority of Type I microseisms were of coastal origin (because of their single-frequency component) and the 8-sec period was in this group's period range. Since these Type I microseisms were closer to the TA network and the distance between source and stations was smaller, they could have been less attenuated. On the other hand, there were deep microseisms with no single-frequency component. In these cases, the distance between source and receivers was larger, and the short receiver-source distance would not be a good explanation. Considering the large dynamic range for the 8-sec power curve and larger distances between the source and receivers (in some cases), I hypothesize the 8-sec seismic energy would be less attenuated compared to the shorter periods in the double-frequency microseism band.

In order to identify the effects of attenuation on the seismic energy generated by microseisms, synthetic seismograms have to be computed. This would be done by first determining the precise location of the source, e.g., using azimuthal back-projection. The polarization vectors could be elongated along great circle arcs and the intersection of those elongated vectors would give the source location for a given time. Then, this discovered source location could be used to compute synthetics with the help of different Q (anelastic attenuation factor) values for each station. The best match between the observed waveforms and the synthetic seismograms would reveal how much the seismic signal was attenuated as a result of geometrical spreading and scattering.

2.4.6 5-sec and 8-sec Degree of Polarization Curves

Figure 2.15 shows array-averaged degree of polarization curves for the 5-sec and 8-sec periods. A quick comparison of two curves shows that the 5-sec curve (Figure 2.15 top panel) was less affected by earthquakes because it had a fewer number of transient spikes. Also, similar to the 5-sec and 8-sec eigen power curves, the 5-sec degree of polarization curve had smaller dynamic range than the 8-sec curve (Figure 2.15 bottom panel). Additionally, the 5-sec curve had quite low values for the first 4 months. Only a few times did the values exceed 0.2.

One of the most interesting time periods was the month of August. Close to the end of August, the degree of polarization values went over 0.3, which happened for two reasons. First, this time period coincided with two major storms occurring in the north Atlantic (Hurricane Bill) and the central Pacific Oceans (Hurricane Jimena). Second, the IRIS DMC was performing station calibration for the majority of stations in the TA

network. Unfortunately, the calibrations were done for a long time period (more than an hour with irregular timing) and in an interesting manner. The calibration started in the middle of the TA network and it was done at every other station as time progressed. Thus, the calibration looked like a propagating seismic wave. From the spatial polarization and eigen power animations for the 5-sec period, I found that the calibrations played a major role in the values going over 0.3.

After August, there were several other strong microseisms with noteworthy degree of polarization. Although the 5-sec curve had a slightly more dynamic range starting in August, and in general being larger than 0.2 after mid August, the polarization vectors of individual stations for the 5-sec period showed large azimuthal variations (Figure 2.15, top panel). In other words, the vectors were not aligned in one specific direction even when the degree of polarization values were high. Their azimuthal span was quite large. Thus I had difficulties in identifying dominant directions for the 5-sec period throughout the whole year.

Although the 8-sec degree of polarization curve was dominated by earthquake energy (Figure 2.15, bottom panel), the microseisms were quite clear. In fact, some microseisms had degree of polarization values either close to or even larger than the values of some earthquakes. A few nice examples were from the end of October and the whole month of December. These microseisms had degree of polarization values slightly larger than 0.4. Compared to some earthquakes in March, May, and November, these microseisms were more polarized. In general, because the 8-sec curve had larger dynamic range, the polarization vectors of individual stations were aligned in dominant directions throughout the entire year. By following these dominant directions, it was easy to

pinpoint the origin of the 8-sec seismic energy.

2.5 Discussion

I found that the Type I microseisms originated mostly from the Pacific Ocean (from the Gulf of Alaska to the southern coast of Mexico), whereas Type II microseisms were generated in the Gulf of Mexico and North Atlantic Ocean. Both types were caused by single sources (either localized or broad) from the North Atlantic and the Pacific Oceans. On the other hand, Type III and Type IV microseisms were mostly created by the combination of several sources from either the same ocean or different oceans. The dominant Type III and Type IV source regions were in the northeast and central Pacific Ocean, and the North Atlantic Ocean. Additionally, microseisms from the Gulf of Mexico and Hudson Bay were also observed in the Type IV group.

In terms of periods, I found that most often the seismic energy with periods of 4, 5, and 6 sec was generated in the North Atlantic Ocean. The 8-sec period was observed from the Pacific Ocean when Type I microseisms were present (Northeast and Central Pacific Ocean). However, the Newfoundland and Labrador region generated occasional 8-sec seismic energy as well.

In terms of duration, Type III and Type IV microseisms had the longest durations. For instance a Type III microseism in the first half of December had duration of more than 280 hours. Analyzing the polarization directions and eigen amplitudes, I found that two microseismic sources from the Newfoundland region and the Queen Charlotte Islands region contributed to this long microseism. Similar to the durations, I found that the strongest microseisms were of Type III. The microseism on December 28–31 had

array-averaged seismic power of -101.2 dB, making it the strongest microseism observed in 2009. Two regions, one from southern Mexico and another near Newfoundland and Labrador, were the dominant source regions while this event was recorded by the TA network.

Because the march of the TA stations to the east continued in 2009, different geologic units affected the recordings of microseisms throughout 2009. For instance if two microseismic sources were present in the both oceans (Atlantic and Pacific), or even two microseisms in the same ocean, the TA stations responded differently to these sources. This was observed strongly with the spatial polarization animations. In some cases, the northern stations were indicating ocean wave-wave interaction either from the Atlantic coast or Northeast Pacific coast, while the southern stations were showing microseisms originating off the coast of California or the Pacific coast of the Southern Mexico. Additionally, TA stations deployed on the two sedimentary basins in the Great Plains and Rio Grande Rift region showed clear site effects. When a weaker microseism was propagating, the stations in these regions had their polarization directions changing every hour and indicated directions not associated with any significant seismic signal (i.e., earthquakes, microseisms, cultural noise, etc.). This caused some difficulties when I tried to determine the dominant polarization direction or origin of the seismic energy. This was observed with the spatial polarization animations for 5 sec period and the spatial eigen power animations for the 4, 5 sec, and even in some cases for 6 and 8 sec periods.

Table 2.1 Type I Microseisms

Date	Duration (hours)	Pol Direction	Location	Ave. Peak Seismic Power (dB)	Ave. Peak Period (sec)	Period Range (sec)	Single-freq comp.?
January 10–11	17	NW	Gulf of Alaska	-120.0	7.7	7.1–8.5	Yes
February 15–16	20	NW	Gulf of Alaska	-120.2	8.5	7.7–9.5	Yes
March 9–10	24	NW	Gulf of Alaska	-122.1	8.3	7.9–9.8	Yes
March 10–12	40	SW	Southwest of Baja California	-119.2	7.4	6.1–8.5	Not clear
March 27–29	44	NW	Gulf of Alaska	-112.7	8.3	6.2–10.1	Yes
April 3–5	54	SW	The Pacific coast of Sthrn Mexico	-122.2	7.7	7.0–8.8	Yes
April 5–8	87	NW	Gulf of Alaska	-113.3	7.7	6.2–8.7	Not clear
April 11–13	44	NW	Gulf of Alaska	-122.0	8.1	7.5–8.9	Yes
April 12–13	25	SW-S	Several sources Baja California, and the Pacific coast of Sthrn Mexico	-121.8	8.1	7.1–9.0	Yes
April 19–21	65	SW	Off the coast of Sthrn California and Baja, California	-121.8	6.9	6.4–7.5	Yes
April 22–26	99	S	The Pacific coast of Sthrn Mexico	-121.3	8.9	7.2–10.0	Yes
May 7–10	74	SW-S	The Pacific coast of SthrnMexico	-127.4	8.5	7.8–9.0	Yes
June 4–7	75	S	The Pacific coast of Sthrn Mexico	-127.8	8.7	7.0–9.2	Yes
June 9–12	52	S	The Pacific coast of Sthrn Mexico	-129.1	7.9	7.1–9.0	Yes
June 25–28	50	SW	Off the coast of Sthrn California and Baja California	-121.9	7.9	7.1–8.9	No
July 15	16	NE	Northern Atlantic (Newfoundland and Labrador)	-128.3	6.3	5.5–6.8	Yes

Table 2.1 continued

Date	Duration (hours)	Pol Direction	Location	Ave. Peak Seismic Power (dB)	Ave. Peak Period (sec)	Period Range (sec)	Single-freq comp.?
July 21–23	44	S	The Pacific coast of Sthrn Mexico	-128.7	8.3	7.1–9.0	Not clear
July 23–27	107	S	The Pacific coast of Sthrn Mexico	-118.8	8.7	6.1–10.1	Yes
July 28–30	53	S	The Pacific coast of Sthrn Mexico	-129.5	8.1	7.0–9.2	Yes
August 20–22	54	S	The Pacific coast of Sthrn Mexico	-123.2	8.1	8.1–10.1	Yes
August 22–24	32	E-NE	North Atlantic (Hurricane Bill)	-114.8	8.1	7.1–9.7	Yes
September 1–3	30	SW	Off the coast of Baja California	-113.7	7.0	6.0–9.2	No
September 8–10	44	SW	Off the coast of Baja California	-123.7	6.9	6.2–7.8	No
September 13–14	39	SW	Off the coast of Baja California	-125.6	7.9	7.0–9.0	Not clear
September 21–22	16	NW	Gulf of Alaska	-120.4	7.4	6.4–8.0	Yes
October 3–5	48	S	The Pacific coast of Sthrn Mexico	-124.9	8.1	7.1–9.8	Yes
October 20–21	21	SW	Off the coast of Sthrn California	-115.9	6.9	6.0–7.9	No
October 21–24	78	NW	Gulf of Alaska	-110.7	7.7	6.1–9.3	Yes
November 25–27	43	NW	The Queen Charlotte Islands Region	-116.8	8.3	6.2–9.1	Yes
December 5–6	18	SW	Several sources along the coast of Sthrn California, and Baja California	-122.9	9.3	8.3–10	Yes

Table 2.2 Type II Microseisms

Date	Duration (hours)	Pol Direction	Location	Ave. Peak Seismic Power (dB)	Ave. Peak Period (sec)	Period Range (sec)	Single-freq comp.?
March 8	12	SE	Gulf of Mexico	-120.5	5.1	4.2–5.4	Not clear
March 9–11	29	NE	North Atlantic (Newfoundland)	-121.2	4.7	3.6–5.8	Not clear
March 28	22	SE	Gulf of Mexico	-122.0	4.3	3.1–4.9	Yes
April 11–13	35	NE	North Atlantic (Newfoundland)	-117.1	4.4	3.2–5.2	Yes
June 6–9	62	SE	Gulf of Mexico	-123.2	4.2	3.0–5.2	Not clear
July 25–26	30	SE	North Atlantic (off the coast of Eastern Florida)	-125.0	3.9	3.1–4.7	No
October 9–10	22	SE	Gulf of Mexico	-116.5	3.8	2.9–4.1	Not clear
October 23–24	32	SE & NE	Newfoundland Region & Gulf of Mexico	-113.8	4.8	3.1–5.5	Not clear
October 30	20	SE	Gulf of Mexico	-117.3	4.2	3.0–4.9	Yes
December 14–15	31	NE	Atlantic Ocean (The Northeast coast of US)	-117.6	4.2	2.9–5.0	Not clear
December 24–25	32	SE	Gulf of Mexico	-114.4	4.3	2.8–5.1	Yes

Table 2.3 Type III Microseisms

Date	Duration (hours)	Pol Direction	Location	Ave. Peak Seismic Power (dB)	Ave. Peak Period (sec)	Period Range (sec)	Single-freq comp.?
January 1–7	156	NW, NE, S	Gulf of Alaska, North Atlantic & Sthrn Mexico	-108.2	5.9	3.4–9.0	Yes
January 14–19	123	NE	North Atlantic	-108.3	6.9	3.5–9.5	Yes
September 10–12	47	NW, NE	Gulf of Alaska & North Atlantic	-109.1	5.5	3.2–8.5	Yes
October 11–14	74	NE	Newfoundland	-113.7	6.3	3.7–8.6	Yes
October 14–20	150	NE, S	North Atlantic, Sthrn Mexico	-102.6	6.3	3.1–8.6	Yes
October 26–30	83	NE, SE	Newfoundland & off the coast of Sthrn California	-105.7	5.4	2.8–9.1	Yes
November 5–10	131	NW, NE	Gulf of Alaska & Newfoundland	-106.4	8.7	3.2–10.1	Yes
November 27–December 2	130	NW, NE	North Atlantic & Northeast Pacific	-108.2	7.4	3.2–10.4	Yes
December 2–14	283	NW, NE	Gulf of Alaska & Newfoundland	-105.1	6.5	3.0–9.0	Yes
December 16–24	203	NW, NE	Gulf of Alaska & Newfoundland	-106.6	5.6	2.9–8.1	Yes
December 28–31	80	NE, S	Newfoundland & Sthrn Mexico	-101.2	6.2	2.8–9.2	Yes

Table 2.4 Type IV Microseisms

Date	Duration (hours)	Pol Direction	Location	Ave. Peak Seismic Power (dB)	Ave. Peak Period (sec)	Period Range (sec)	Single-freq comp.?
Jan 7–14	153	NE	North Atlantic	-116.1	5.2	3.6–7.0	Yes
Jan 19–23	118	NE	North Atlantic	-112.9	5.4	3.6–7.0	Yes
Jan 23–28	119	NE, NW	North Atlantic (dominant)	-111.9	7.7	4.1–8.7	Yes
Jan 29–Feb 1	69	NW	Gulf of Alaska	-115.3	5.8	3.7–7.5	Yes
Feb 1–3	55	NE, NW	North Atlantic (dominant)	-112.9	5.9	4.0–7.5	Yes
Feb 3–9	138	NW	Northeast Pacific	-112.8	5.5	3.4–7.5	Yes
Feb 9–12	66	Not clear	Not clear	-116.4	5.6	3.7–8.2	Yes
Feb 13–17	89	NE	North Atlantic	-114.5	5.9	3.8–7.6	Not Clear
Feb 17–22	102	NW, NE	N. Atlantic & NE Pacific	-110.5	6.2	3.7–8.3	Yes
Feb 23–27	49	NE, NW	N. Atlantic & NE Pacific	-116.5	5.2	3.7–7.1	Yes
Feb 28–March 7	167	NW, NE	Gulf of Alaska & N. Atlantic	-115.4	4.7	3.4–8.5	Yes
March 7–8	22	NW	Gulf of Alaska	-114.8	7.7	6.3–8.8	Yes
March 12–14	40	S, NW	Pacific coast of S. Mexico & NE Pacific	-118.8	4.9	3.9–7.1	Not clear
March 14–19	123	W	Off the coast of Washington State	-116.9	7.1	5.4–8.1	Yes
March 29–April 2	96	NE, SW	Sthrn California & North Atlantic	-113.6	5.2	3.7–7.1	Yes
April 14–18	100	NE	North Atlantic	-116.6	6.6	3.9–7.8	Not clear
May 11–13	46	NE	Newfoundland & Labrador	-112.6	5.9	4.3–7.1	Not clear
Aug 22–25	80	NE, S	N. Atlantic & Pacific coast of sthrn Mexico	-117.1	5.2	2.9–7.0	Not clear
Sep 6–9	62	NE	Hudson Bay	-118.1	4.2	3.1–5.8	Not clear
Sep 14–21	144	NE, NW,SW	N. Atlantic & NE and central Pacific	-107.6	5.6	3.3–6.7	Yes
Sep 25–27	45	NE, NW	Hudson Bay & Gulf of Alaska	-117.3	5.1	3.4–7.5	Yes

Table 2.4 continued

Date	Duration (hours)	Pol Direction	Location	Ave. Peak Seismic Power (dB)	Ave. Peak Period (sec)	Period Range (sec)	Single-freq comp.?
Sep 30–Oct 4	114	NE	North Atlantic	-119.5	4.0	3.4–6.1	Not clear
Oct 8–11	80	NE	Newfoundland	-110.9	6.0	3.7–7.6	Yes
Oct 21	9	SE	Gulf of Mexico	-116.5	4.8	3.5–5.6	Not clear
Oct 31–Nov 3	70	NE	North Atlantic	-109.6	5.6	3.0–7.0	Yes
Nov 11–16	130	S, NE, NW	N. Atlantic, NE Pacific, Cen. Pacific	-115.2	7.6	2.9–8.7	Yes
Nov 16–21	128	NW	Northeast Pacific	-113.2	5.5	3.4–7.8	Yes
Nov 21–24	62	NE, NW	NE Pacific & Hudson Bay	-117.6	5.9	3.4–6.8	Yes

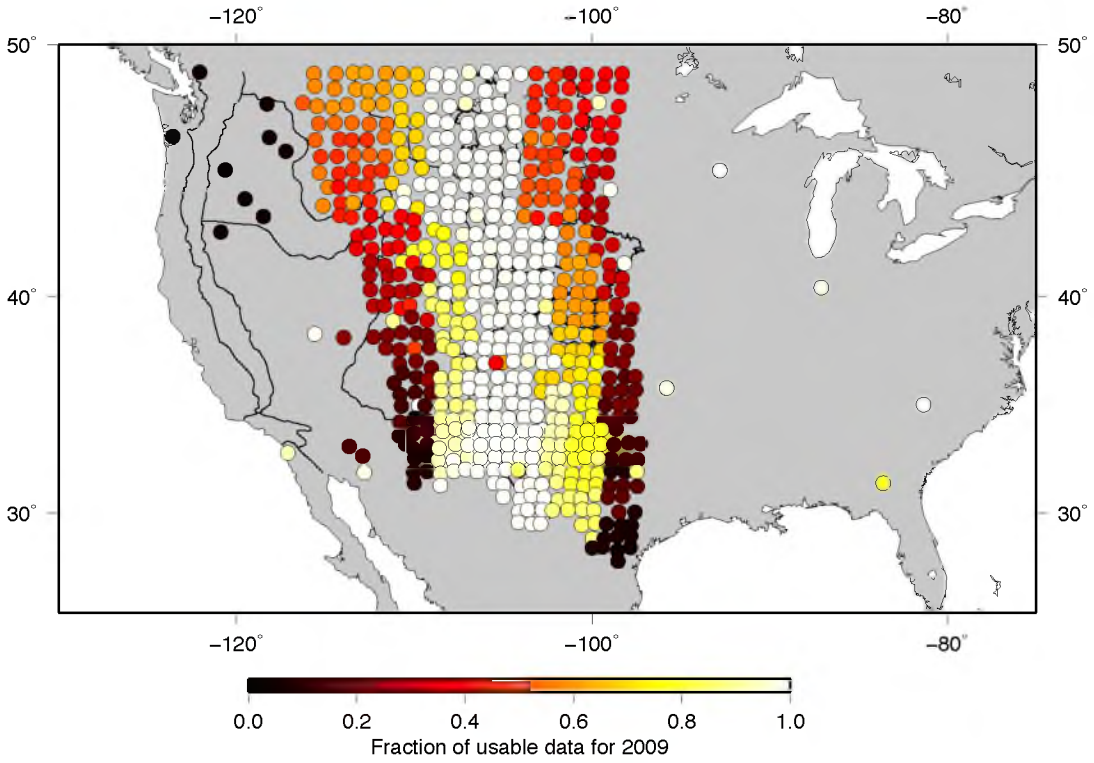

Figure 2.1 Data availability and location of the TA stations during 2009. Light colors indicate higher availability while darker colors indicate less available data for 2009. The black lines on the map show major physiographic provinces of the Western and Central United States.

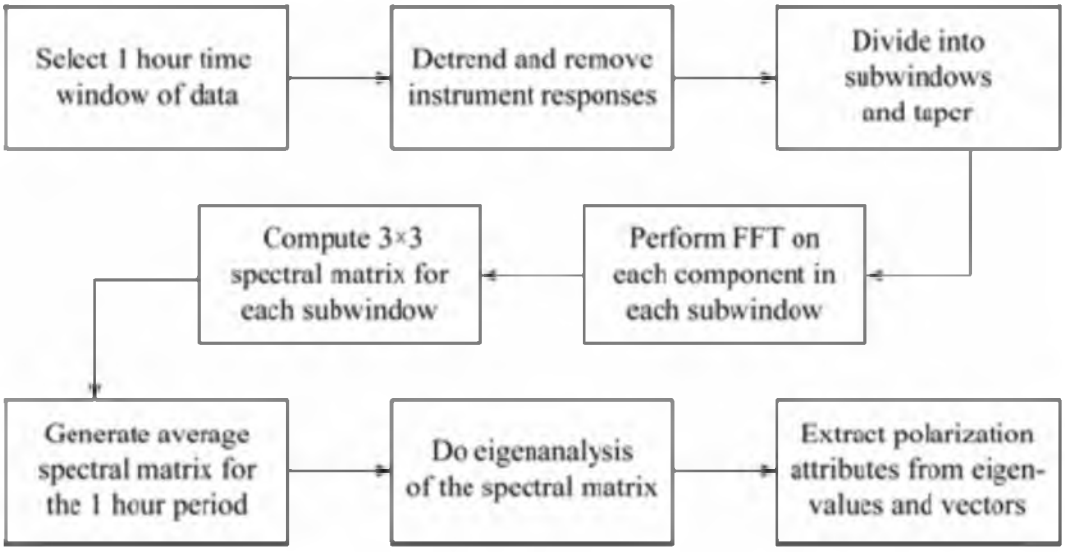

Figure 2.2 Flowchart showing how the data were processed (adapted from Koper and Hawley, 2010)

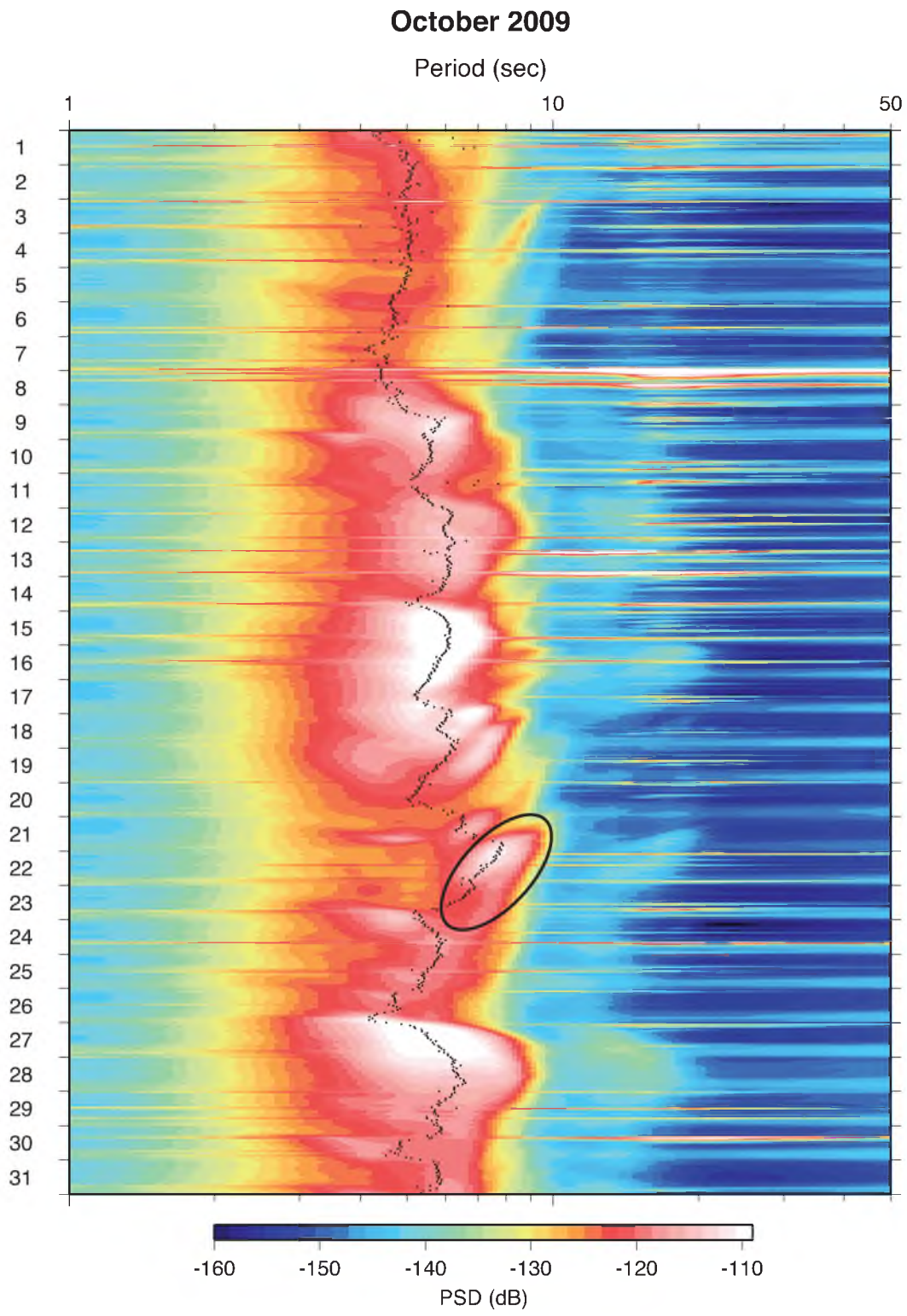

Figure 2.3 Array averaged spectrogram for the month of October 2009. The black ellipse outlines a Type I microseism recorded during October 21–24 by the TA stations. The black dots in the double-frequency microseism band (3–9 sec) indicate the maximum power for each hour.

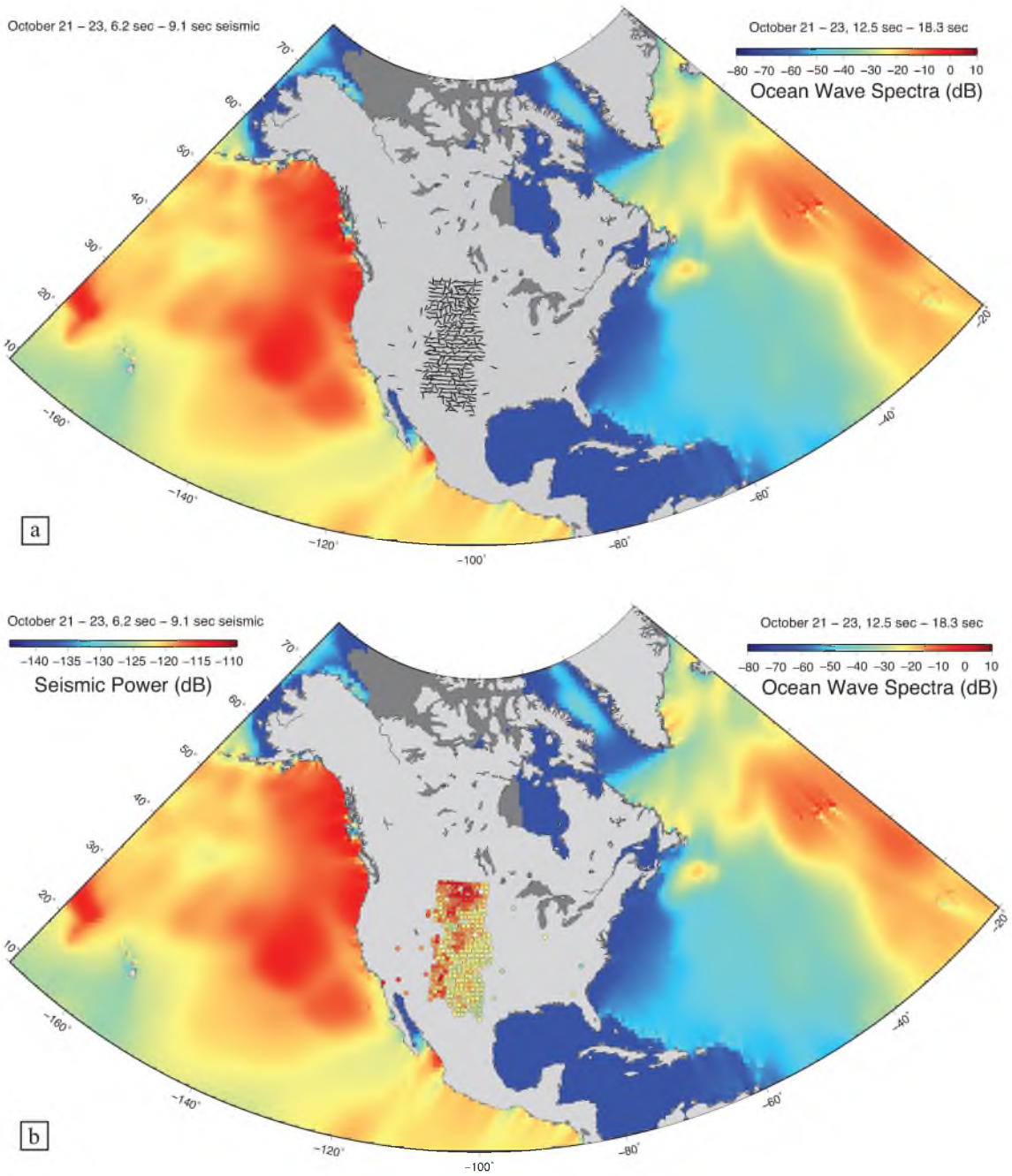

Figure 2.4 Seismic vs. Ocean wave spectra for Type I microseism from October 21–23. a) Comparison of the time and frequency averaged polarization vectors and b) the seismic amplitudes (bottom) of individual stations with the ocean wave spectra for the microseism recorded between October 21–23

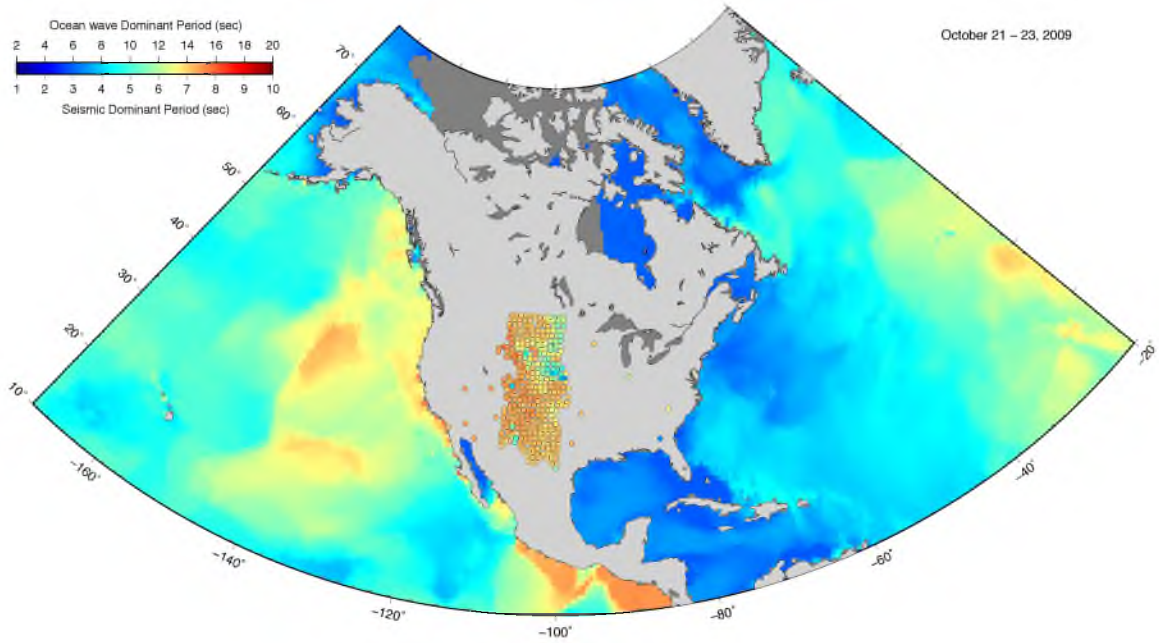

Figure 2.5 A comparison of averaged peak seismic periods of individual stations with the averaged peak ocean wave periods for the microseism of October 21–23, 2009.

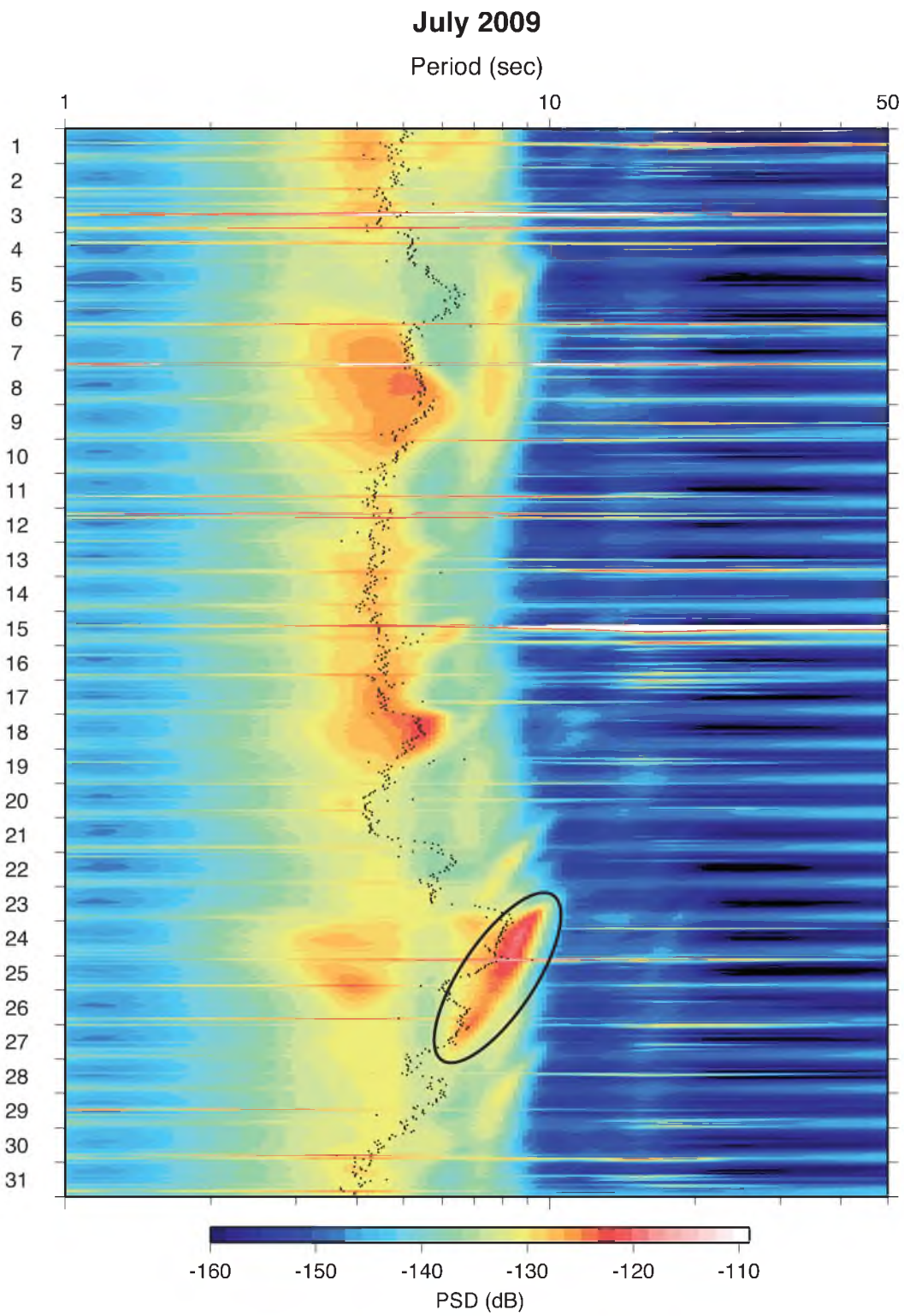

Figure 2.6 Array averaged spectrogram for the month of July from 2009. The black ellipse outlines a microseism recorded during July 23–27 by the TA stations. The black dots in the double-frequency microseism band (3–9 sec) indicate the maximum power for each hour.

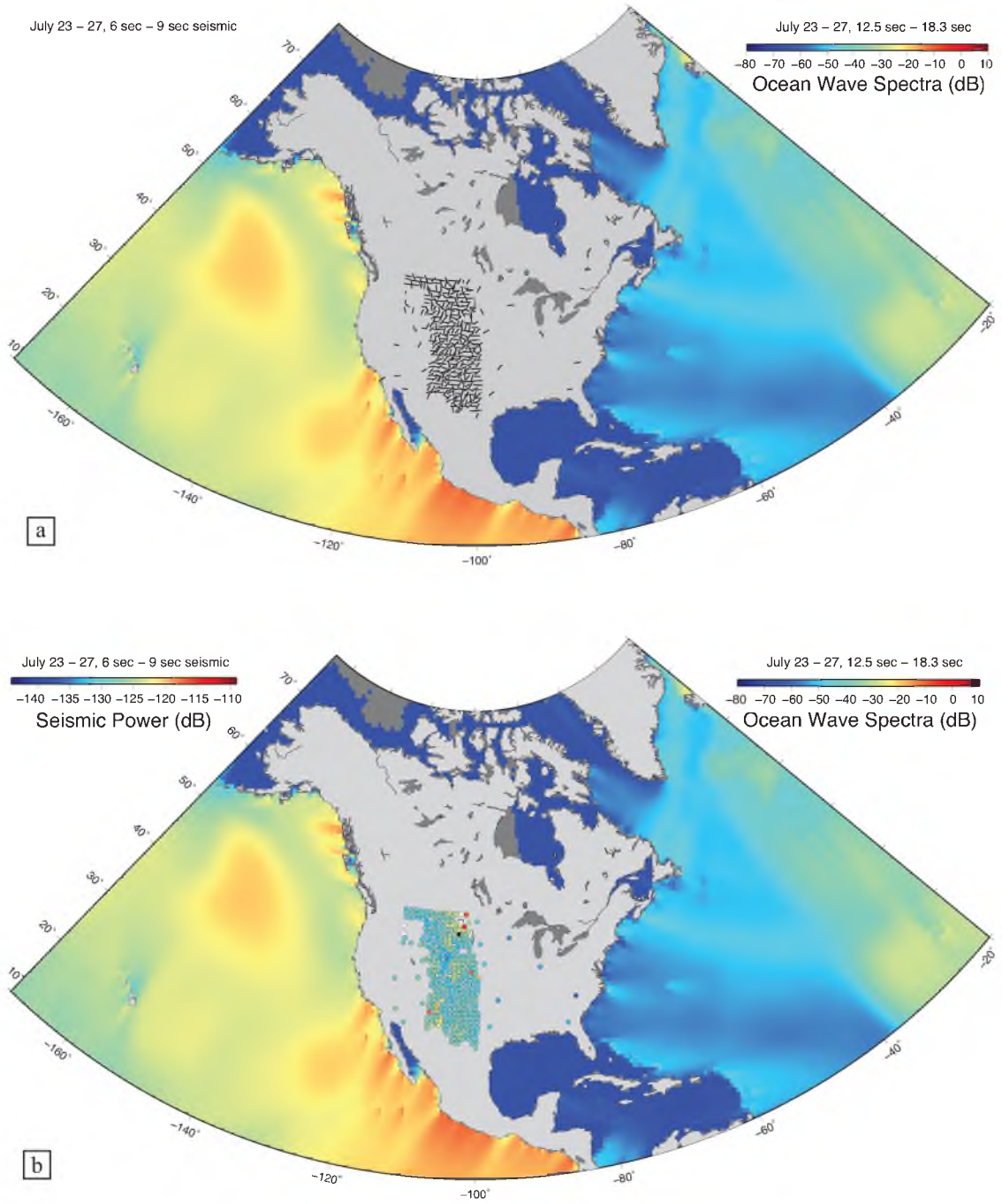

Figure 2.7 Seismic vs. Ocean wave spectra for Type I microseism from July 23–27, 2009. a) Comparison of the time and frequency averaged polarization vectors and b) the seismic amplitudes (bottom) of individual stations with the ocean wave spectra for the microseism recorded between July 23–27.

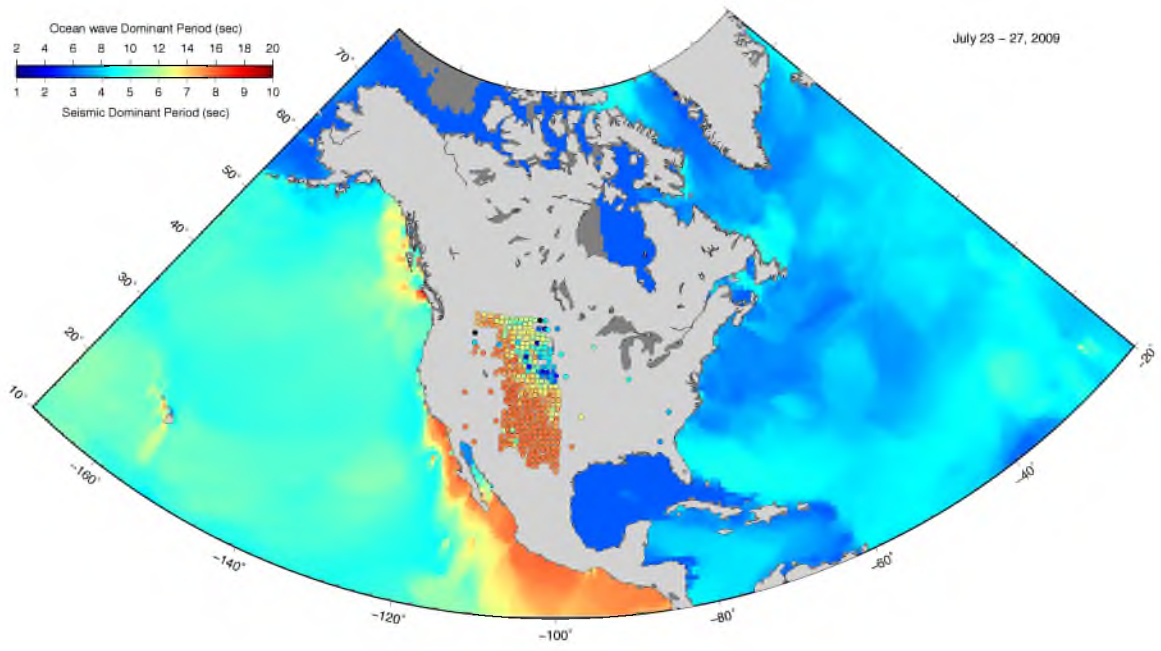

Figure 2.8 Comparison of average peak seismic periods of individual stations with the average peak ocean wave periods for the microseism of July 23–27, 2009.

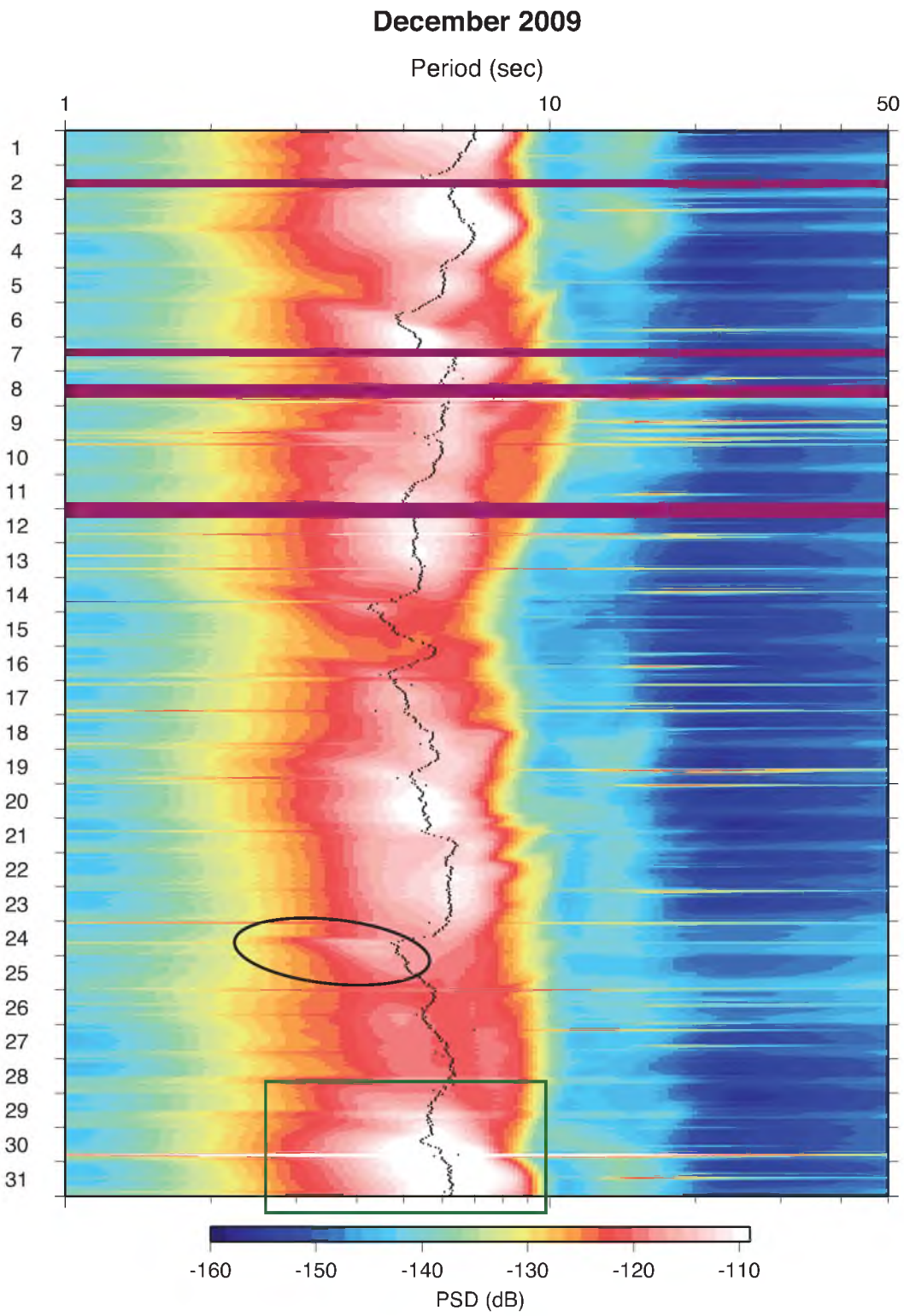

Figure 2.9 Array averaged spectrogram for the month of December from 2009. The black ellipse outlines a Type II microseism recorded during December 24–25 by the TA stations. The green rectangle outlines the Type III microseism recorded during December 28–31. The dark purple lines indicate missing hours. The black dots in the double-frequency microseism band (3–10 sec) indicate the maximum power for each hour.

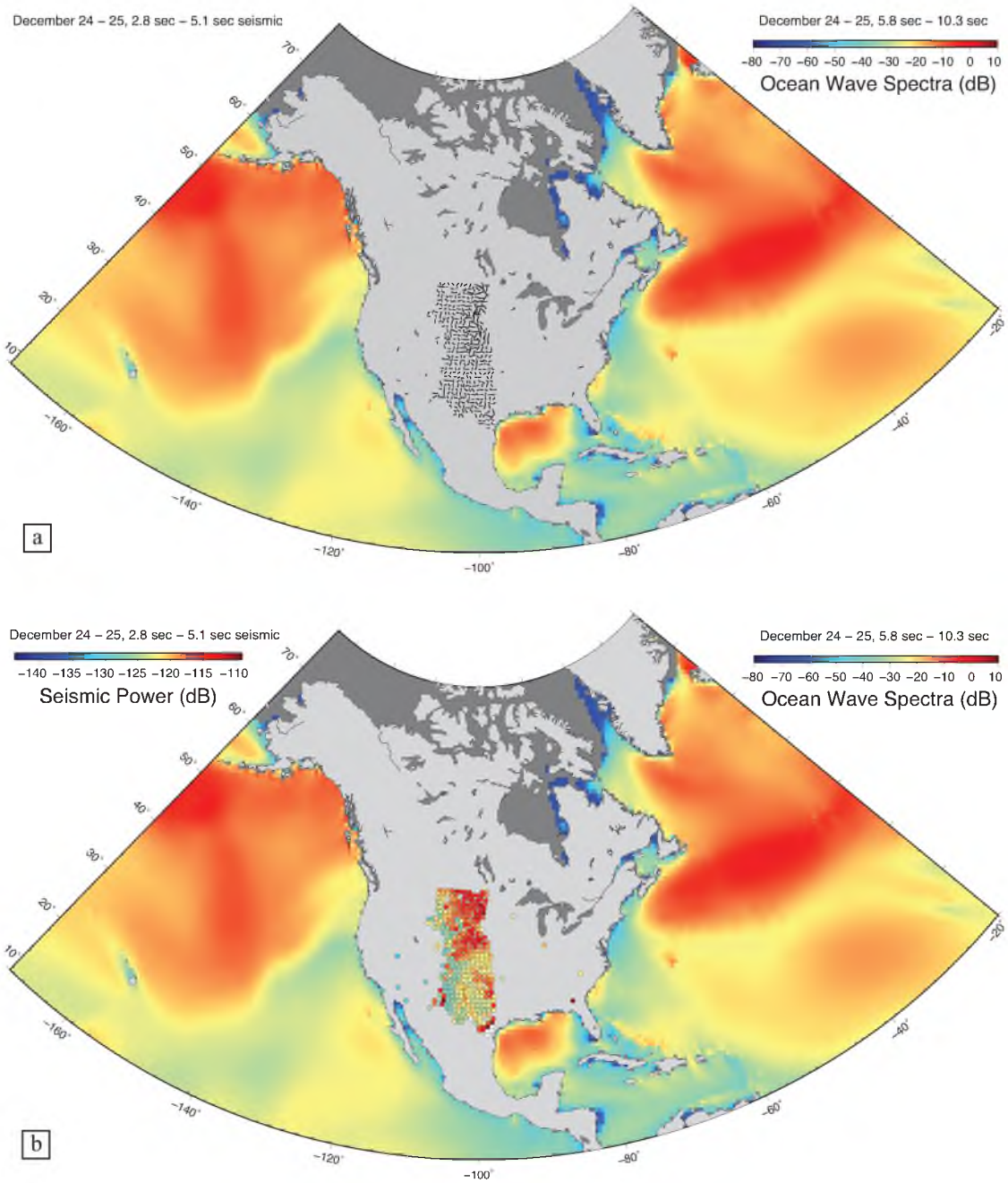

Figure 2.10 Seismic vs. Ocean wave spectra for Type II microseism between December 24–25. a) Comparison of the time and frequency averaged polarization vectors and b) the seismic amplitudes (bottom) of individual stations with the ocean wave spectra for the microseism recorded between December 24–25.

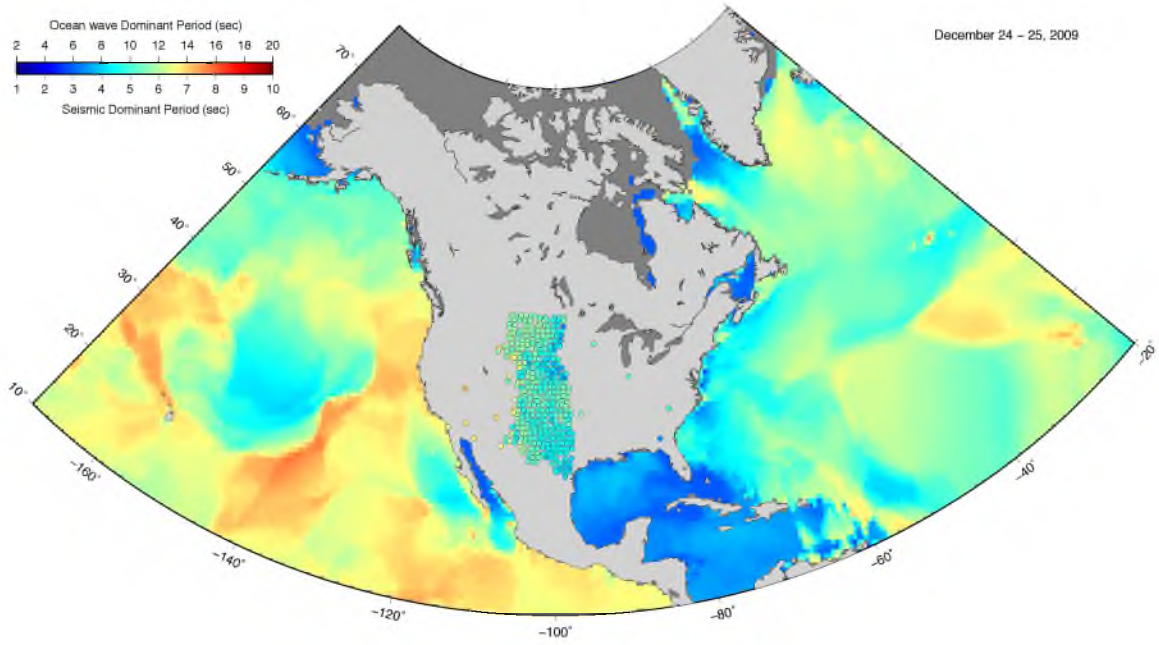

Figure 2.11. Comparison of average peak seismic periods of individual stations with the average peak ocean wave periods for the microseism of December 24–25, 2009.

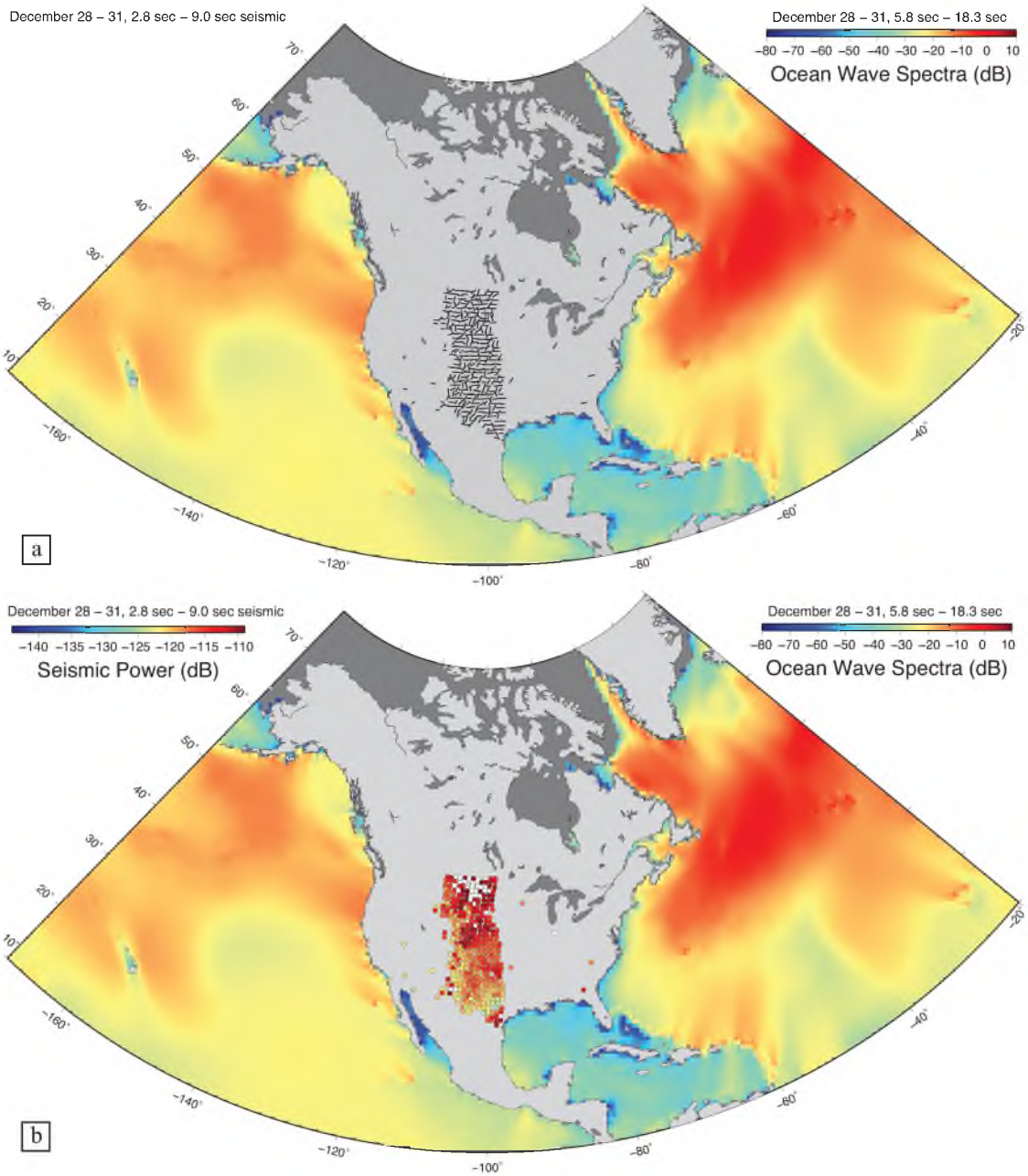

Figure 2.12 Seismic vs. Ocean wave spectra for Type III microseism between December 28–31. a) Comparison of the time and frequency averaged polarization vectors and b) the seismic amplitudes of individual stations with the ocean wave spectra for the microseism recorded between December 28–31.

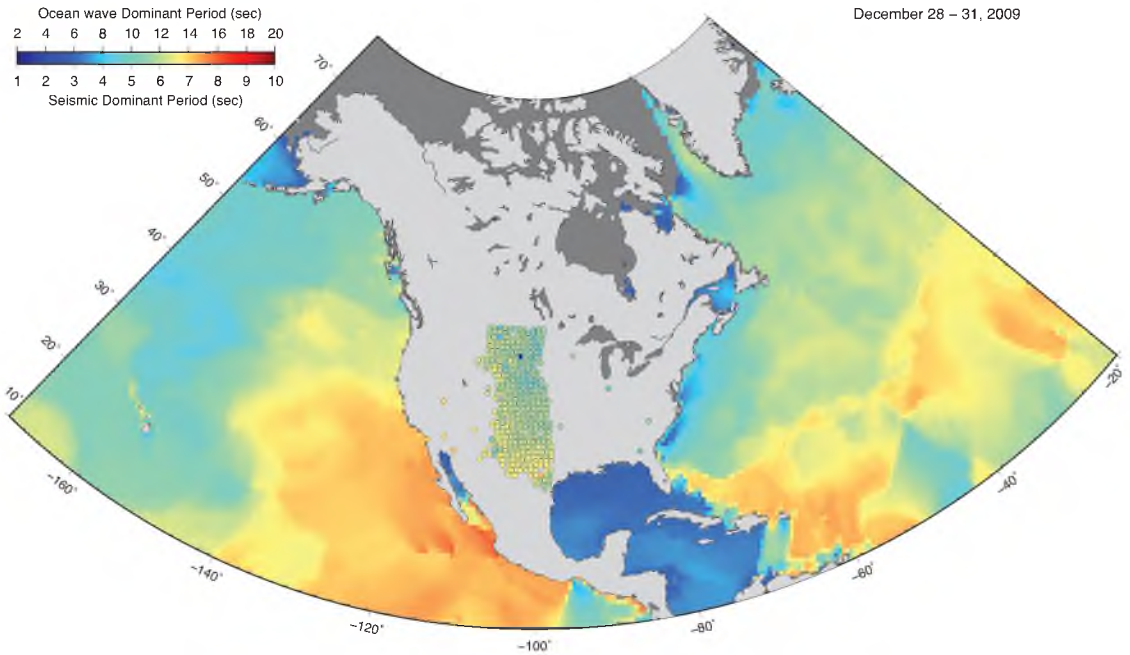

Figure 2.13 Comparison of average peak seismic periods of individual stations with the average peak ocean wave periods for the microseism of December 28–31 , 2009.

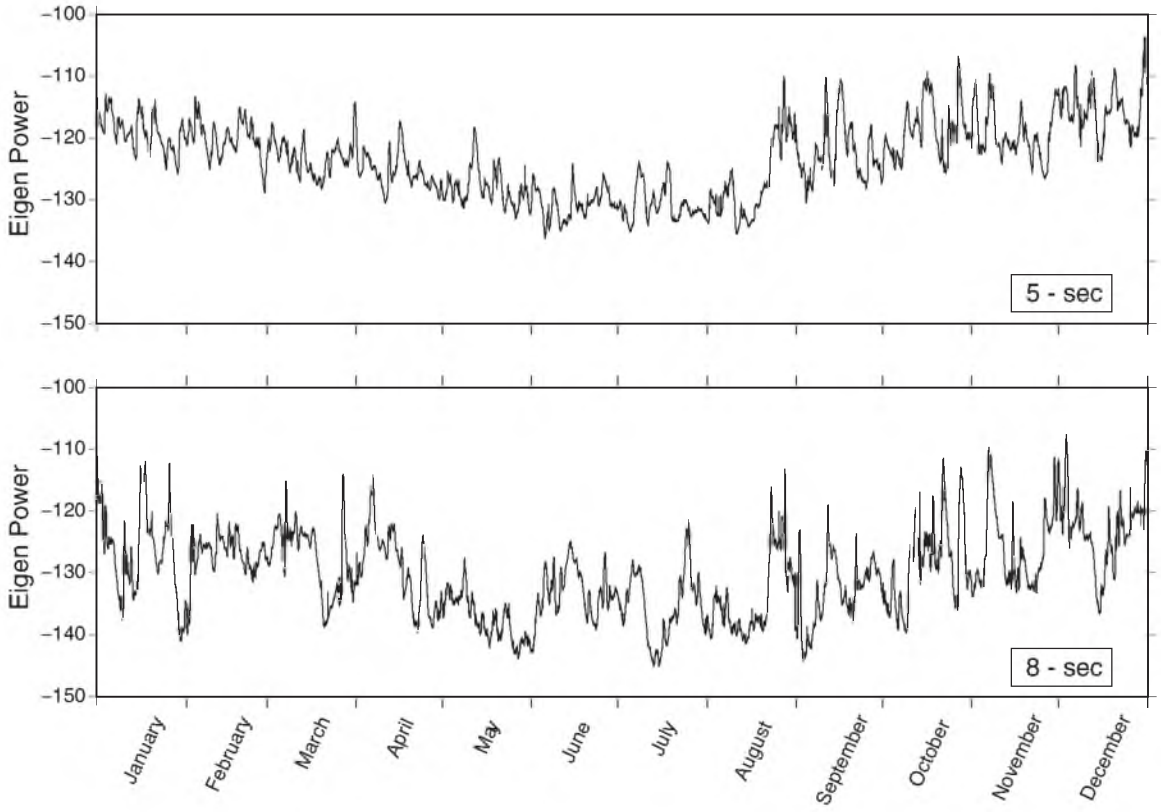

Figure 2.14 Array averaged and smoothed eigen power curves for the 5-sec (top) and the 8-sec (bottom) periods for 2009.

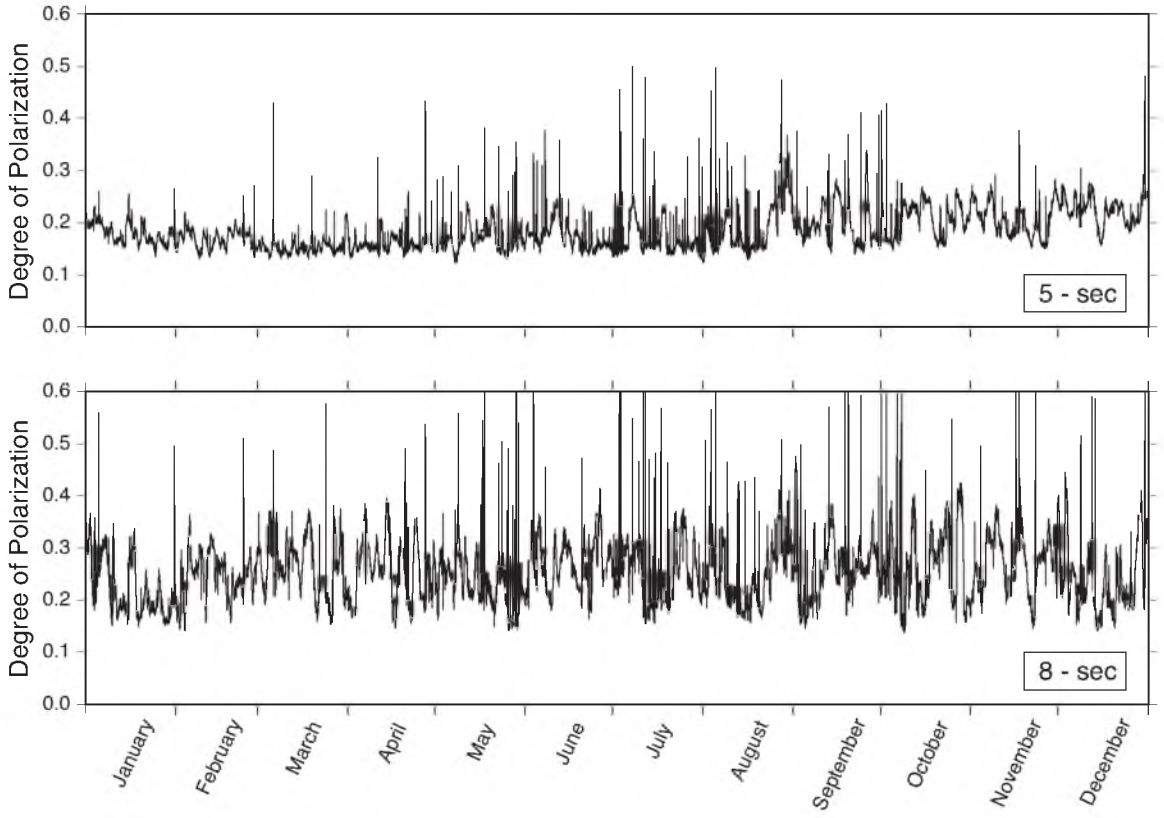

Figure 2.15. Array averaged degree of polarization curves for 5-sec (top) and 8-sec (bottom) periods for 2009.

CHAPTER 3

MICROSEISMS FROM SUPERSTORM SANDY[1]

3.1 Abstract

We analyzed and visualized the microseisms generated by Superstorm Sandy as recorded by the Earthscope Transportable Array (TA) during late October through early November of 2012. We applied continuous, frequency-dependent polarization analysis to the data and were able to track the course of Sandy as it approached the Florida coastline and, later, the northeastern coast of the U.S. The energy level of Sandy was roughly comparable to the background microseism level generated by wave-wave interactions in the North Atlantic and North Pacific oceans. The maximum microseismic power and degree of polarization were observed across the TA when Sandy sharply changed its direction to the west-northwest (specifically, towards Long Island, New York) on October 29. The westward turn also briefly changed the dominant microseism period from 5 sec to 8 sec. We identified three other microseismic source regions during the 18-day observation period. In particular, peak-splitting in the double frequency band and the orientation of the 5-sec and 8-sec polarization vectors revealed two contemporaneous microseism microseism sources, one in the North Atlantic and one in the Northeast

[1] Reprinted from Earth and Planetary Sciences, 402, Sufri, O., Koper, K. D., Burlacu, R., and B. de Foy, Microseisms from superstorm Sandy, 324–336, Copyright (2014) with permission from Elsevier.

Pacific, for the dates of November 3–4. Predictions of microseismic excitation based on ocean wave models showed consistency with the observed microseismic energy generated by Sandy and other storms.

3.2 Introduction

It is well known that hurricanes, typhoons, and other oceanic storms create microseisms with periods of ~1–20 sec at land-based seismometers, even those located thousands of kilometers inland from coastlines. Owing to relatively recent deployments of mid- and large-aperture arrays of broadband seismometers, it is now possible to study the complete wavefield of these signals, leading to improved location of microseismic sources and a deeper understanding of the underlying source mechanism.

Recent examples of these types of studies include detections of body and surface waves in southern California from 2005 Hurricane Katrina in the Gulf of Mexico (Gerstoft et al., 2006); location of microseismic sources in the Mediterranean Sea and northern Atlantic Ocean in the boreal winter of 2005–2006 using several variable-aperture arrays in western Europe (Chevrot et al., 2007); detection and location of teleseismic P waves throughout the world's oceans recorded by arrays in Yellowstone, Kyrgyzstan, and Turkey in 2000–2001 (Landes et al., 2010); tracking of western Pacific typhoons in 2006 using data recorded across Japan and Taiwan (Chi et al., 2010); analysis of Hurricane Irene and other storms in 2011–2012 using Transportable Array (TA) stations in the central U.S. (Traer et al., 2012); observations from a temporary array deployed in 2002 in New Zealand of differing source regions for Love and Rayleigh waves created by Southern Ocean storms (Behr et al., 2013); and validation of

microseismic P waves recorded at the Southern California Seismic Network (Obrebski et al., 2013).

While the basic theory of excitation for microseismic Rayleigh waves has been known for decades (e.g., Longuet-Higgins, 1950; Hasselmann, 1963) general uncertainties still exist in terms of source locations and mechanisms, such as the relative importance of coastal reflections versus deep water storm interactions in generating double-frequency microseisms and the details of how strong transverse energy (Love waves) can be generated by the fluid ocean interacting with the solid Earth. The recent development of sophisticated, realistic ocean-wave models and theoretical advances in fluid dynamics now allow for quantitative simulation of microseisms (Kedar et al., 2008; Ardhuin et al., 2011; Ardhuin and Herbers, 2013), and therefore a current motivation for studying microseisms is to better understand fundamental interactions between the coupled atmosphere-ocean-solid Earth system. This topic was listed fourth in a recent top 10 list of "Seismological Grand Challenges" (Lay et al., 2009) and is one that will likely become increasingly important in the future as the geophysical effects of climate change are identified and studied.

A specific theme in microseismic research that has emerged is mining historical seismic data to develop a baseline of severe storm occurrence in presatellite days when hurricanes, typhoons, and so on were likely undercounted or poorly documented (Landsea, 2007). This allows for quantitative comparisons with more recent seismic observations of storm activity to determine whether storm frequency and intensity have increased over the last 50–60 years as global temperatures have risen (Grevemeyer et al., 2000; Ebeling and Stein, 2011); more generally it complements seismic monitoring of

changes in the ocean wave climate that capitalize on the broad geographical sensitivity of microseisms (Aster et al., 2008; Koper et al., 2009; Stutzmann et al., 2009; Aster et al., 2010).

In this study, we report on microseisms created by Superstorm Sandy that were recorded by stations of the TA deployed mostly in central and eastern U.S. during the period of October 22–31, 2012. Although at its peak Sandy was classified only as Category 3 (out of 5) on the Saffir-Simpson hurricane wind scale (http://www.nhc.noaa.gov/aboutsshws.php), it was the largest Atlantic hurricane on record as measured by spatial extent and caused enormous damage along the east coast of the United States. We perform continuous, frequency-dependent polarization analysis of the TA data to determine how microseismic waves created by Sandy varied in time, space, power, coherence, and polarization and compare these to meteorological observations of Sandy and predictions of microseismic power based on ocean wave models. We also compare the seismic observations of Sandy to the background microseismic field generated over a slightly longer time period (October 18−November 4, 2012).

3.3. Data and Methodology

We downloaded all available broadband seismic data (channel codes of BHZ, BHN, and BHE) with the TA network code from the IRIS Data Management Center (DMC, www.iris.edu) for the days of October 18, 2012 through November 4, 2012 (GMT), corresponding to 432 potential hours of data for each station. For a given hour of station data to be viable, we required there to be no gaps on all three components. Overall the data return was excellent, with 403 of the 428 stations meeting this requirement for all

432 hours (Figure 3.1). We selected an hour as the fundamental unit of time in which to process the data because initial work showed that over this time period microseisms are relatively stationary and tend to overwhelm signals from transient events, such as small-to-moderate sized regional earthquakes.

The technique we used to process the data is described in detail in Koper and Hawley (2010). It is based on eigen-decomposition of 3x3 spectral covariance matrices at individual stations and follows the work of Sampson (1983) as described by Park et al. (1987). Cross-spectra are calculated only between different components of a single station and not between like components of different stations, so it is fundamentally a polarization analysis and not a conventional f-k or beamforming analysis. Advantages of the polarization approach over beamforming include (1) seismic energy does not have to be coherent between stations, (2) seismic energy does not have to propagate as a plane wave, and (3) true amplitudes are recovered because there is no beam loss. The main disadvantage is that polarization analysis tends to give more scattered estimates of backazimuth than does beamforming, especially when the signal-to-noise ratio is small (Harris 1990; Suteau-Henson, 1990; Schulte-Pelkum et al., 1994).

Our approach is similar to the analyses of Tanimoto et al. (2006) and Schimmel et al. (2011) in that it operates in the frequency domain, and polarization information, such as the degree of elliptical particle motion, is determined from phase differences among the components of a complex vector. In this respect it is different from techniques that extract polarization information from the relationship among the three eigenvalues of a purely real 3x3 covariance matrix calculated in the time domain (e.g., Jurkevics, 1988; Earle, 1999; Schulte-Pelkum et al., 2004).

Each hour-long segment of data is detrended and restored to ground acceleration by spectral division of the instrument response using a trapezoidal frequency-domain taper defined with frequency limits of 0.001–0.002 Hz and 10–20 Hz. Next, it is divided into 10 subwindows of length 819.2 sec (32,768 points) that overlap one another by 62%. Each subwindow is detrended, tapered with a 10% Hanning window, and processed with a fast Fourier transform (FFT). The spectral covariance matrix for the subwindow is computed by multiplying the FFT of each component by the complex conjugate of each component, and the overall spectral covariance matrix for the hour is computed by linear averaging of the subwindow matrices. A $\log_{10}$-based smoothing scheme is used to reduce the number of independent frequency bins from 32,768 to 301, with the lowest bin centered at 0.00123 Hz and the highest at 19.9 Hz. The diagonal elements of the spectral matrix are estimates of the power spectral density (PSD) for each component and are output and saved for each hour-long segment of data at each station.

We next perform eigen-decomposition of each matrix and save the values of the dominant eigenvalue (λ) and eigenvector, as well as the degree of polarization, β^2, which varies from 0, when the three eigenvalues are equal, to 1 when only a single non-zero eigenvalue exists (Samson, 1983). Polarization information is extracted from the complex dominant eigenvector (i.e., the eigenvector associated with the largest eigenvalue) as discussed by Park et al. (1987) to yield the following four angular quantities: Θ_H, the horizontal azimuth of the major axis, which points in the direction of the source for P-waves, and varies from -180° to 180°; Θ_V, the angle made with the vertical by the major axis of the ellipse, which corresponds to the angle of incidence for P waves, and varies from 0° to 90°; φ_{HH}, the phase difference between the horizontal components, which

varies from 0° to 180° and represents the degree of ellipticity in the horizontal plane; and φ_{VH}, the phase difference between the vertical and principal horizontal components, which varies from -90° to 90° and represents the degree of ellipticity in that plane, for instance being -90° for a pure retrograde Rayleigh wave.

3.4 Results

3.4.1 Time Evolution of Array-Averaged Microseismic Power

There is strong variability in microseism power as a function of frequency. The double-frequency, or secondary, peak is usually the largest in the microseismic band, and although it is centered at periods of 4–5 sec on average (Peterson, 1993), it can vary significantly based on the distance from the source region to the station, the near-source bathymetry, and the details of the wave-wave interactions at the ocean's surface. Likewise, the single-frequency, or primary, peak that is centered at periods near 15 sec on average (Peterson, 1993) can drift a few seconds in either direction. Furthermore, oceanic storms can excite seismic energy at periods both smaller (e.g., Koper et al., 2009) and larger (e.g., Rhie and Romanowicz, 2004) than the classic microseismic range.

We explore this issue for Sandy by calculating the array-averaged power as a function of time for each of the 301 frequency bins. This is presented as a spectrogram in Figure 3.2a. Power was calculated from the largest eigenvalue of the spectral matrix. This quantity is indicative of the dominant microseismic mode of propagation, no matter how the wavefield is polarized or from what direction it arrives at a station. It is a convenient way to reduce the number of dependent variables from 3 to 1 for visualization purposes. Figure 3.2b shows slices of the spectrogram throughout the microseismic band, at periods

of 1 sec, 5 sec, 8 sec, 12 sec, and 20 sec.

As expected, the 5-sec period has the largest power and is least affected by transient energy from earthquakes, which include the M_w 7.8 Haida Gwaii event that occurred on October 28, 2012 and its aftershocks. Interestingly, the 5-s power is only slightly elevated during Sandy's passage compared to the normal background level. The 8-sec power shows greater sensitivity to earthquake transients; however, it also shows greater dynamic range than the 5-s curve in responding to microseisms. In at least one case, on November 3–4, the TA stations respond simultaneously to two different storm systems, with the double-frequency peak splitting into a dominant subpeak near 5-sec and a weaker, narrower subpeak near 8 sec. The 12 sec and 20 sec bands show increasing sensitivity to earthquake transients with relatively subtle influence from single-frequency microseisms.

A strong diurnal pattern is evident over a broad range of periods. It is strongest at periods < 1.0 sec, which also show a weekly variation, implying that cultural factors such as traffic and construction are mainly responsible. Diurnal oscillation at longer periods, > 20 sec, lack a weekly signal and are more likely due to natural factors such as day-night temperature fluctuations that cause tilting of the seismometer, which in turn gets recorded as horizontal accelerations.

3.4.2 Spectrograms of Individual Stations

Noise power at individual TA stations share the general time-frequency behavior shown in the array-averaged spectrogram (Figure 3.2a); however, there is significant variation related to site effects and local noise sources, and there is less of a diurnal

signature compared to the array average. In Figure 3.3 we show results from four representative stations: A04D located the northwest corner of the United States on Lummi Island, WA; M54A located southeast of Lake Erie in Oil City, PA; S46A located in the center of the TA in Corydon, KY; and station 062Z located on an island of the Florida Keys in Marathon, FL. We again use power measured from the largest eigenvalue of the spectral covariance matrix, ensuring that the dominant noise source is fully represented no matter how it is polarized or from which direction it arrives.

Unsurprisingly, the most prominent feature in the spectrogram of the TA station A04D in Washington is the signal from the M_w 7.8 Haida Gwaii earthquake and its early aftershocks. The microseismic signal from Sandy is subtle and is less strong than the normal background microseisms that occurred before and after the passage of Sandy. This is probably due to the large distance of A04D from the east coast and the relatively high attenuation of seismic energy in the western U.S. The brightest microseism occurred November 3–4 with a dominant period near 8 s. A large peak occurs simultaneously at the corresponding single-frequency band, suggesting the microseismic energy was generated from a storm interacting with the coastline. The results using an ocean wave model confirmed the presence of the 8 sec seismic noise sources along western Canada and Alaska. In general, the single-frequency peak tracks the larger double-frequency peak, showing the same sort of gliding dispersion as a function of a time.

The TA station M54A, located near Lake Erie, shows a much stronger signal from Sandy. The peak near 5 sec for October 29–31 is the largest on the spectrogram and coincides with a sharp change in direction of Sandy. At this time Sandy's path changed from the northeast to the northwest, and the speed along the path increased (Figure 3.1).

Other double-frequency microseism arrivals that are lower in power occurred around October 18, October 24, and November. 3. The single frequency peak is visible almost throughout the entire period and often shows a dispersive gliding (e.g., October 21–22). As with other stations, this band was strongly contaminated by earthquake energy from the Haida Gwaii sequence. TA station S46A, located in Kentucky, shows features very similar to M54A, but with a smaller peak from Sandy, presumably due to its greater distance from the storm.

One of the most distinctive spectrograms is from the TA station O62Z, located on an island in the Florida Keys. Strong power was observed at 1 sec for the entire time that Sandy was active, even when it was south of Cuba with low wind speeds. Owing to the relatively short period, it is likely that this energy is related to an increase in local wind speeds. The strongest signal associated with Sandy occurs over a relatively wide band of 3–5 sec, with peak energy associated with the Sandy turn over October 29–31. Interestingly, 062Z shows an increase in power at periods greater than 20 sec, associated with the passage of Sandy. Significant power exists up to at least 300 sec and may be especially observable at O62Z because of its island or coastal setting.

3.4.3 Time Evolution of the Dominant Microseismic Period

As shown in the previous spectrogram figures, there is noticeable drifting of the dominant period (i.e., period with the highest power) within the microseismic band. In Figure 3.4 we present the time and spatial evolution of these dominant periods, with a complete animation available in the electronic supplement. Site effects are clearly seen, with stations in Florida nearly always dominated by 1–3 sec energy, while the remainder

of the array is commonly characterized by 5–6 sec energy. It is possible that unusual winds or the peninsular nature of Florida are partially responsible for the period reduction in microseismic noise; however, stations along the Gulf coast and further north along the Mississippi valley also often have reduced microseismic periods suggesting that the enhanced sediment thickness in these areas (e.g., Laske and Masters, 1997) preferentially traps shorter-period microseismic energy. It is only when Sandy passed north over the Bahamas Islands on October 27 that all the Florida stations have peak periods near 5 sec.

The most dramatic feature seen in the animation of peak period is the sharp rise on October 29, at the time when Sandy makes an abrupt turn from the northeast to the northwest and increases the speed at which it is travelling. Here the dominant periods across much of the TA quickly rise to 8–9 sec and then gradually drop back to 5 sec as Sandy approaches the coastline and makes landfall. The drift to long periods does not seem to be a path effect, in which shorter-period energy is preferentially attenuated, because the storm locus does not change significantly. Likewise, the wind speeds and bathymetry are similar before the turn and when the turn begins. Therefore, we attribute the increase in period to stronger wave-wave interaction as the storm turns.

3.4.4 Time Evolution of the Microseismic Wavefield Across the TA

We examined the distribution of power and polarization across the TA in spatial and time domains for a wide range of periods (0.5–200 sec) but here we present the results for the 5-sec (Figures 3.5, 3.6), 8-sec (Figures 3.7, 3.8), and 12-sec (Figures 3.9, 3.10) periods, focusing on the classic double-frequency and single-frequency microseism bands. The location of the hurricane's eye and the maximum sustained wind noted on the

figures were taken from the Sandy Graphics Archive web page of the National Hurricane Center (http://www.nhc.noaa.gov/archive/2012/graphics/al18/loop_3W.shtml).

The first figure for each period (Figures 3.5, 3.7, and 3.9) includes several frames that show spatial variation of dominant eigenvalue power across the TA, at the times indicated by arrows on the array-averaged curve in the top panel. Earthquakes can be seen as spikes in the time series, whereas the microseismic arrivals can be seen as longer period humps, with a gradual increase, possibly a flat top, and then a gradual decrease in power. Complete animations for each period are included in the electronic supplement.

The second figure associated with each period (Figures 3.6, 3.8, and 3.10) includes several frames that show the spatial variation of Θ_H, the horizontal azimuth of the major axis of the polarization ellipsoid, at specific times. The lengths of the vectors are weighted by the degree of polarization (β^2), with more polarized ground motion having longer lines. The array average value of (β^2) is shown as a function of a time across the top panel, with red arrows indicating the time for each frame. As in the case of array-averaged power, earthquakes appear as spikes and microseismic arrivals appear as smooth humps.

Unless otherwise noted, the observed energy is consistent with the Rayleigh wave propagation. Histograms of phase differences between the vertical and dominant horizontal components (φ_{VH}) are generally clustered around ±90°. We note that the positive values do not necessarily indicate prograde motion since they can also be interpreted as retrograde arrivals from the opposite direction, Θ_H +/-180 (Park et al., 1987). In general, we find that selecting the direction corresponding to $\varphi_{VH} \sim -90°$ gives the expected result; however, this is not universally true, especially when the degree of

polarization is relatively low. This may be caused by numerical instability or perhaps actual prograde Rayleigh wave particle motion caused by an unusual velocity structure (Tanimoto and Rivera, 2006). For this reason, we do not use heads on the vectors indicating Θ_H.

3.4.4.1 The 5-sec Microseismic Field

During the 18-day study period, the 5-sec wavefield was the least contaminated by earthquakes in terms of power (Figure 3.5) and degree of polarization (Figure 3.6). The effects of Hurricane Sandy were observed beginning on October 25, as Sandy gained wind speed and began moving northward from Cuba as a category 1 hurricane. As Sandy reached the coast of Florida, the microseismic power increased and reached its first peak around October 27 08:00 UTC (the second and third time frames from Figure 3.5). Following this first maximum, the microseismic energy decreased as Sandy moved away from the Florida coastline to the northeast. As Sandy approached the coasts of New Jersey, New York, and Delaware on October 29 21:00 UTC, the second maximum was observed in the array-averaged microseismic energy (the fifth time window in Figure 3.5). After this point, Sandy lost its energy and rotation and became a posttropical depression on land. This resulted in a significant decrease in the array-averaged energy (the sixth time frame in Figure 3.5).

The power results are consistent with the degree of polarization figures (October 27, 21:00 UTC time frame and the October 29, 21:00 UTC time frame from Figure 3.6). It can be seen that the station polarization vectors are pointing to one specific region for each time frame. The second time frame is associated with Hurricane Sandy's northeast

motion, away from the Florida coastline and all the stations are pointing to the southeast of TA network. The third time frame is associated with the turning (westward motion, towards Long Island, New York), and all the vectors are pointing to the west of TA network.

We also observed three domains in the array-averaged power not correlated with Sandy. The first domain in microseismic power was observed October 18–21 (Figure 3.5). This decrease in power was most likely associated with the previous North Atlantic storm known as hurricane Rafael (National Hurricane Center, Hurricane Rafael advisory archive; www.nhc.noaa.ov/archive/2012/RAFAEL.shtml). Following this, there was a broad peak in the microseismic power on October 22–25 that coincided with the initiation of Sandy (October 22 15:00 UTC time frame, Figure 3.5). The northeast-southwest polarized vectors from the first time frame in Figure 3.6 indicate two possible source regions; northeast pointing to the North Atlantic or southwest direction pointing to the Gulf of Mexico. Assuming that the arrivals are standard retrograde Rayleigh waves, the φ_{VH} values near -90° that are observed imply a North Atlantic origin. The third domain occurs November 3–4 (Figure 3.5), with the polarization analysis again indicating a North Atlantic origin.

3.4.4.2 The 8-sec Microseismic Wavefield

The 8 sec period is another interesting region in the double-frequency microseism band, with fluctuation in the array-averaged power curve greater than that observed for the 5 sec period (Figure 3.7). As Sandy approached the coast of Florida, there was an increase in power, and even as Sandy moved away from Florida to the northeast, this

increasing trend continued until being interrupted by surface waves of M_w 7.8 Haida Gwaii earthquake and its aftershocks. Following this interruption, the maximum amplitudes were observed as Sandy made a turn to the west (towards New Jersey and Delaware) (October 29, 16:00 UTC time frame from Figure 3.7). Following that, the microseismic energy started gradually decreasing as Sandy made landfall and became a posttropical depression near Lake Erie (the last time frame from Figure 3.7).

Our 8 sec power results are complemented by the degree of polarization curve and the spatial polarization maps shown in Figure 3.8. The first and third time frames indicate regions where the 8-sec energy was generated. The first time frame (October 26, 22:00 UTC) points to the southeast when Sandy approached the coast of Florida. The third time frame (October 29, 14:00 UTC) points to the east of the TA when Sandy made its westward turn. These regions are probable microseismic source locations coinciding with Sandy's position. The second time frame in Figure 3.8 (October 28, 15:00 UTC) is an exception in terms of coincidence of source region and Sandy's position. As seen from the map, the polarization vectors point to the south of Sandy's location. This shows the source region is located somewhere in the wake of the hurricane.

A final observation we make is the orientation of the polarization vectors for the map of November 3, 18:00 UTC. They are polarized in a northwest-southeast direction, different from the 5-second energy that is polarized northeast-southwest during the same time period. Relative phase observations for the 8-sec energy support retrograde Rayleigh waves arriving from somewhere in the Northern Pacific. These two different results indicate 5-sec energy and 8-sec energy are sensitive to source regions in different oceans.

An interesting feature of the 8-sec power maps (Figure 3.7) is finger-like

striations that are aligned in the direction of the microseismic source. These features are apparent in the time frames of October 26 23:00 UTC, October 27 20:00 UTC, October 29 16:00 UTC from Figure 3.7, but are most clearly viewed in the supplementary animation. These features were also seen during the passage of other distant storms and the Haida Gwaii earthquakes, and they always pointed towards the source. We think these patterns vary too quickly with azimuth to be related to any irregular near-source bathymetric feature, and instead are related to the focusing and defocusing of energy propagating in a 3-D Earth.

3.4.4.3 The 12-sec Microseismic Wavefield

The single frequency microseism band is generally defined between 10 seconds and 16 seconds. Although each period in this band is sensitive to different aspects of microseisms, we present the 12-second energy because of its strong response to Sandy's motion towards Florida. With the exception of earthquakes, the 12-second microseismic power did not vary nearly as much as it for 5-second and 8-second periods. However, the second time frame (Oct. 26 07:00 UTC) and particularly the fourth time frame (Oct. 29 18:00 UTC) in Figure 3.9 indicate a rise in power across the TA stations. Increased amplitudes are seen when Sandy reached the shallow waters of Florida and when Sandy changed course to the west. However, the westward turn is mostly masked by the M_w 7.8 Haida Gwaii mainshock and its aftershocks.

Weak, but recognizable, finger-like radiation patterns are also observed in this period and other nearby periods of the single frequency microseism band (October 26 07:00 UTC time frame in Figure 3.9). The higher degree-of-polarization values coincide

with the time period when these patterns are present (Figure 3.10). The most interesting observation in the 12–sec band is the azimuthal orientation of the polarization vectors. The first time frame in Figure 3.10 shows polarization vectors oriented orthogonal to those from the 5-second and 8-second periods, suggesting Love wave particle motion. This idea is reinforced by considering the phase differences between the horizontal and vertical components. In Figure 3.11, we compare histograms of φ_{HH} and φ_{VH} for the prospective 12-s Love waves to those from typical 8-s Rayleigh waves. For the prospective Love waves the φ_{HH} distribution is strongly peaked around 0°, while the φ_{VH} distribution is flat across all angles, indicative of linearly polarized motion in the horizontal plane with insignificant motion on the vertical component. The Rayleigh waves, in contrast, have a flat φ_{HH} distribution and a φ_{VH} distribution strongly peaked around ±90°, indicative of elliptical particle motion in the vertical-radial plane and insignificant motion on more than one horizontal component.

It is unclear precisely how Love waves are generated from ocean waves, and here we speculate that they may be generated by the interaction of storm/hurricane-induced ocean waves with small-wavelength bathymetric features (such as small islands and seamounts) that act as secondary, Huygens-type sources of seismic energy. In order to validate this hypothesis, synthetic modeling of the 3D coupled ocean-solid Earth system is required.

3.5 Discussion

Analysis of microseisms created by Superstorm Sandy and recorded across the TA shows that the overall strength of the microseismic energy varied considerably as the

storm progressed. As expected, double-frequency microseismic energy was dominant, with the peak energy occurring on October 29 as the storm shifted sharply to the northwest and accelerated. A smaller peak occurred on October 27 as the storm crossed over the Bahamas and turned toward the northeast. In both of these cases, and more generally throughout the observation period, the dominant period was positively correlated with power, varying mainly between 5 and 8 seconds.

The TA-averaged microseismic power created by Sandy was only slightly larger than the background microseismic power created by storms in the North Atlantic and North Pacific at around the same time. For instance, North Atlantic storms occurring around October 22–23 and November 3–4 generated microseisms with a dominant period near 5 sec and nearly the same power as Sandy. Likewise, a northeastern Pacific storm on November 3–4 generated significant microseismic power at a period near 8 sec.

The polarization vectors of the 5-sec and 8-sec energy tracked the motion of Hurricane Sandy closely. They generally pointed towards the eye of the hurricane as the source region, but also sometimes lagged slightly behind the eye, pointing to a source region in the storm's wake. The TA-averaged degree of polarization was positively correlated with average power and period and peaked when Sandy sharply turned direction on October 27 and October 29. In general, the polarization analysis indicated that Sandy created mainly Rayleigh wave energy, with evidence of Love wave generation in the single-frequency band as the storm passed over the Bahamas.

Figure 3.12 shows the computed daily averages of the power spectral density of the equivalent pressure generated by the ocean surface gravity waves (Ardhuin and Herbers, 2013) using the Ifremer version 4.07 of the WAVEWATCH-III ocean wave

model (Tolman, 2002). The global model has a spatial resolution of 0.5° in latitude and longitude and incorporates coastal reflections (A discussion of the model parameterization is presented in Ardhuin et al., 2011). The frames for the dates of October 27 and October 29 show significant wave-wave interactions (for seismic periods of 5 sec and 8 sec) occurring close to the Florida coastline and off the coasts of New Jersey, Delaware and New York, respectively. Our results of 5 sec and 8 sec polarization vectors were pointing towards these regions where the maximum in spectral power was predicted by the ocean wave model for those specific dates. We also observed a similar situation for microseisms not related to Sandy. On November 3, there were two different regions with peak spectral power, one in the North Atlantic located off the east coast of Greenland (5 sec) and another region in the Northeast Pacific (8 sec). These regions are also consistent with the polarization vectors of 5-s and 8-s periods from the November 3, 22:00 UTC time frame in Figure 3.6, and the November 3, 18:00 UTC time frame in Figure 3.8. This explains the splitting of double frequency microseism band for the dates of November 3–4 in the array-averaged spectrogram (Figure 3.2).

Ardhuin et al. (2011) recently presented a classification system for microseismic generation from wave-wave interactions in the ocean. They based their classification on sea states with the following definitions: class-I is the mechanism where ocean waves generated by a rapidly moving storm interact with trailing waves in the opposite direction, class-II involves coastally reflected ocean waves interacting with the incident waves propagating in the opposite direction, and the class-III mechanism is the interaction of ocean wave groups generated by two separate storm systems. Considering the directions of 5-s and 8-s polarization vectors for October. 27 and October 29 and the results from

the numerical ocean wave model, we conclude that the microseisms from Sandy were generated mainly by a class-I mechanism type (similar to the mechanism IIIa described in Figure 2a by Ardhuin et al., 2011) .

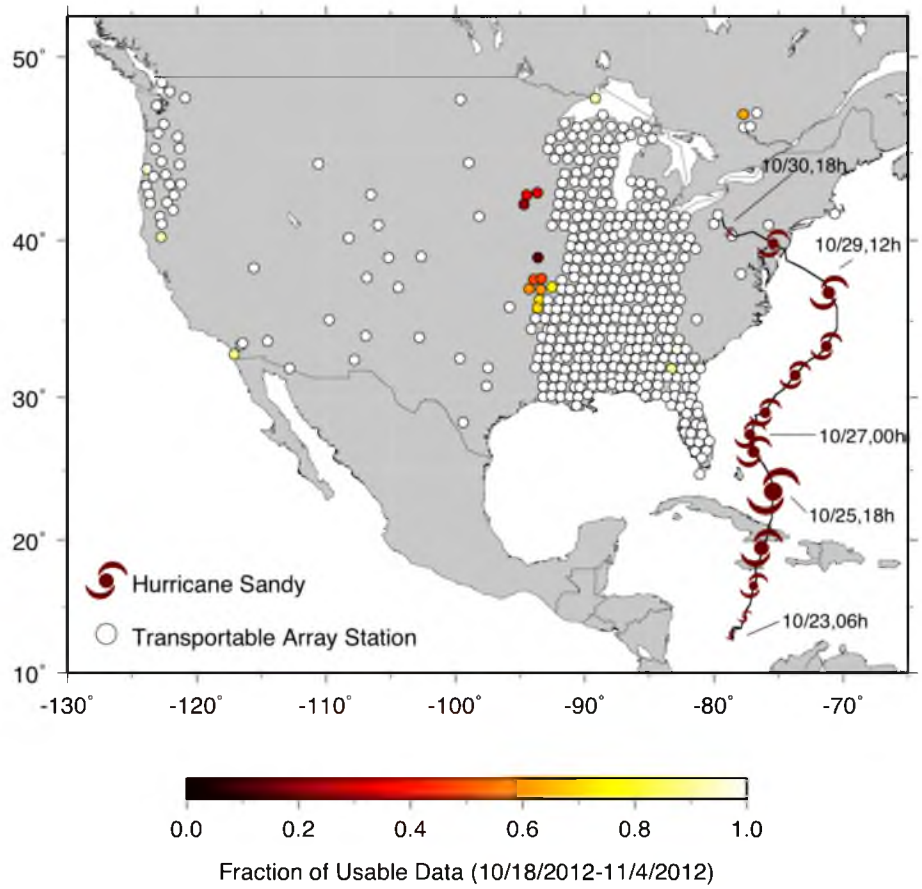

Figure 3.1 Map of TA station geometry during the time Superstorm Sandy was active. Circles indicate seismometer locations, with color indicative of data completeness. The track of Sandy is shown using hurricane symbols equally spaced in time from Oct. 22, 2012 through Nov. 1, 2012, with symbol size proportional to wind speed.

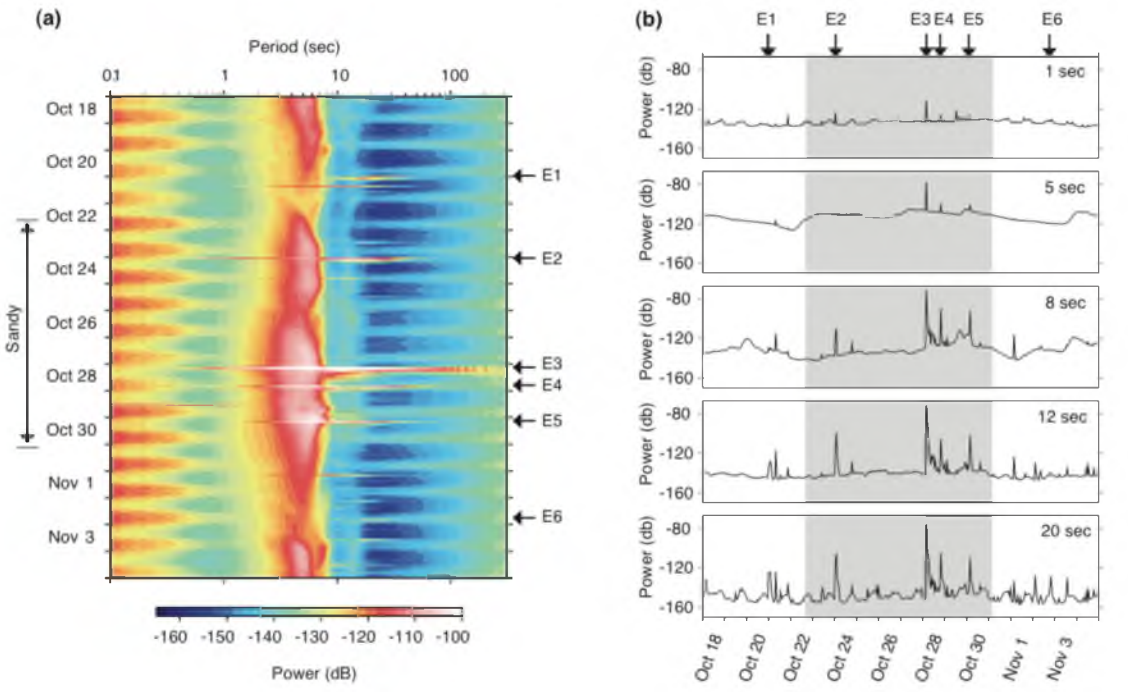

Figure 3.2 Array-averaged spectrogram and selected individual periods from single and double frequency microseisms for the dates of October 18–November 4, 2014. a) Array-averaged spectrogram of the dominant eigenvalue of the spectral covariance matrix. Earthquakes appear as horizontal lines and those with magnitudes larger than M_w 6.0 are highlighted with arrows: E1 - M_w 6.2 event in Vanuatu, E2 - M_w 6.5 event in Costa Rica, E3 - M_w 7.8 event in Haida Gwaii, E4 - M_w 6.3 event in Haida Gwaii, E5 - and M_w 6.2 event in Haida Gwaii, and E6 - an M_w 6.1 event in the Philippines. (b) Array-averaged values of power for the dominant eigenvalue of the spectral covariance matrix across a range of periods in the microseism band of ~1–20 sec. Grey shading is used for the time when Sandy was active.

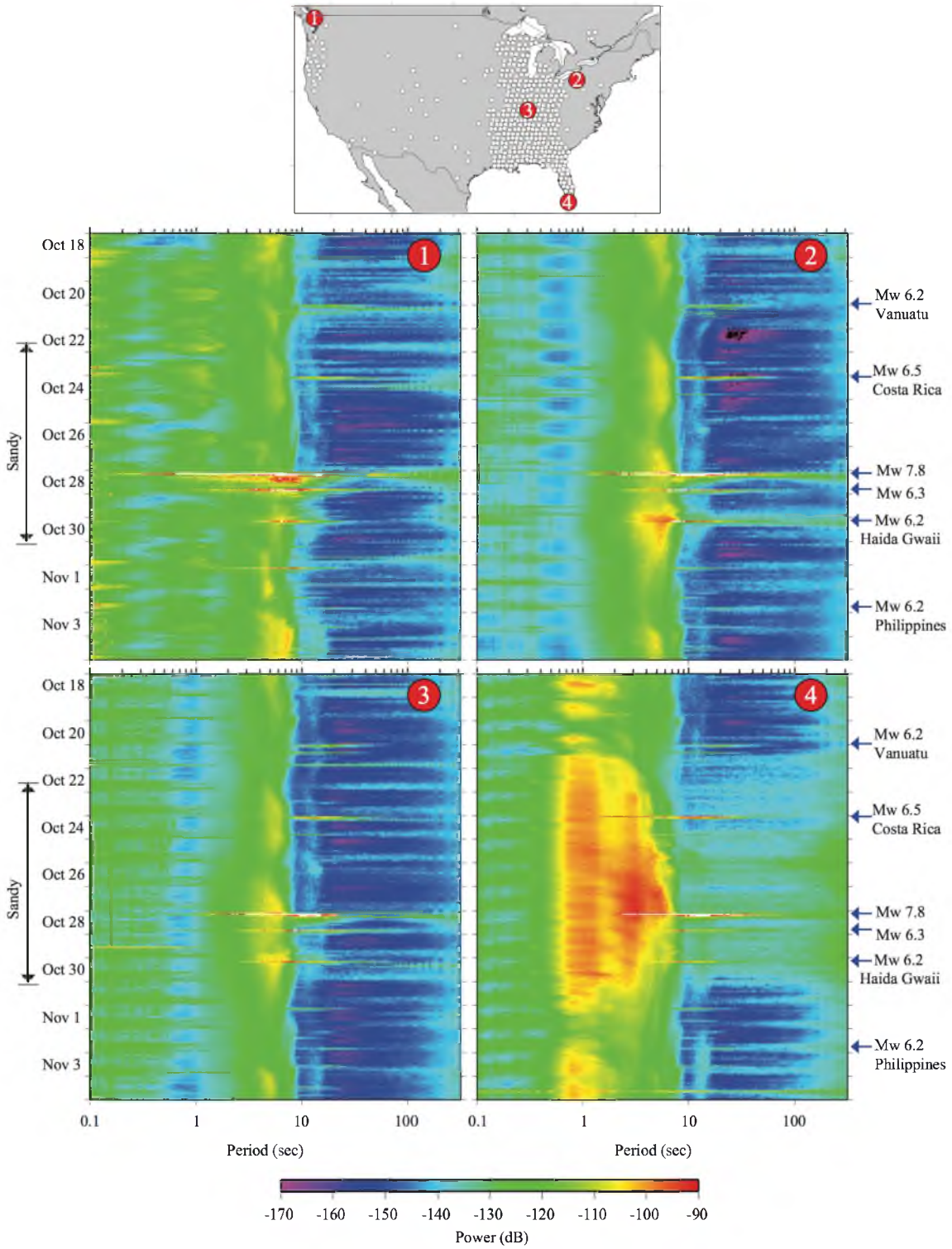

Figure 3.3 Spectrograms of dominant eigenvalue power for four TA stations. Stations 1–4 correspond to TA stations A04D, M54A, S46A, and 062Z, respectively. Earthquakes with magnitudes of at least 6.0 M_w are noted on the right with blue arrows, and time extent of Sandy is indicated on the left with the black arrows.

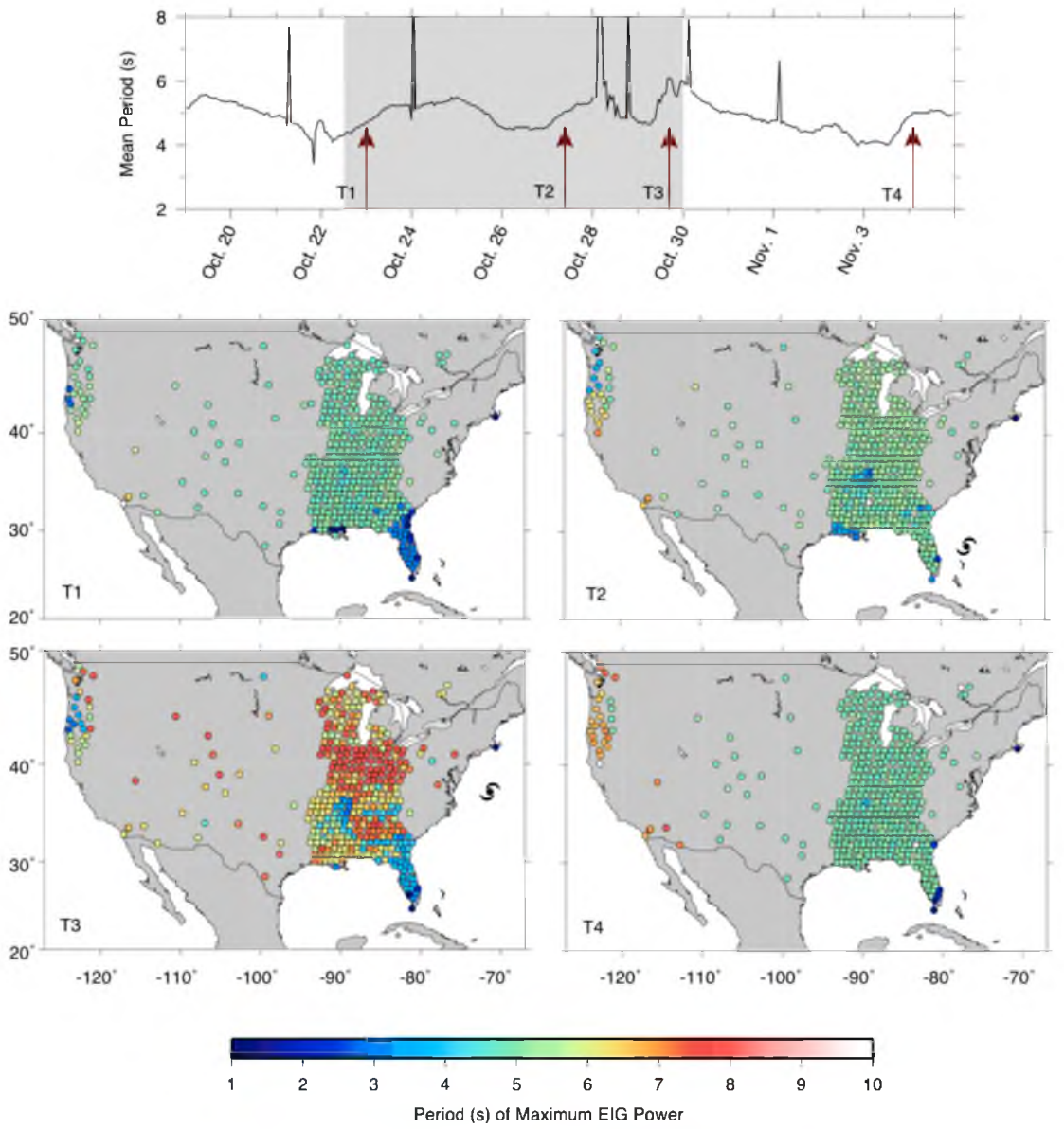

Figure 3.4 Periods corresponding to the largest eigenvalue power in the microseismic band. The top panel shows the array-averaged period as a function of time, with grey shading used to indicate the time Sandy was active. The four bottom panels show the spatial variation in dominant period at the times indicated by arrows in the top panel.

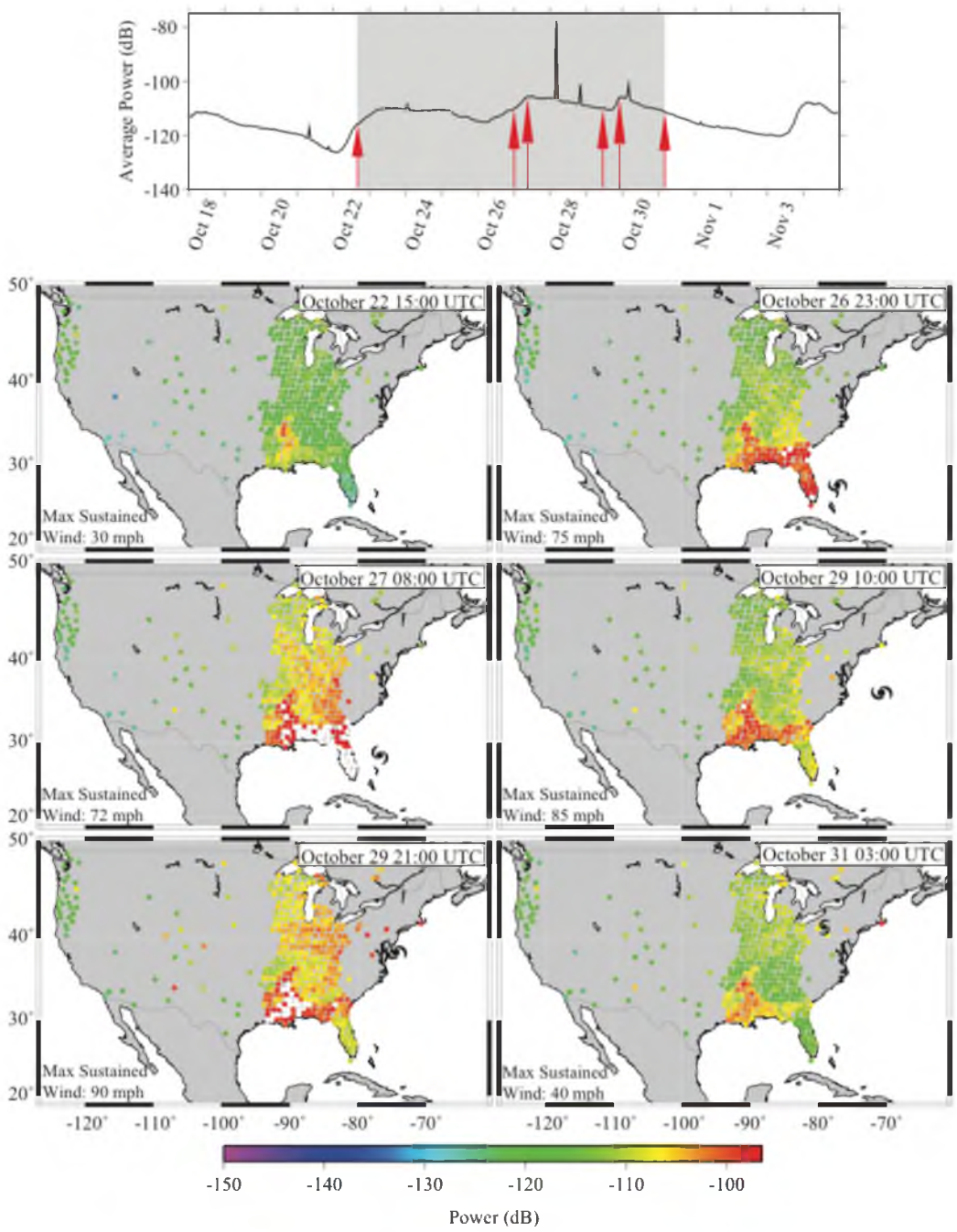

Figure 3.5 Variation in 5-sec power across space and time, where power is calculated from the dominant eigenvalue of the covariance matrix. The top panel shows the array-averaged variation in 5-sec power with grey shading used during the time Sandy was active. The red arrows indicate times for which the spatial variation in 5-sec power is shown below in an individual panel. A full animation is available in the electronic supplement.

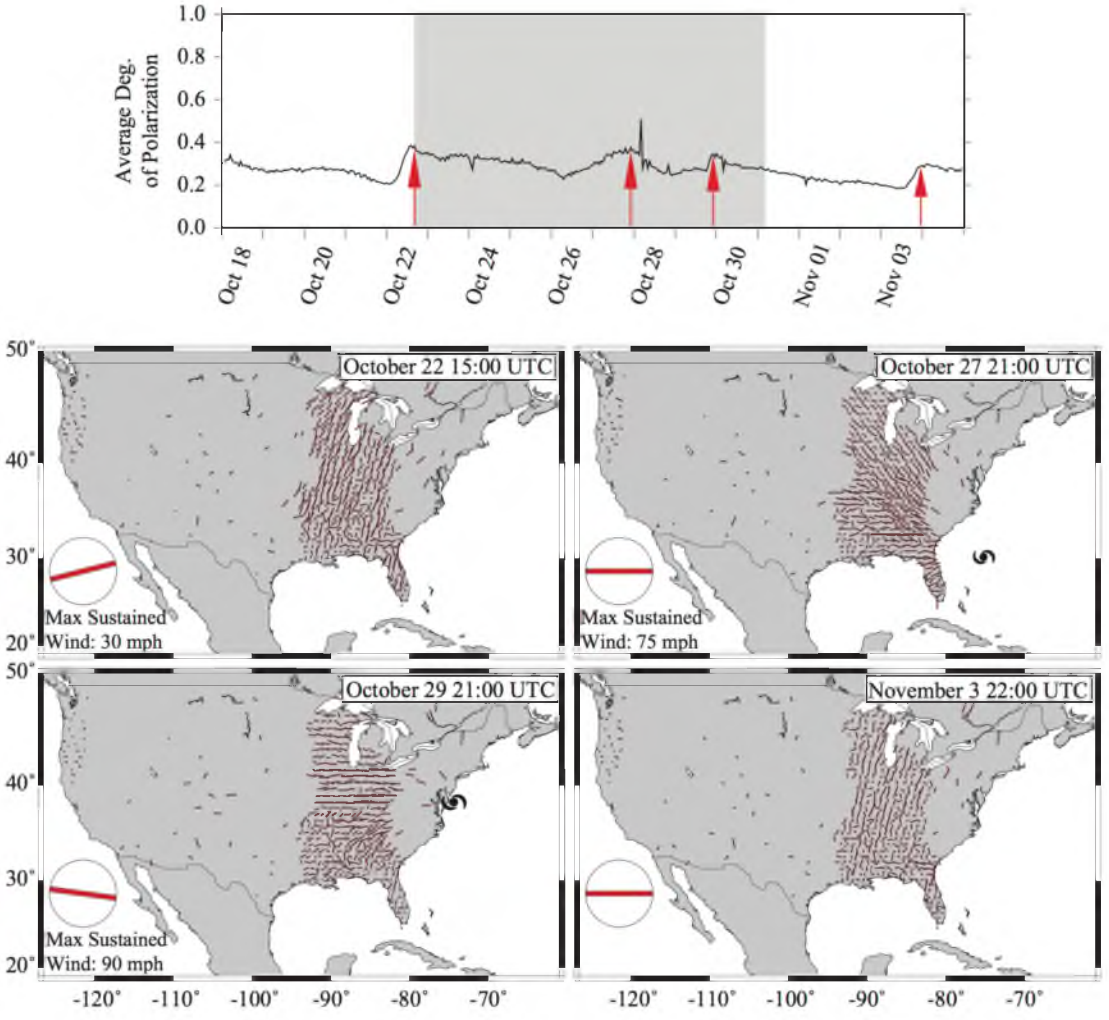

Figure 3.6 Variations in the polarization of 5-sec energy across space and time. The top panel shows the array-averaged variation in the degree of polarization, β^2. Grey shading is used to indicate the time extent of Sandy and the red arrows correspond to the times of the four panels shown below. Each panel shows the azimuthal orientation of the polarization ellipsoid, Θ_H, at each station, with length scaled by β^2. The array-averaged value of Θ_H is shown by the large red line in the lower left corner of each panel. Hurricane symbols are used to show the location of Sandy. A full animation is available in the electronic supplement.

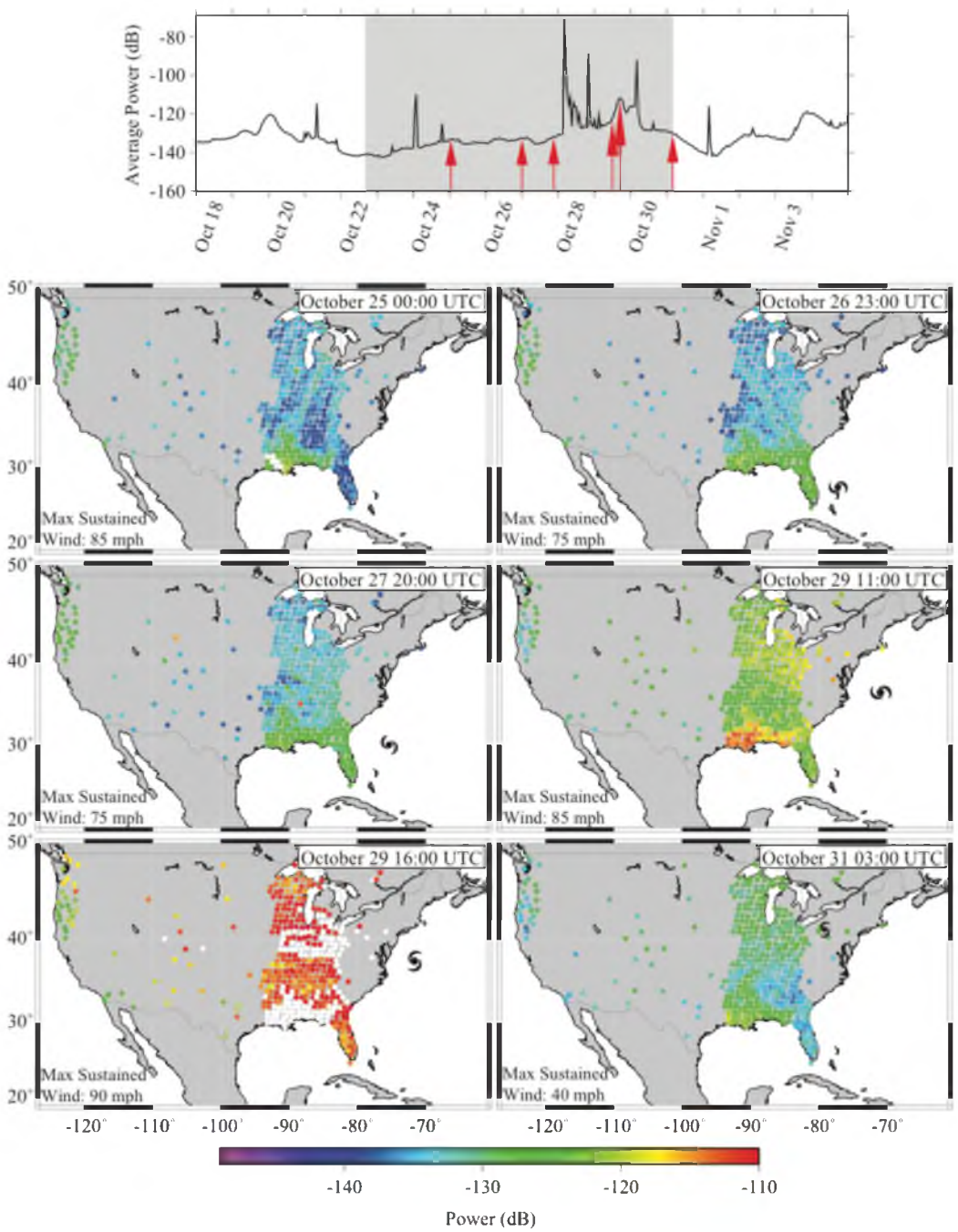

Figure 3.7 The same as Figure 3.5, but for a period of 8 sec. A full animation is available in the electronic supplement.

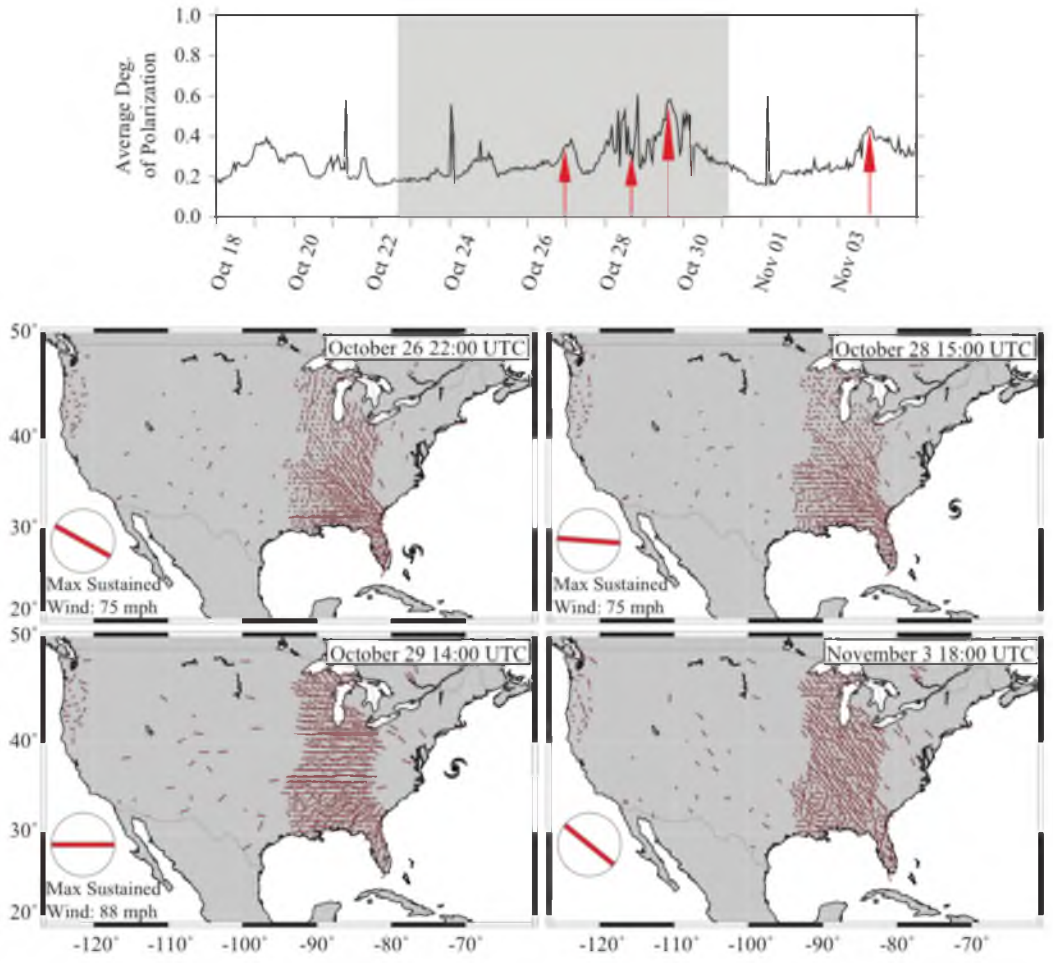

Figure 3.8 The same as in Figure 3.6, but for a period of 8 sec. A full animation is available in the electronic supplement.

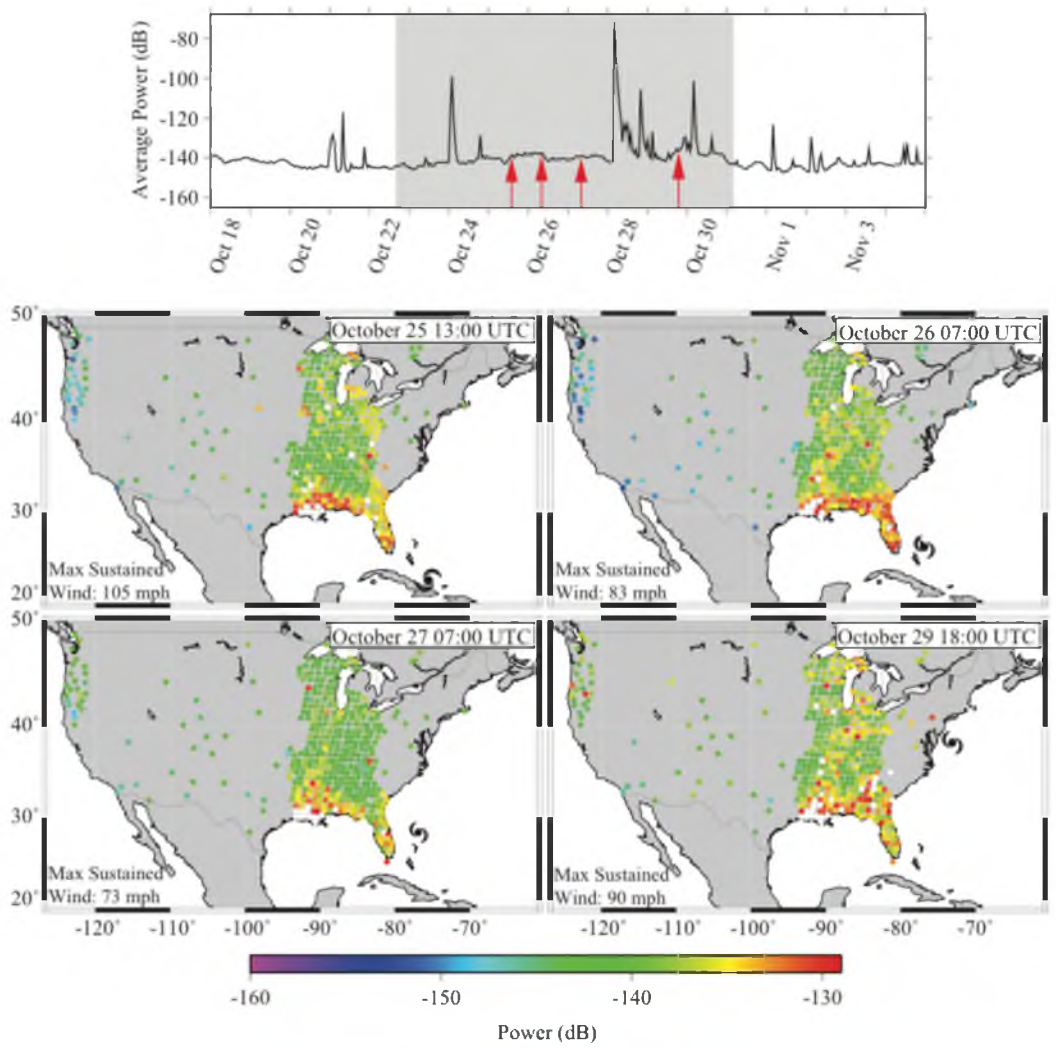

Figure 3.9 The same as in Figure 3.5, but for a period of 12 sec. A full animation is available in the electronic supplement.

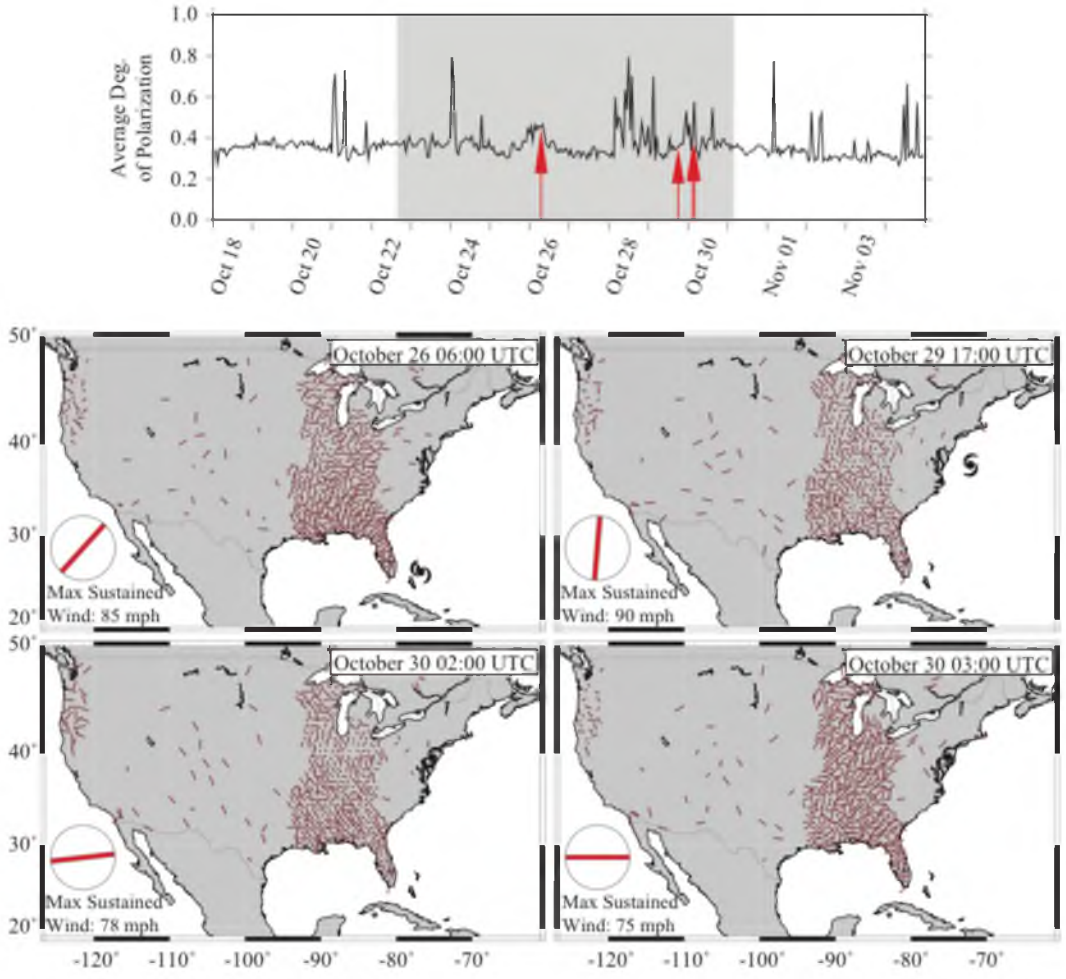

Figure 3.10 The same as in Figure 3.6, but for a period of 12 sec. A full animation is available in the electronic supplement

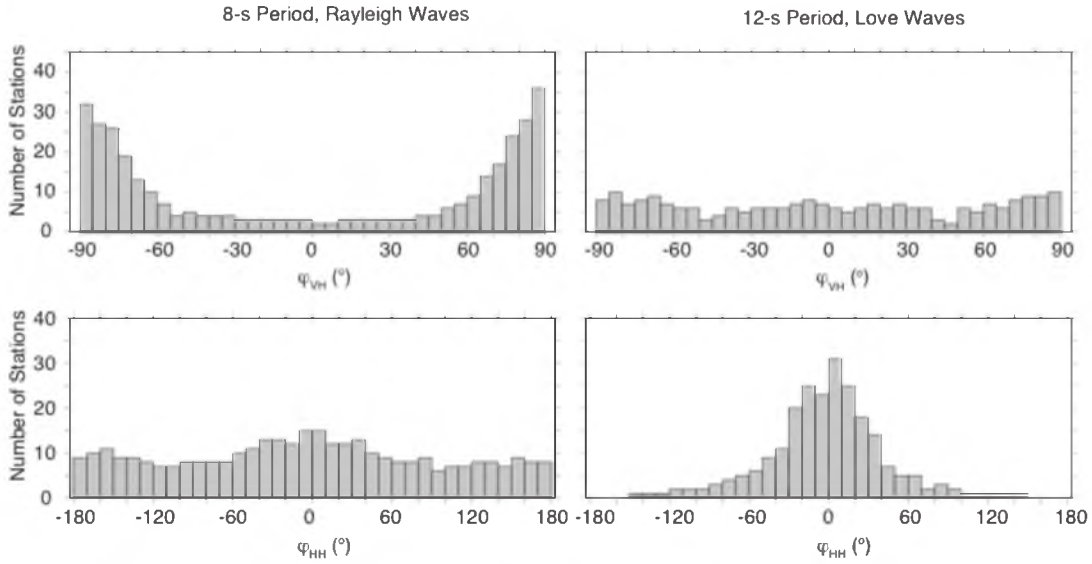

Figure 3.11 Distribution of phase differences between the vertical and dominant horizontal components (φ_{VH}) and the two horizontal components (φ_{HH}). The panels on the left are typical of energy recorded at 5 sec and 8 sec throughout the study period, while the panels on the right correspond to stations showing azimuthal polarization orientation (Θ_H) at 12 sec that is orthogonal to the direction of Sandy. In both cases, eigenvectors were analyzed for a 16-hr period (Oct. 25, 19:00 UTC though Oct. 26 10:00 UTC) for those stations with $\beta^2 > 0.15$.

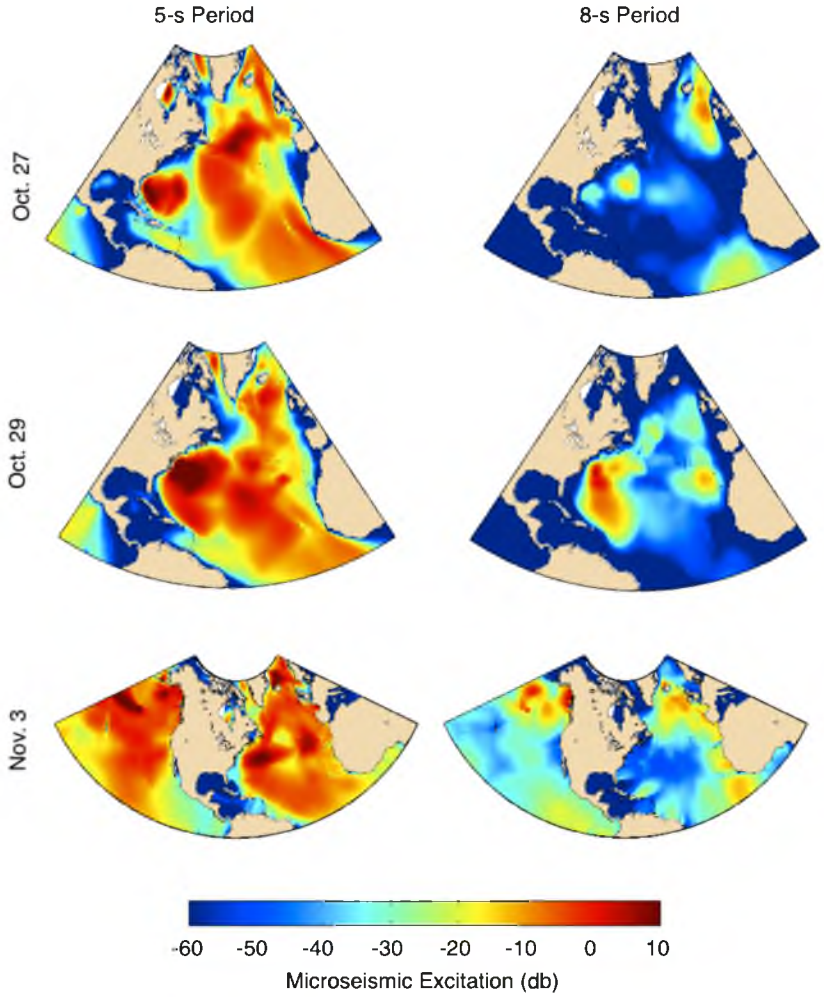

Figure 3.12 Daily averaged power spectral density of the equivalent pressure generated by the ocean surface gravity waves, corresponding to seismic periods of 5 sec and 8 sec, computed from the WAVEWATCH-III Ifremer model. The top frames show the time when Sandy approached the Florida coastline (Oct. 27), and the middle frames show the power spectral density at the time when Sandy made the sharp westward turn (Oct. 29). The bottom frames indicate the modeled power for the North Atlantic and Pacific oceans for the time when the splitting of the double frequency microseism band occurred (Nov. 3)

CHAPTER 4

DISCUSSION AND CONCLUSION

I cataloged and described microseisms recorded by the Earthscope Transportable Array for the calendar year of 2009. I indicated geographical regions capable of generating strong microseisms and their predominant peak seismic periods. I found that Type I microseisms were dominant in the Northeast Pacific Ocean (Gulf of Alaska and the Queen Charlotte Islands Region) and East-Central Pacific Ocean (Southern California, Baja California, and Southern coast of Mexico). Their dominant peak seismic period was around 8 s. The Type II microseisms were found to originate from the Gulf of Mexico and along the coast of Newfoundland and Labrador and had dominant peak seismic period of 4–5 sec. I found that single sources were the cause of Type I and Type II microseism groups.

On the other hand, Type III and Type IV microseisms were observed in both the Pacific and Atlantic oceans: the north and east-central Pacific, and the north Atlantic Oceans with the peak seismic periods of 5–8 sec. In addition, the Hudson Bay was also a strong Type IV microseism generator. Different from Type I and Type II, the Type III and IV microseisms were generated by the combination of multiple sources from either different oceans or the same ocean.

Previous studies indicated that the Baffin Bay, Labrador, and Newfoundland

regions were not able to generate long-period double-frequency microseismic energy (Sergeantet al., 2013). The explanation given was that the region is not capable of generating long-period ocean waves (more than 10 sec) combined with shallow water depths. In this study, I was able to identify some long-period double-frequency microseismic energy (5–7 sec) propagating from the Newfoundland region. However, polarization vectors of the TA network indicated broader source regions in this part of the North Atlantic Ocean (during the year of 2009). It could be that these long-period double-frequency microseism sources are generated at the entrance of Baffin Bay where the water depths are greater. Azimuthal back projection may indicate more precise locations and give a better answer whether these regions are capable of producing long-period microseisms or not.

I also presented how microseisms generated by hurricane- and storm-driven ocean waves could be tracked and analyzed. This was highlighted in a case study from 2012 during the passage of Hurricane Sandy. It is widely thought that microseisms mostly propagate as Rayleigh waves. However, I found that there was also possible Love wave generation observed in the single-frequency microseism band in the vicinity of the Bahamas. The source mechanism for this Love wave generation was explained as possible sideways displacement of seamounts and/or islands induced by hurricane driven ocean waves. Modeling the source and seismic wave propagation from this region could yield more precise conclusions. The other key finding of this study was that microseismic energy sharply increased as the hurricane made its westward turn towards New York. This was best observed on the array-averaged power curves and power of individual stations of periods of 5 and 8 sec.

APPENDIX

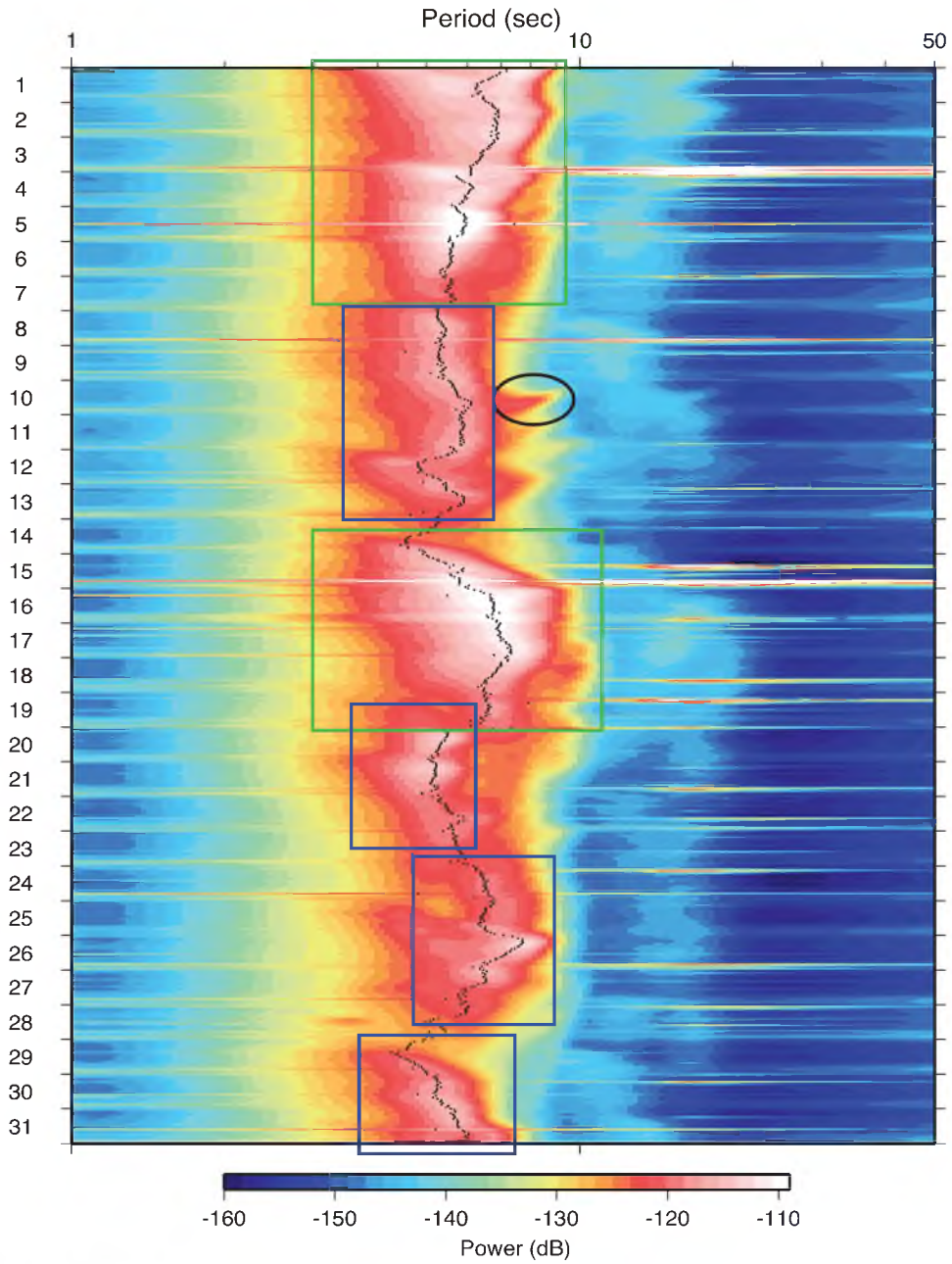

Figure A.1 Array average spectrogram of January 2009.

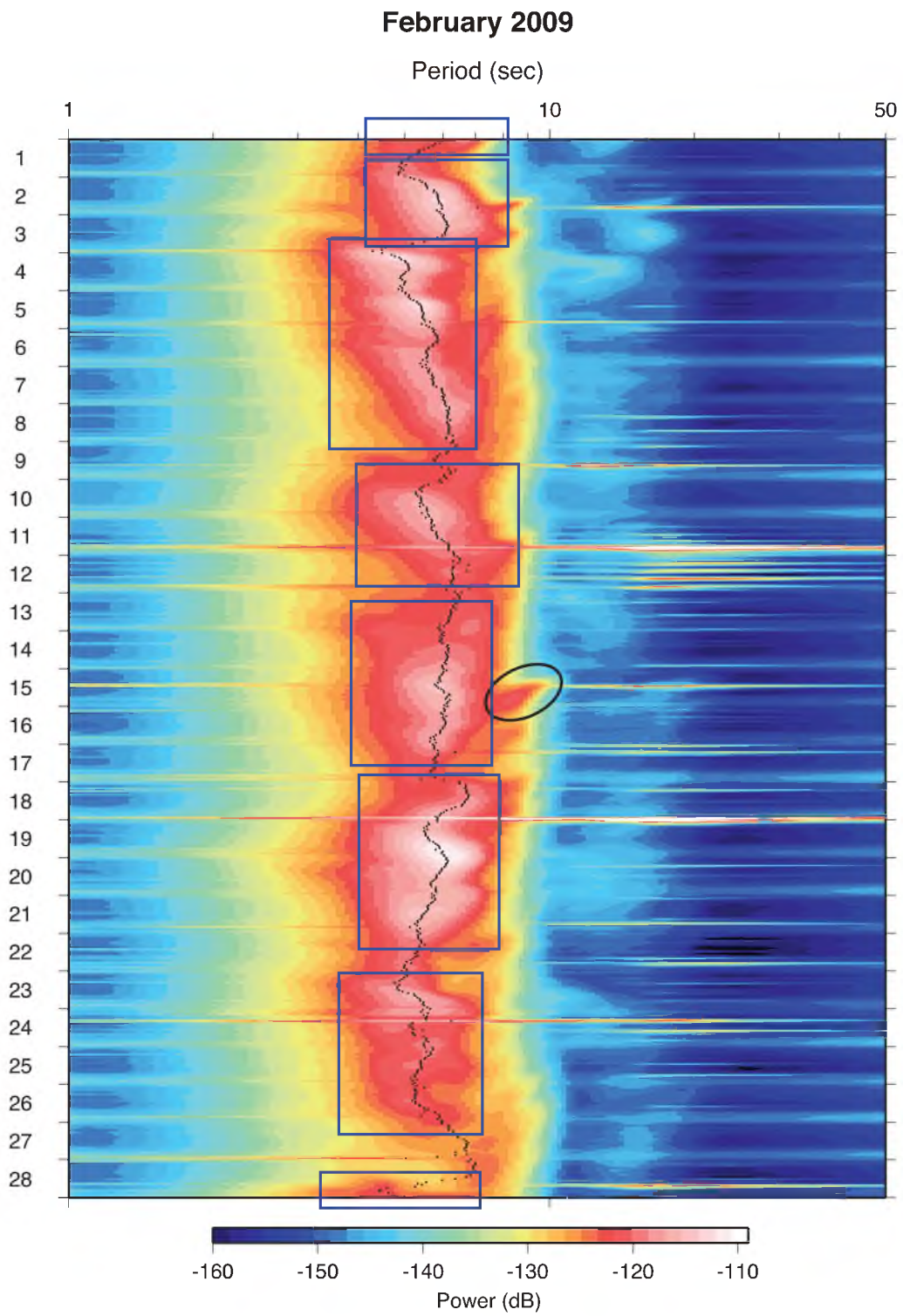

Figure A.2 Array average spectrogram of February 2009. The black ellipses, purple ellipses, blue rectangles, and green rectangles show picked Type I, Type II, Type III, and Type IV microseisms, respectively.

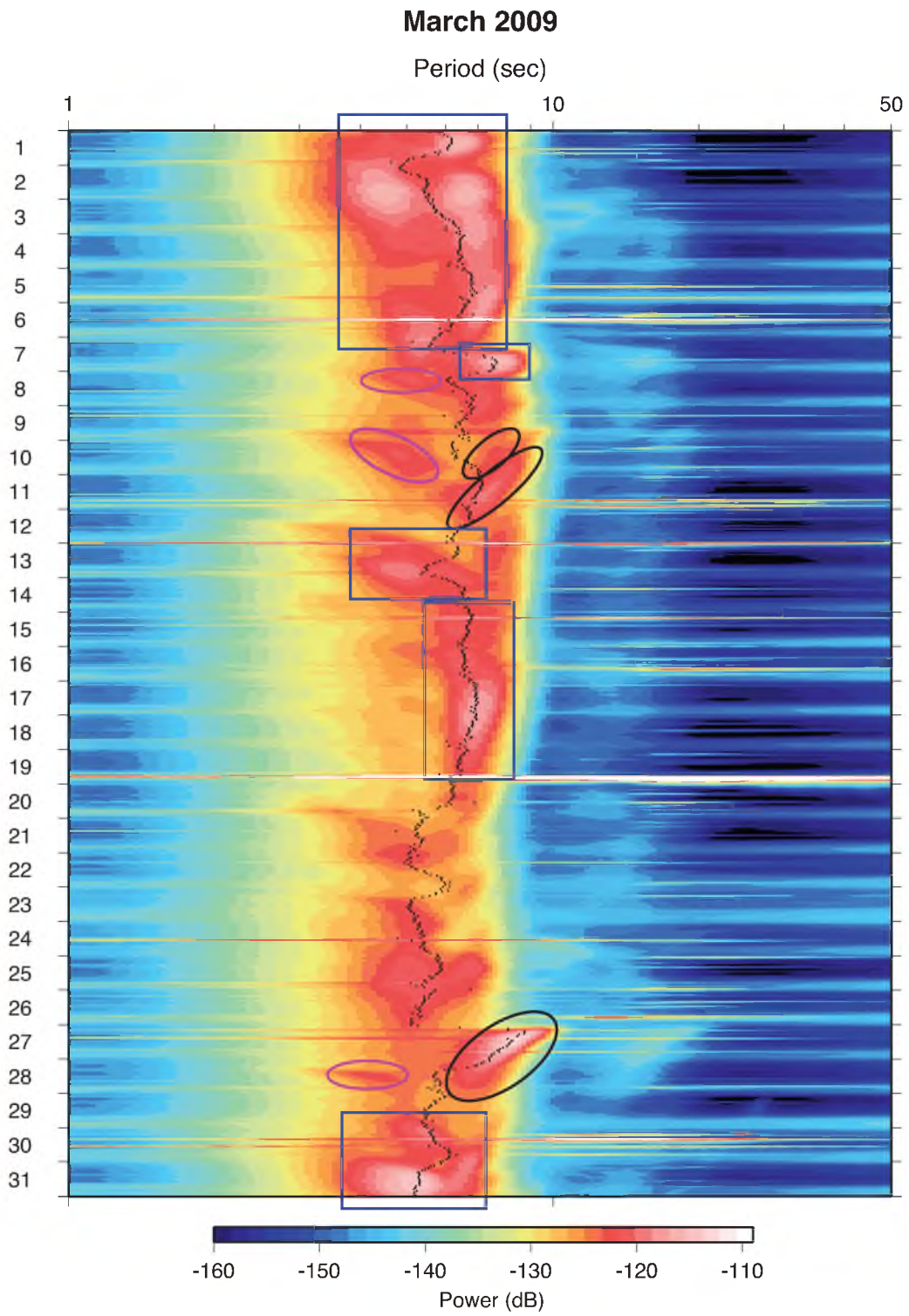

Figure A.3 Array average spectrogram of March 2009. The black ellipses, purple ellipses, blue rectangles, and green rectangles show picked Type I, Type II, Type III, and Type IV microseisms, respectively.

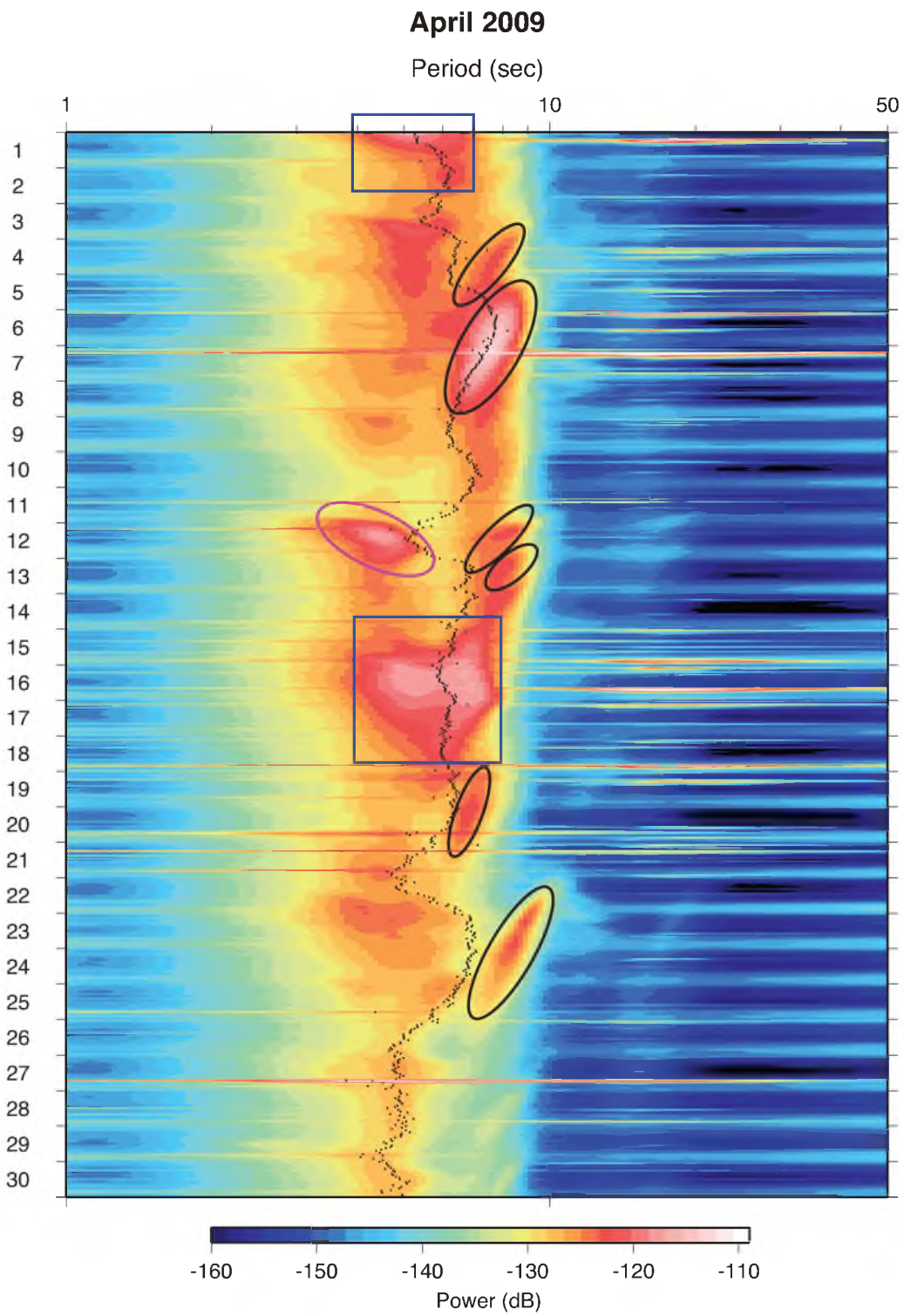

Figure A.4 Array average spectrogram of April 2009. The black ellipses, purple ellipses, blue rectangles, and green rectangles show picked Type I, Type II, Type III, and Type IV microseisms, respectively.

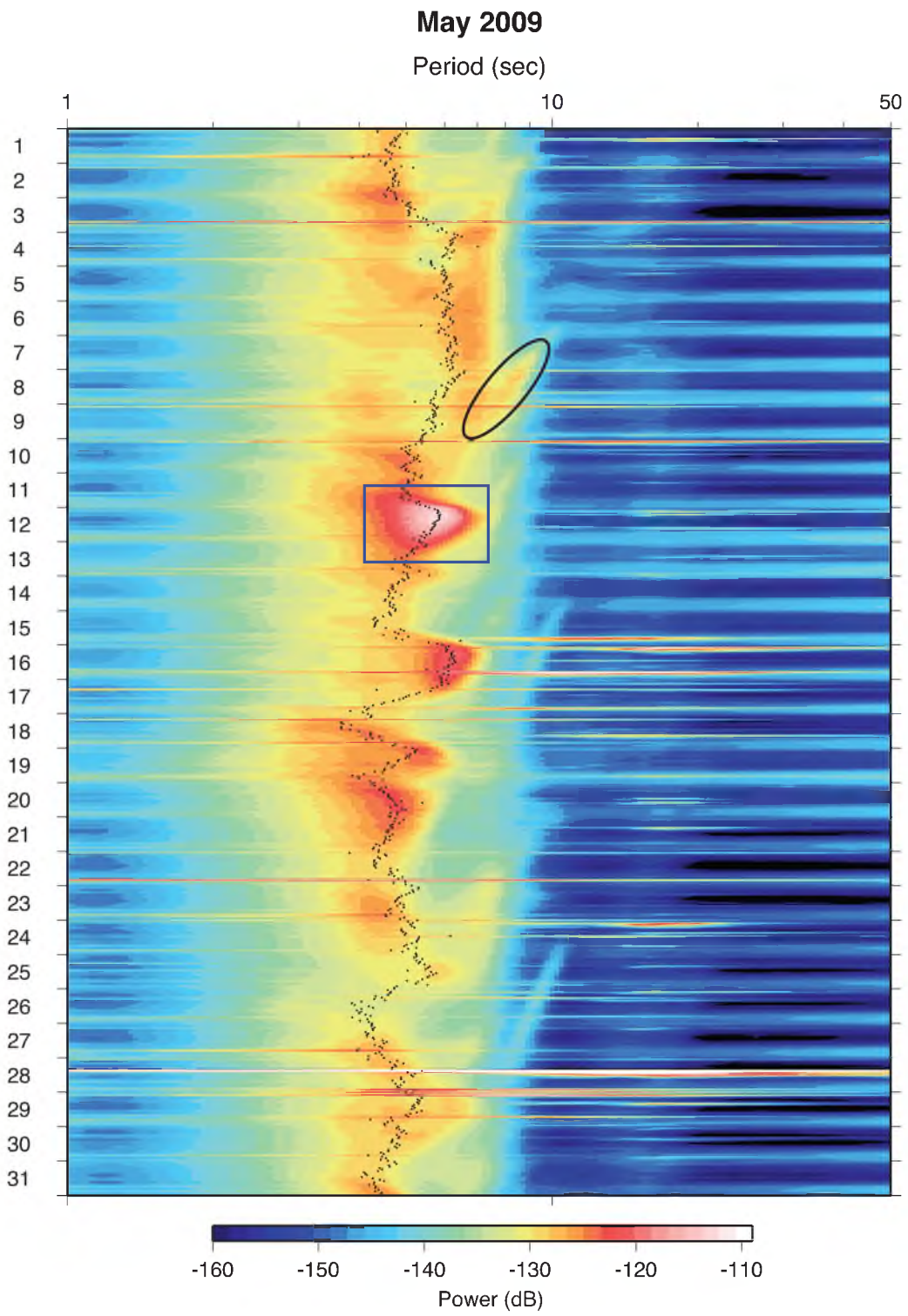

Figure A.5 Array average spectrogram of May 2009. The black ellipses, purple ellipses, blue rectangles, and green rectangles show picked Type I, Type II, Type III, and Type IV microseisms, respectively.

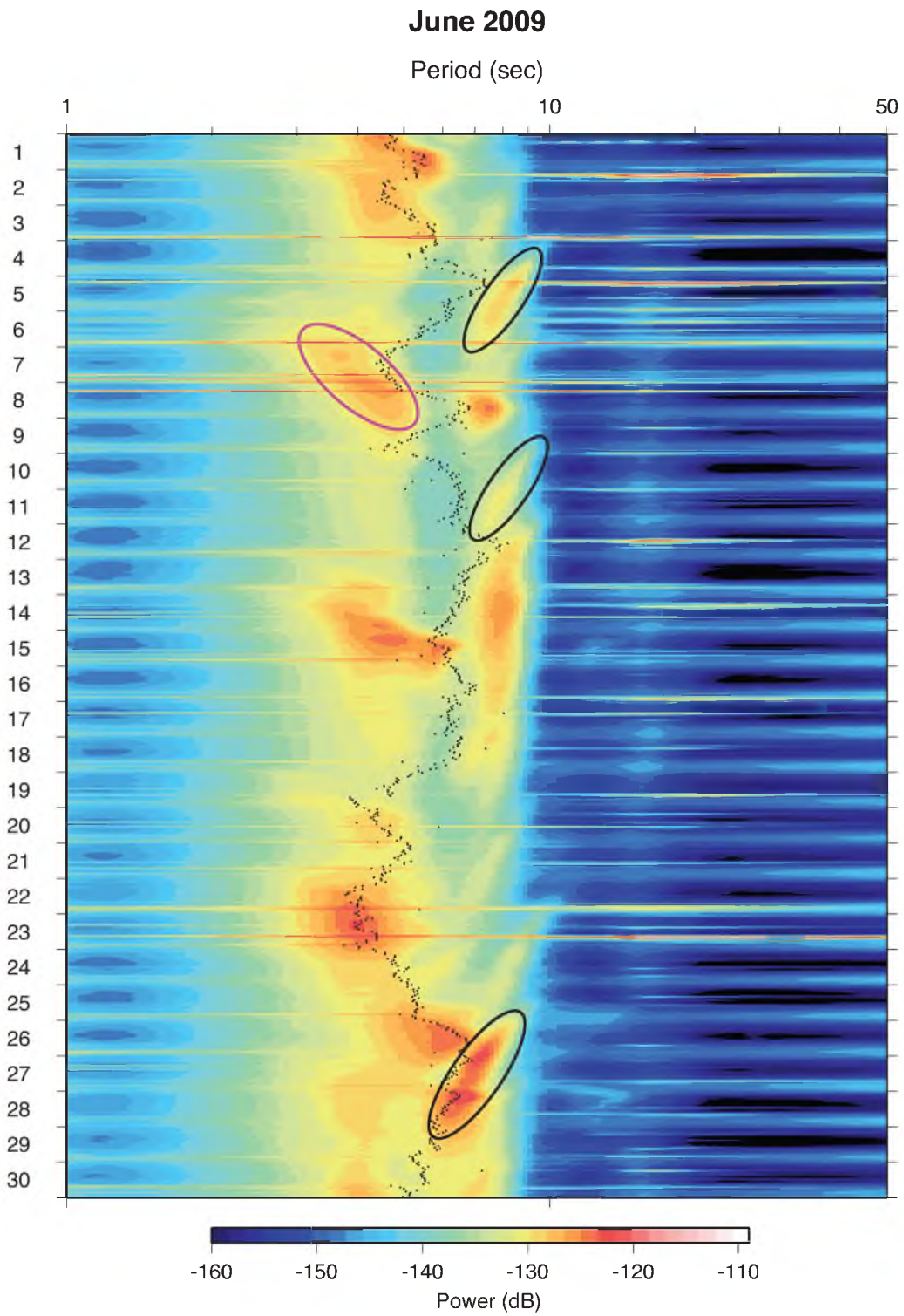

Figure A.6 Array average spectrogram of June 2009. The black ellipses, purple ellipses, blue rectangles, and green rectangles show picked Type I, Type II, Type III, and Type IV microseisms, respectively.

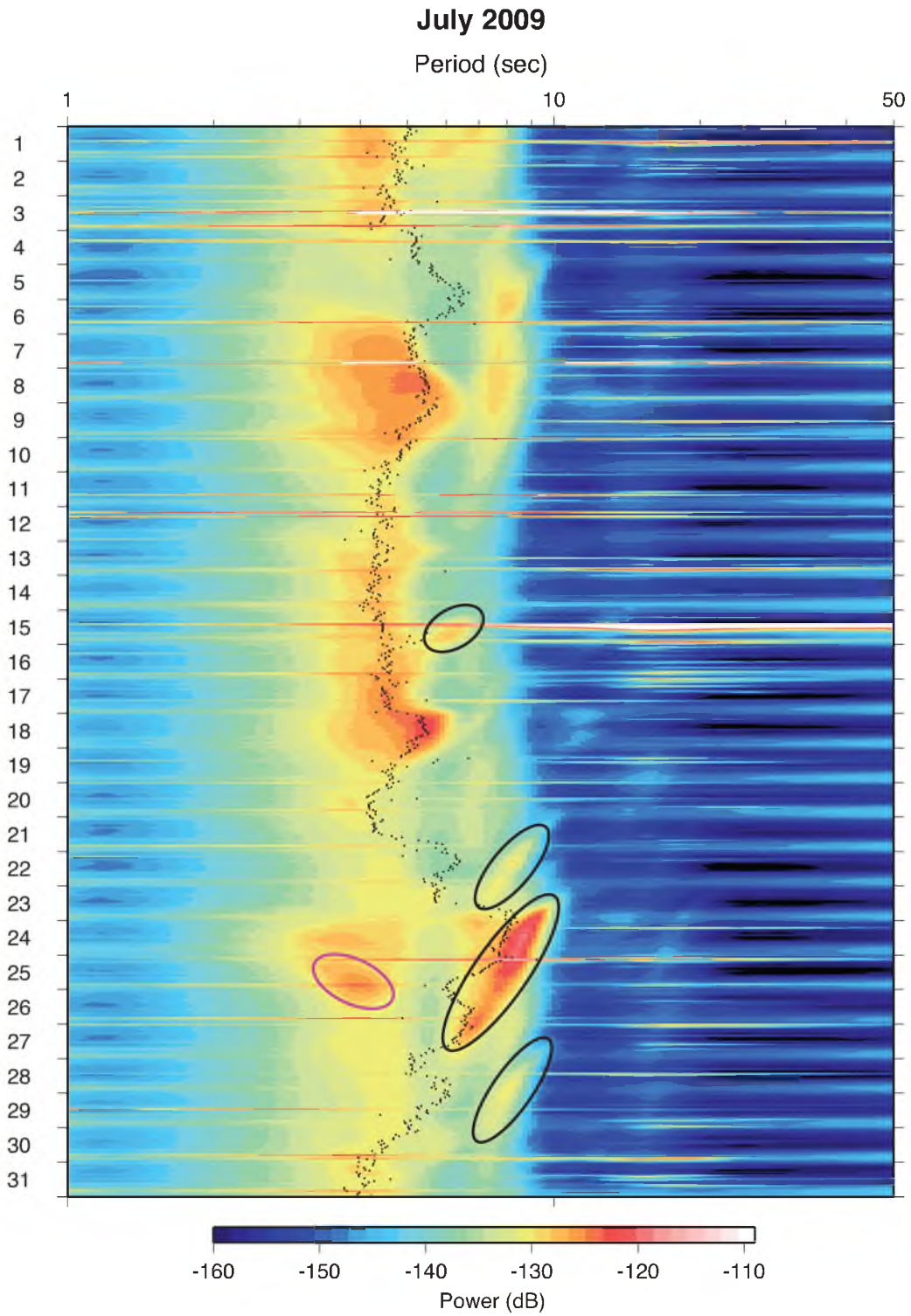

Figure A.7 Array average spectrogram of July 2009. The black ellipses, purple ellipses, blue rectangles, and green rectangles show picked Type I, Type II, Type III, and Type IV microseisms, respectively.

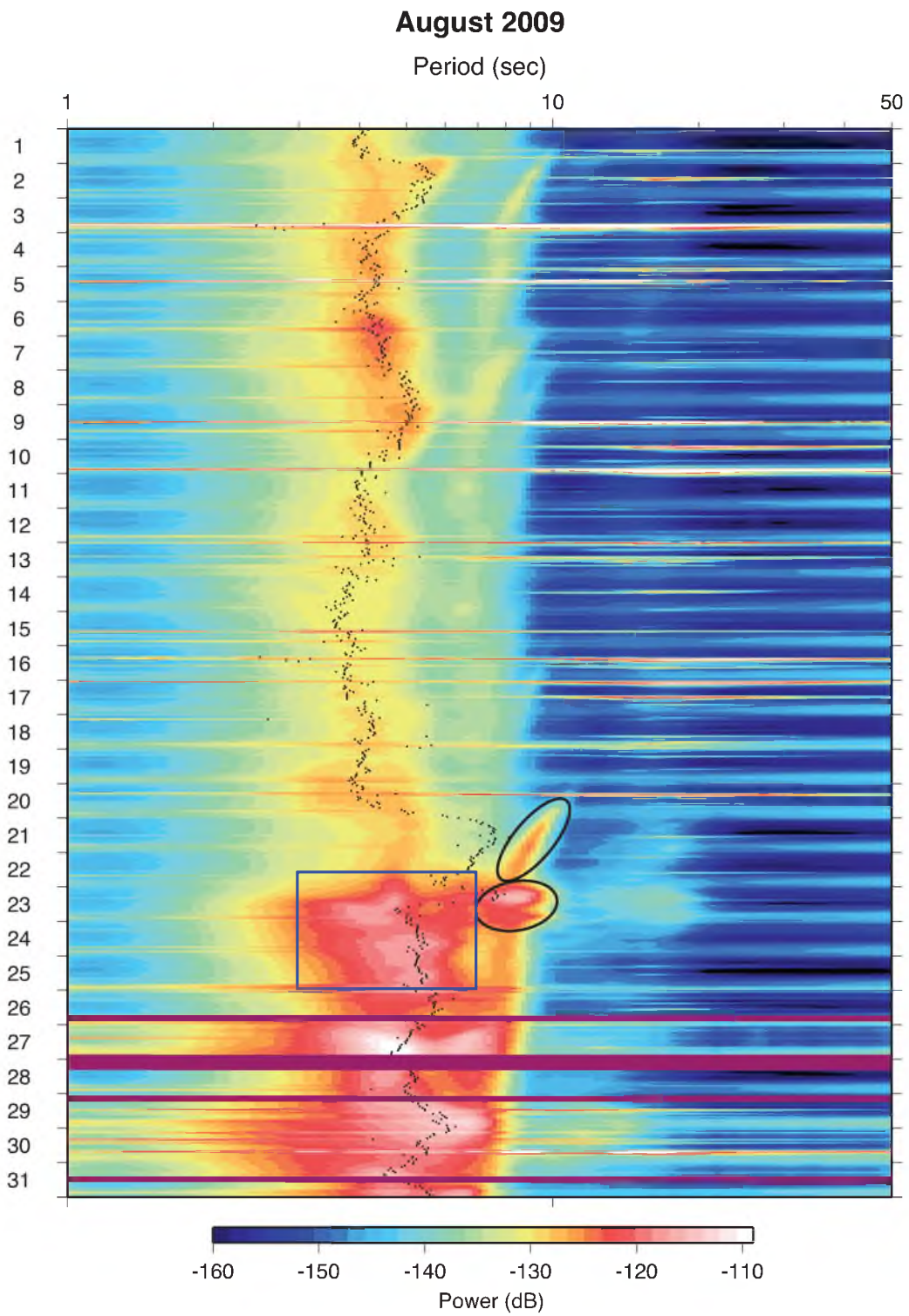

Figure A.8 Array average spectrogram of August 2009. The black ellipses, purple ellipses, blue rectangles, and green rectangles show picked Type I, Type II, Type III, and Type IV microseisms, respectively.

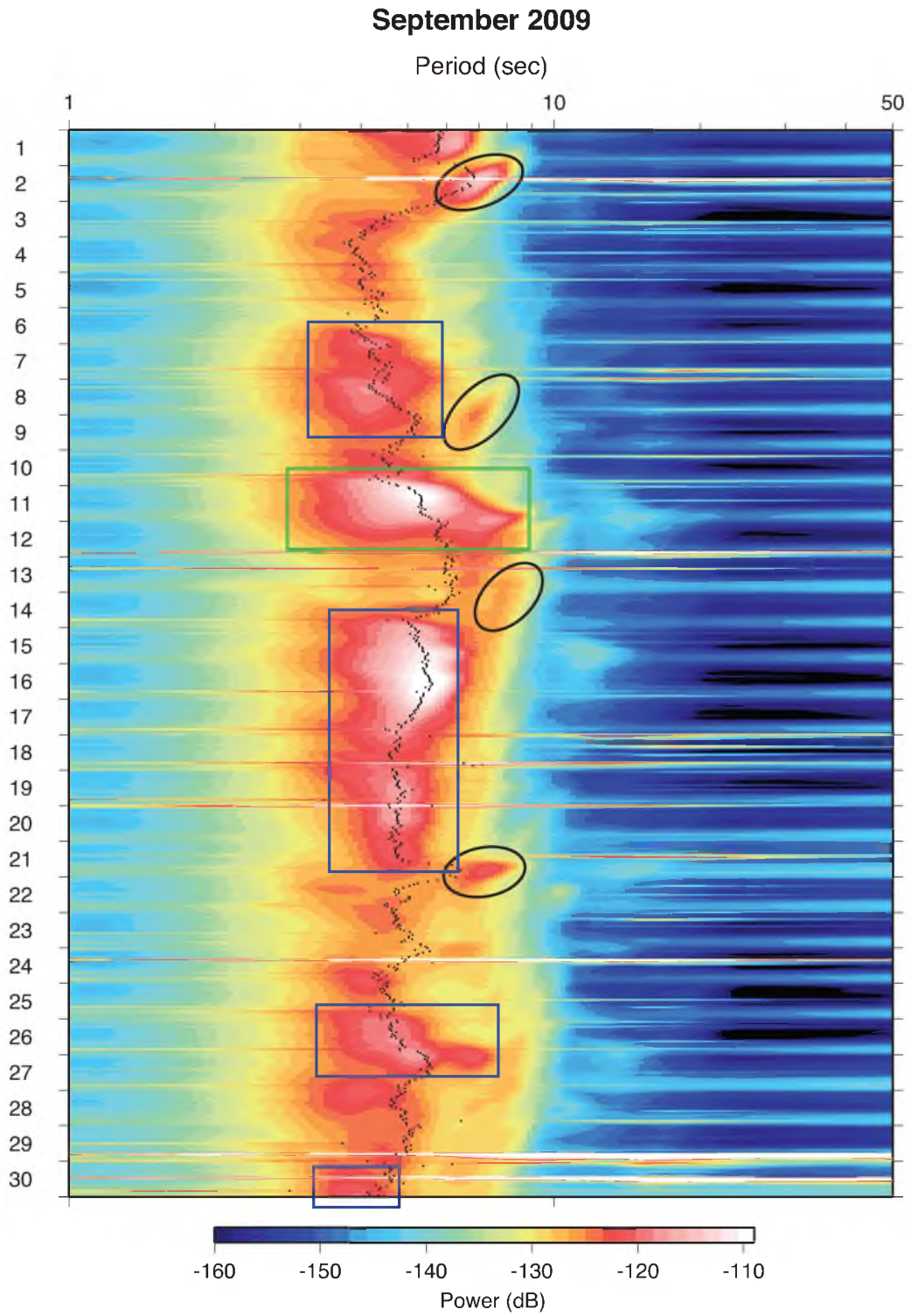

Figure A.9 Array average spectrogram of September 2009. The black ellipses, purple ellipses, blue rectangles, and green rectangles show picked Type I, Type II, Type III, and Type IV microseisms, respectively.

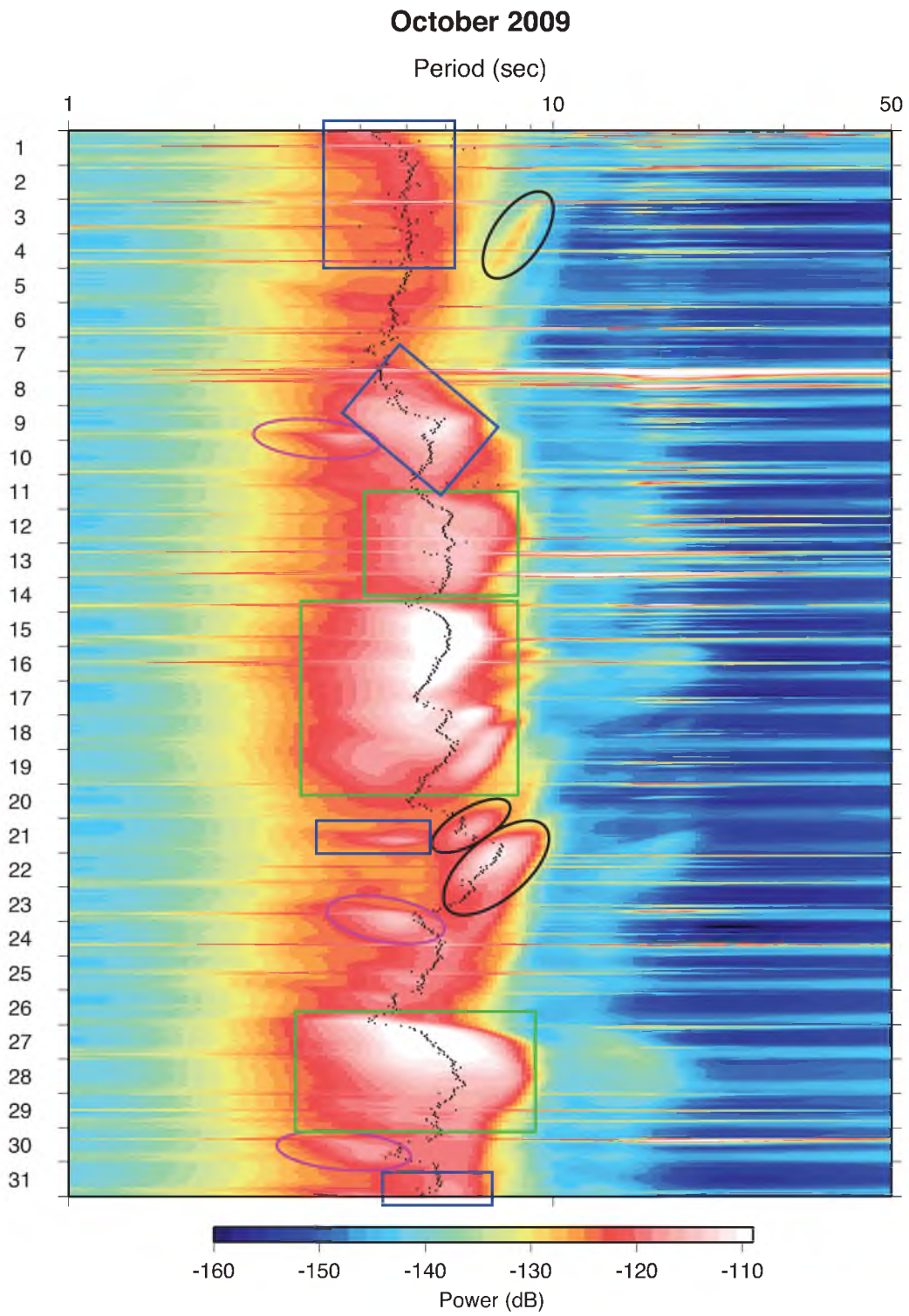

Figure A.10 Array average spectrogram of October 2009. The black ellipses, purple ellipses, blue rectangles, and green rectangles show picked Type I, Type II, Type III, and Type IV microseisms, respectively.

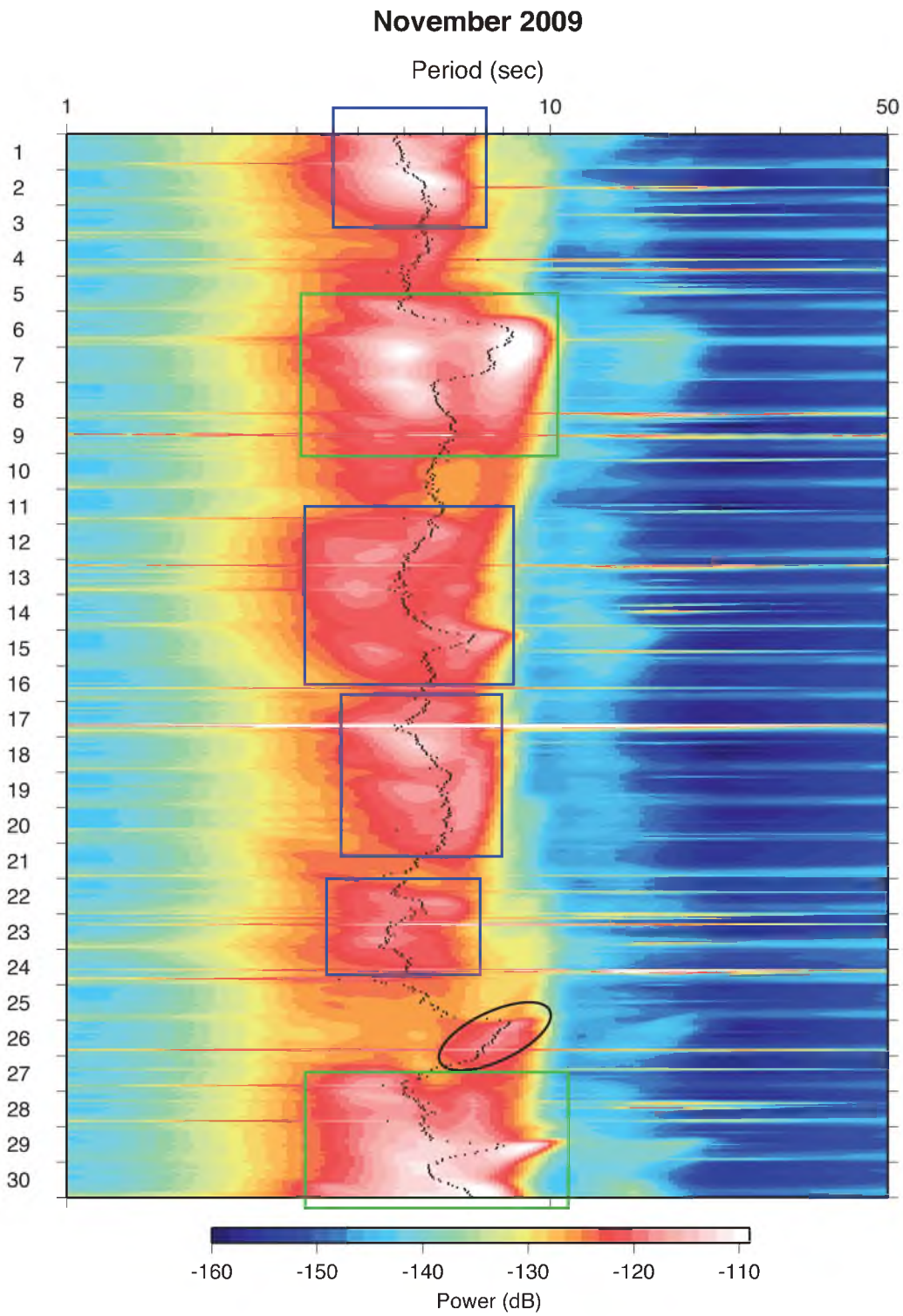

Figure A.11 Array average spectrogram of November 2009. The black ellipses, purple ellipses, blue rectangles, and green rectangles show picked Type I, Type II, Type III, and Type IV microseisms, respectively.

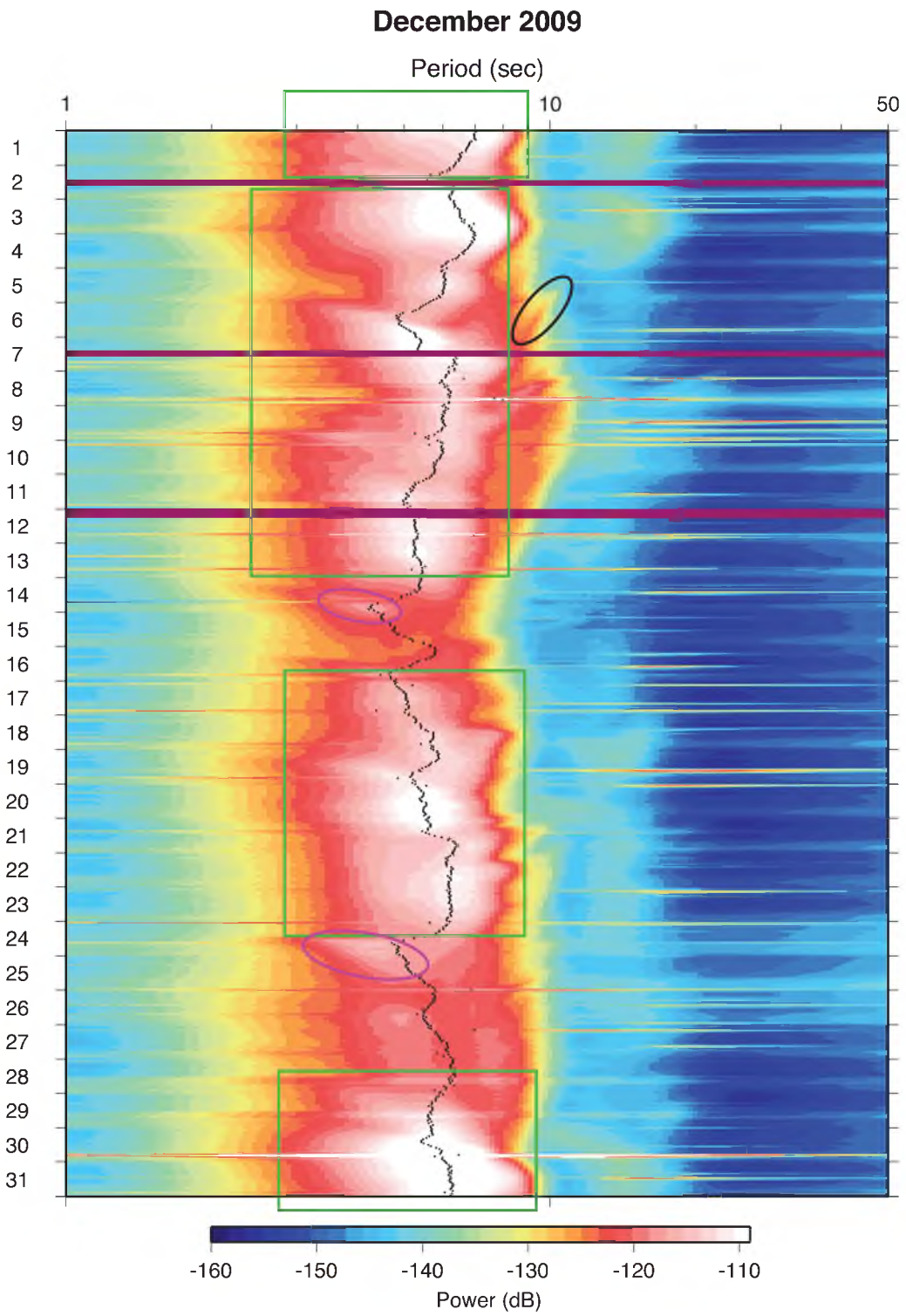

Figure A.12 Array average spectrogram of December 2009. The black ellipses, purple ellipses, blue rectangles, and green rectangles show picked Type I, Type II, Type III, and Type IV microseisms, respectively.

REFERENCES

Arduin, F., and Herbers, T. H. C., 2013. Noise generation in the solid Earth, oceans, and atmosphere, from nonlinear interacting surface gravity waves in finite depth. J. Fluid. Mech. 716, 316–348 , doi:10.1017/jfm.2012-548.

Ardhuin, F., Stutzmann, E., Schimmel, M., and Mangeney, A., 2011. Ocean wave sources of seismic noise. J. Geophys. Res. 116 (C09004). doi:10.1029/2011JC006952.

Aster, R. C., McNamara, D. E., and Bromirski, P. D., 2008. Multidecadal climate-induced variability in microseisms. Seism. Res. Lett. 79 (2), 194–202.

Aster, R. C., McNamara, D. E., and Bromirski, P. D., 2010. Global trends in extremal microseism intensity. Geophys. Res. Lett. 37 (L14303). doi:10.1029/2010GL043472.

Banerji, S. K., 1935. Theory of microseisms. Proc. Indian Acad. Sci. A 1, 727–753.

Behr, Y., Townend, J., Bowen, M., Carter, L., Gorman, R., Brooks, L., and Bannister, S., 2013. Source directionality of ambient seismic noise inferred from three-component beamforming. J. Geophys. Res. 118, 240–248, doi:10.1029/2012JB009382.

Bromirski, P. D., Cayan, D. R., and Flick, R. E., 2005. Wave spectral energy variability in the northeast Pacific. J. Geophys. Res. 110, C03005, doi:10.1029/2004JC002398.

Cessaro, R. K., 1994. Sources of Primary and Secondary Microseisms. Bull. Seismol. Soc. Am. 84 (1), 142–148.

Chevrot, S., Sylvander, M., Benahmed, S., Ponsolles, C., Lefe`vre, J. M., and Paradis, D., 2007. Source locations of secondary microseisms in western Europe: Evidence for both coastal and pelagic sources. J. Geophys. Res. 112 (B11301). doi:10.1029/2007JB005059.

Chi, W.-C., Chen, W.-J., Kuo, B.-Y., and Dolenc, D., 2010. Seismic monitoring of western Pacific typhoons. Mar. Geophys. Res. 31, 239-251. doi:10.1007/s11001-010-9105-x.

Earle, P. S., 1999. Polarization of the Earth's teleseismic wavefield. Geophys. J. Int. 139, 1–8.

Ebeling, C. W., and Stein, S., 2011. Seismological identification and characterization of a large hurricane. Bull. Seismol. Soc. Am. 101 (1), 399403. doi:10.1785/0120100175.

Gerstoft, P., Fehler, M. C., and Sabra, K. G., 2006. When Katrina hit California. Geophys. Res. Lett. 33 (L17308). doi:10.1029/2006GL027270.

Gherzi, E., 1930. Microseisms associated with storms. Gerlands Beitr. Geophysik 25, 145–147.

Grevemeyer, I., Herber, R., and Essen, H.-H., 2000. Microseismological evidence for a changing wave climate in the northeast Atlantic Ocean. Nature 408, 349–352.

Gutenberg, B., 1924. Die seismische Bodenunruhe. Gebrüder Borntraeger, Berlin, 67 pp.

Harris, D., 1990. Comparison of the direction estimation performance of high-frequency seismic arrays and three-component stations. Bull. Seismol. Soc. Am. 80, 1951–1968.

Hasselmann, K., 1963. A statistical analysis of the generation of microseisms. Rev. Geophys. 1, 177–209.

Kedar, S., Longuet-Higgins, M., Graham, F. W. N., Clayton, R., and Jones, C., 2008. The origin of deep ocean microseisms in the North Atlantic Ocean. Proc. R. Soc. London Ser. A 464, 1–35. doi:10.1098/rspa.2007.0277.

Koper, K. D., de Foy, B., and Benz, H., 2009. Composition and variation of noise recorded at the Yellowknife Seismic Array. 1991–2007, J. Geophys. Res. 114 (B10310). doi:10.1029/2009JB006307.

Koper, K. D., and Hawley, V. L., 2010. Frequency dependent polarization analysis of ambient seismic noise recorded at a broadband seismometer in the Central United States. Earthquake Sci. 23, 439–447.

Landès, M., Hubans, F., Shapiro, N. M., Paul, A., and Campillo, M., 2010. Origin of deep ocean microseisms by using teleseismic body waves. J. Geophys. Res. 115 (B05302). doi:10.1029/2009JB006918.

Landsea, C., 2007. Counting Atlantic tropical hurricanes back to 1900. Eos Trans. AGU 88, 197–208.

Laske, G., and Masters, G., 1997. A global digital map of sediment thickness. EOS Trans. AGU 78, F483.

Lay, T., ed., 2009. Seismological Grand Challenges in Understanding Earth's Dynamic Systems. Report to the National Science Foundation, IRIS Consortium, 76 pp.

Longuet-Higgins, M.S., 1950. A theory for the generation of microseisms. Philos. Trans. Roy. Soc. Ser. A. 243, 1–35.

McNamara, D. E., and Buland, R. P., 2004. Ambient noise levels in the continental United States. Bull. Seismol. Soc. Am. 94(4), 1517–1527, doi: 10.1785/012003001.

Miche, M., 1944. Mouvements ondulatoires de lamer en profondeur constante ou decroissante. Ann. Ponts Chaussees 114, 25–78.

Obrebski, M., Ardhuin, F., Stutzmann, E., and Schimmel, M., 2013. Detection of microseismic compressional (P) body waves aided by numerical modeling of oceanic noise sources. J. Geophys. Res. 118, doi:10.1002/jgrb.50233.

Park J, Vernon F. L., and Lindberg, C. R., 1987. Frequency dependent polarization analysis of high-frequency seismograms. J. Geophys. Res. 92, 12,664–12,674.

Peterson, J., 1993. Observations and modeling of seismic background noise. USGS Open File Report 93–322, 94 pp.

Rhie, J., and Romanowicz, B., 2004. Excitation of Earth's continuous oscillations by atmosphere-ocean-seafloor coupling. Nature 431, 552–556.

Samson J. C., 1983. Pure states, polarized waves, and principal components in thespectra of multiple, geophysical time-series. Geophys. J. R. Astr. Soc. 72, 647−664.

Schulte-Pelkum V., Earle P. S., and Vernon, F. L., 2004. Strong directivity of ocean-generated seismic noise. Geochem. Geophys. Geosys. 5 (Q03004). doi:10.1029/2003GC000520.

Sergeant, A., Stutzmann, E., Maggi, A., Schimmel, M., Ardhuin, F., and Obrebski, M., 2013. Frequency-dependent noise sources in the North Atlantic Ocean. Geochem. Geophys. Geosyst. 14. doi:10.1002/2013HGC004905.

Stutzmann, E., Schimmel, M., Patau, G., and Maggi, A., 2009. Global climate imprint on seismic noise. Geochem. Geophys. Geosyst. 10 (Q11004). doi:10.1029/2009GC002619.

Traer, J., Gerstoft, P., Bromirski, P. D., and Shearer, P. M., 2012. Microseisms and hum from ocean surface gravity waves. J. Geophys. Res. 117, B11307, doi: 10.1029/2012JB009550.

Zhang, J., Gerstoft, P., and Shearer, P. M., 2009. High-frequency P-wave seismic noise driven by ocean winds. Geophys. Res. Lett. 36, L09302, doi: 10.1029/2009GL037761.